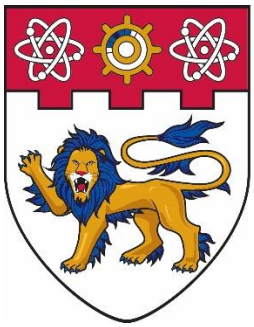

NANYANG TECHNOLOGICAL UNIVERSITY
SINGAPORE

INDUCING HYBRID PEROVSKITE CRYSTAL GROWTH ON SUBSTRATES FOR EFFICIENT, AMBIENT STABLE OPTOELECTRONIC DEVICES

RIYAS AHMAD

Interdisciplinary Graduate School

Energy Research Institute @ NTU (ERI@N)

2021

INDUCING HYBRID PEROVSKITE CRYSTAL GROWTH ON SUBSTRATES FOR EFFICIENT, AMBIENT STABLE OPTOELECTRONIC DEVICES

RIYAS AHMAD

Interdisciplinary Graduate School

Energy Research Institute @ NTU (ERI@N)

A thesis submitted to the Nanyang Technological University in partial fulfillment of the requirement for the degree of

Doctor of Philosophy

2021

Statement of Originality

I hereby certify that the work embodied in this thesis is the result of original research, is free of plagiarised materials, and has not been submitted for a higher degree to any other University or Institution.

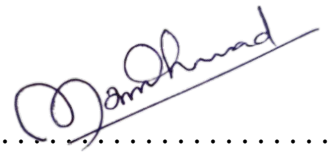

5th April 2021 . . . . . .

Date Riyas Ahmad

Supervisor Declaration Statement

I have reviewed the content and presentation style of this thesis and declare it is free of plagiarism and of sufficient grammatical clarity to be examined. To the best of my knowledge, the research and writing are those of the candidate except as acknowledged in the Author Attribution Statement. I confirm that the investigations were conducted in accord with the ethics policies and integrity standards of Nanyang Technological University and that the research data are presented honestly and without prejudice.

16th April 2021 . . . . . .

Date Prof. Subodh Gautam Mhaisalkar

Authorship Attribution Statement

This thesis contains material from two papers published in the following peer-reviewed journals where I was the first author.

Chapter 4 and 6 are published as Riyas Ahmad, Abhijith Surendran, P. C. Harikesh, Reinhard Haselsberger, Nur Fadilah Jamaludin, Rohit Abraham John, Teck Ming Koh, Annalisa Bruno, Wei Lin Leong, Nripan Mathews, Maria-Elisabeth Michel-Beyerle, Subodh G. Mhaisalkar, Perturbation-Induced Seeding and Crystallization of Hybrid Perovskites over Surface-Modified Substrates for Optoelectronic Devices. *ACS Applied Materials and Interfaces*, 31, 27727–27734 (2019). DOI: 10.1021/acsami.9b05965.

The contributions of the co-authors are as follows:

- Prof. Subodh GM, Prof. ME Michel-Beyerle and Assoc. Prof. Nripan M provided the initial project direction and edited the manuscript drafts.
- I prepared the manuscript drafts. The manuscript was revised by Dr. Rohit AJ and Dr. TM Koh.
- I co-designed the study with Dr. TM Koh and A. Prof. WL Leong.
- All material synthesis, device fabrication and characterization were conducted by me in the Energy Research Institute @ NTU (ERI@N). The intensity-dependent time-correlated single photon counting of the fluorescence emission was performed by Dr. Reinhard H at the center of biophysics at SPMS, supported by NTU Singapore.
- Abhijith S assisted in the collection and analysis of photodetector characteristics and measured the DLS data.
- Dr. PC Harikesh assisted with the SEM and cross-sectional imaging.
- Dr. N Fadilah and Dr. Annalisa B performed the photoluminescence characterizations.
- Dr. Rohit AJ assisted in the collection of I-V data and SCLC measurements.

Chapter 5 and 6 are submitted as Riyas Ahmad, Pio John S. Buenconsejo, Ming Pin Alan Lim, P.C. Harikesh, Vipinraj Sugathan, Reinhard Haselsberger, Bening Titra Muhammad, Teck Ming Koh, Annalisa Bruno, Wei Lin Leong, Nripan Mathews, Maria-Elisabeth Michel-Beyerle, Subodh G. Mhaisalkar, Highly Crystalline and Oriented $MAPbI_3$ Spherulitic Films by Tailoring Crystal Growth Kinetics.

The contributions of the co-authors are as follows:

- Assoc. Prof. Nripan M, Prof. Subodh GM and Prof. ME Michel-Beyerle provided the initial project direction and edited the manuscript drafts.
- I prepared the drafts of the manuscript. The manuscript was revised together by Dr. TM Koh and Dr. Reinhard H.
- I co-designed the study with Assoc. Prof. Nripan M and Dr. Annalisa B.
- I performed all the material deposition processes, device fabrication. collected and analyzed the measured data at Energy Research Institute @ NTU (ERI@N) and Facility for Analysis Characterisation Testing & Simulation (FACTS).
- I performed the *X*-ray pole figure analysis with the assistance of Dr. Pio John SB at FACTS.
- MP Alan Lim performed EBSD measurements and carried out the analysis with me and Dr. Pio John SB at FACTS.
- Dr. PC Harikesh and Vipinraj S assisted with SCLC measurements.
- Bening TM and A. Prof. WL Leong assisted with photovoltaic cell measurements.

5th April 2021 . . . . . .

Date Riyas Ahmad

Abstract

Hybrid lead perovskites are at the forefront of emerging class of optoelectronic materials. With a certified photovoltaic efficiency of 25.2 % for 9 mm^2 area devices, it is currently the most efficient emerging photovoltaic technology. The lion's share of perovskite photovoltaic devices employs polycrystalline thin films of this material, with typical grain sizes around 300 nm. The optoelectronic characteristics like trap density and carrier lifetimes are several orders of magnitude better in perovskite single crystals, suggesting that these materials have the potential to deliver higher power conversion efficiencies than their polycrystalline film counterparts. Even though there are a plethora of reports on polycrystalline devices, works on monocrystalline perovskite photovoltaic cells are scanty, owing to their difficulties in device fabrication procedures. For the fabrication of efficient single crystal-based devices, the crystals need to be sliced into wafers of thickness typically lesser than the diffusion length of charge carriers (of the order of 100 μm). As this material is brittle and has a low shear modulus (of the order 10 GPa), it cannot be sliced down to these thickness regimes. Therefore, the only viable option to fabricate a single crystal/highly-crystalline hybrid perovskite device, is to grow the crystals of these materials directly on the device substrates. Photovoltaic devices fabricated using methylammonium lead iodide ($MAPbI_3$) monocrystalline films have yielded efficiencies of 21 % for a device area of 2 mm^2; however, scaling beyond a few millimeters in lateral dimensions is yet to be achieved. In this work, two techniques were developed to grow highly crystalline layers of $MAPbI_3$ films over substrates, without any constraint over their lateral dimensions. The mechanism of anti-solvent vapor crystallization (AVC) of lead halide perovskites was meticulously investigated, and sonication modified AVC (S-AVC) was developed. As the nucleation and initial crystal growth was initiated by sonication, this crystal growth technique was independent of the nature of substrates and their surfaces. The grain sizes of these films were around 100 micrometers, three orders of magnitude higher than standard polycrystalline thin films. These highly crystalline films were utilized to fabricate planar photodetectors with a responsivity of 20 AW^{-1}, a 1000 times higher than that of polycrystalline thin film based devices. The thicknesses of S-AVC

based films were of the order of hundred micrometers and were crystallographically random-oriented, making it inappropriate to fabricate vertical optoelectronic devices. In order to overcome these shortcomings of the technique, a second method was developed by modifying the standard spin coating procedure used to deposit perovskite thin films. The perovskite precursor chemistry was tuned, and crystallization kinetics were optimized for inducing heterogeneous nucleation and growth of spherulitic perovskite crystals on substrate surfaces. These films were compact and pinhole free with grain sizes above 100 micrometers. The film thicknesses were easily controllable to a few hundred nanometers by varying the spin coating parameters and the films were highly oriented along [200], [224] crystallographic planes, thus befitting it for vertical photovoltaic device fabrication. The fabricated photovoltaic cells exhibited superior room ambient stability along with good photoconversion efficiencies above 15 %, owing to the enhanced crystallinity of the perovskite layer. The films of various levels of crystallinity were used to unveil the role of grain boundaries on ambient stability of the material. It was proved that a reduction in the number of grain boundaries hampers the moisture induced degradation, thus can be used as an alternative strategy to enhance the ambient stability of perovskite based optoelectronic devices. Lead halide perovskites are known mixed ionic-electronic conductors and the films of various levels of crystallinity were used to study the effect of grain boundaries on ionic motion through the material. In comparison to standard thin films, the ionic conductance was 100 times higher in S-AVC based films which demonstrated that grain boundaries can reduce ionic and electronic conductance by blocking the charge transport through the material. In a nutshell, two techniques were developed in this thesis to grow highly crystalline layers of hybrid lead halide perovskites over substrates. The grown films were utilized to study the effect of crystallinity on optoelectronic device characteristics, ionic conductance and moisture stability of the material.

Lay Summary

Gustav Rose, a German mineralogist discovered the mineral $CaTiO_3$ in the Ural Mountains of Russia in 1839 and was named as perovskite, in honour of Russian mineralogist L. A. Perovski (1792 - 1856). Later, numerous materials with a similar ABX_3 structure were discovered and were named as perovskites, one of the highly investigated material systems with numerous possible electronic applications. In 2009, T. Miyasaka and co-workers from Japan employed hybrid organic-inorganic lead halide perovskites like methylammonium lead iodide ($MAPbI_3$) to replace the light absorbing dye of a dye sensitized solar cell and demonstrated its possible photovoltaic application. Ten years later, as of 2020 lead halide perovskite based solar cells have achieved a photoconversion efficiency of 25.2 %, a feat achieved by the conventional silicon-based cells in 60 years. As a result of an intensive research on the material system, lead halide perovskites have also found their application in light emitting diodes, lasers, *X*-ray detectors, photodetectors and so on. Majority of electronic or optoelectronic devices use a polycrystalline thin film of lead halide perovskites as the semiconductor layer. Employing a monocrystalline or highly crystalline film of the material is expected to enhance the electronic characteristics of the devices, owing to their improved charge carrier generation and conduction. However, monocrystalline devices are difficult to realize, because of the brittleness of the material as well as the intricate fabrication and crystal growth procedures involved. A crystalline perovskite optoelectronic device requisite the growth of the thin semiconductor layer directly over device substrates, thus providing the mechanical robustness for subsequent fabrication processes. This thesis develops strategies to grow highly crystalline layers of lead halide perovskites over the device substrates. Devices like photodetectors and photovoltaic cells are fabricated to study the effect of crystallinity on optoelectronic device characteristics, their ambient stability and ionic conductivity.

Acknowledgements

PhD journey is a roller coaster ride with victories and defeats. At the very moment of conclusion of this journey, I would like to express my profound appreciation to some individuals who shaped my graduate student and personal lives. Above all, I would like to express my sincere gratitude to my supervisors, Prof. Maria-Elisabeth Michel-Beyerle and Prof. Subodh G. Mhaisalkar for their continuous guidance and encouragement throughout the work, which in turn chiseled the scope of this thesis. I am honored and humbled to work with these eminent researchers in the field of photo-physics and optoelectronic materials, which I strongly believe to have created an enormous impact on my scientific career. I would also like to thank my mentor, Prof. Cesare Soci, whose constructive feedbacks have helped in compiling this thesis in this current form. I am extremely grateful for the coursework he taught (Optical Spectroscopic Techniques) in my initial year of graduate studies, which tremendously helped me during my research.

I would like to express my deepest gratitude to Prof. Nripan Mathews for his invaluable guidance during the difficult times of this work. I would like to thank him for his efforts and ideas which helped to keep me focused whenever I deviated from my thesis objectives. I am greatly indebted to research scientists at ERI@N, Dr. D. Bahulayan and Dr. Teck Ming Koh for their suggestions and feedbacks, which helped me in channeling this work. I would also like to express my sincere appreciation to Dr. Reinhard H. for helping me to edit the thesis manuscript.

I also wish to thank my colleagues at ERI@N for their moral support and help, which enabled me to wade forward during my tough times. I would like to express my deepest sense of gratitude to my friends in the laboratory – Abhijith, Fadilah, Yan Fong, Harikesh, Rohit, Bevita, Biplab, Annalisa, Bhumika, Bening, Benny, Wang Hao, Herlina, Mohit, Naveen, Xiaoting, Vipinraj, Xintong, Sujay, Sneha, Guifang, Salim, Alasdair, Anil, Jagadeesh, Enke, Sjoerd, Li Jia and Prem. I would also like to thank some of my friends – Sujith, Govind, Vishal and Ojus whom I met during the 4 years

of my graduate student life. I would also wish to express my gratitude to ERI@N, its administrative as well as supporting staff for providing a wonderful research facility.

As Sir Isaac Newton said, *If I have seen further than others, it is by standing upon the shoulders of giants.* I am profoundly indebted to those who 'walked' before me and laid the foundations for this work, from numerous scientists and researchers known to humanity to my pals in the laboratory.

Last but foremost, I would like to thank my parents and sister for upbringing me and supporting me to pursue my passion and making me the man I am today. I also wish to express my deepest gratitude to my wife Ameena for being a good friend, for her love and constant forbearance during the difficult times of our lives.

Better Than a Thousand Days of Diligent Study is One Day with a Great Teacher

- *Japanese proverb*

To the teachers who taught me, from my kindergarten to my doctoral studies

Table of Contents

Table Captions

Figure Captions

Abbreviations

0D	Zero Dimensional
1D	1 Dimensional
2D	2 Dimensional
3D	3 Dimensional
AFM	Atomic Force Microscopy
AVC	Anti-solvent Vapor Crystallization
CBM	Conduction Band Maximum
CCD	Charge Coupled Device
CMOS	Complementary Metal Oxide Semiconductor
DI	De-ionized
DJ	Dion-Jacobson
DLS	Dynamic Light Scattering
EBSD	Electron Backscatter Diffraction
ETL	Electron Transporting Layer
FM	Frank van der Merwe
FWHM	Full Width Half Maximum
HTM	Hole Transporting Material
IPCE	Internal Power Conversion Efficiency
ITC	Inverse Temperature Crystallization
LASER	Light Amplification by Stimulated Emission of Radiation
LED	Light Emitting Diode
MIEC	Mixed Ionic Electronic Conductor
OWRK	Owens, Wendt, Rabel and Kaeble

PL	Photoluminescence
PV	Photovoltaic
RP	Ruddlesden-Popper
S-AVC	Sonication modified Antisolvent Vapor Crystallization
SCLC	Space Charge Limited Current
SEM	Scanning Electron Microscopy
SK	Stanski-Krastanov
TFL	Trap Filling
UV	Ultra-violet
VW	Volmer-Weber
WTMetaD	Well-tempered Metadynamics
XRD	*X*-ray Diffraction

Chemical Names

ACN	Acetonitrile
APTMS	Aminopropyltrimethoxysilane
DCM	Dichloromethane
DMF	N,N-dimethylformamide
DMSO	Dimethylsulfoxide
FTO	Fluorine-doped Tin Oxide
GBL	γ-Butyrolactone
ITO	Indium-doped Tin Oxide
MABr	Methylammonium bromide
MAI	Methylammonium iodide
$MAPbBr_3$	Methylammonium lead bromide

$MAPbI_3$	Methylammonium lead iodide
OTS	Octadecyltrichlorosilane

Physical Quantities

Abbreviation	**Quantity**	**Unit**
D*	Detectivity	Jones
EQE	External Quantum Efficiency	%
J_{sc}	Short Circuit Current Density	$mAcm^{-2}$
PCE	Power Conversion Efficiency	%
R	Responsivity	AW^{-1}
RH	Relative Humidity	%
T_{rise}, T_{fall}	Rise-time, Fall-time	ms
V_{oc}	Open Circuit Voltage	V

Chapter 1

Introduction

This chapter elucidates the motivation and hypothesis behind this work. The chapter also discusses the research objectives and scope of the work. In the end, the key findings, and outcomes of this work are also provided.

1.1 Motivation and Hypothesis

The sun is the ultimate source of energy on earth. Consequently, the sun was often worshipped as a deity across different civilizations ranging from ancient Egypt to Indo-European and Greco-Roman mythologies. As human civilizations flourished, people found different ways to harness the solar energy. Initially sun's energy stored as biomass was used to meet their energy demands. Later on, the discovery of non-renewable energy resources like coal and 'black gold' fueled abrupt industrialization and scientific breakthroughs. As a result of these scientific and industrial revolutions, human population abruptly surged during the 20th century. Since the 1960's, the world population more than doubled from 3 billion to 7.4 billion, as of 2015[1]. This surge in world population put an imminent demand on energy resources. Reckless exploitation of nonrenewable resources to meet this ever-increasing demand of energy culminated in depletion of these resources. It also resulted in disruption of earth's atmospheric and climatic patterns, which compelled the world to contemplate about green and renewable energy sources.

The solar energy can be harnessed renewably in different forms, of which the direct conversion of sunlight to electric potential is the most viable one. Photovoltaic (PV) devices were developed to convert the light energy to electrical energy which can be stored and used according to the requirements. Different photovoltaic technologies like the ones based on crystalline and amorphous silicon, Cadmium Telluride (CdTe), Gallium Arsenide (GaAs), Copper Indium Gallium diSelenide (CIGS), Copper Zinc Tin Sulfide (CZTS) emerged. All these PV technologies involved cost intensive and intricate fabrication procedures. Hence the initial PV cells were used primarily in artificial satellites and space applications. The cost of materials used in these kind of PV devices reduced considerably but the fabrication procedures remain complicated. This led to the development of totally solution processable technologies. The organic PV cells were cheap and solution processable but produced inferior efficiencies[2]. In 2009 an organic – inorganic hybrid material (hybrid lead halide perovskite) was used as light absorber in PV cell[3]. Within a few years the efficiency of PV devices using this material skyrocketed to 25.2 %[4]. Despite reaching stellar efficiencies, this technology

suffers from several shortcomings which prevent it from commercialization. Apart from being used as a photovoltaic energy harvesting material, lead halide perovskites have recently spurred the research of other optoelectronic devices as well. Crystallization optimization of perovskites have played an important role in improving their device characteristics[5–7]. Its fast and facile single crystal growth enabled the study of its optoelectronic material characteristics[8,9]. The lion's share of perovskite optoelectronic devices employs polycrystalline thin films. The trap density, lifetime and diffusion length of carriers are several orders of magnitude better in single crystals of these materials when compared to their thin film counterparts[9–11]. Hence improving the crystallinity of the material holds the key for improving the device performances. Though there are plethora of works discussing the optoelectronic material and device characteristics of halide perovskites, the investigation of its crystallization and crystal growth requisites intensive research.

Even though large millimeter-sized hybrid perovskite single crystals can be grown easily by fast crystallization techniques, single crystal based devices are very difficult to fabricate. For the fabrication of efficient single crystal based devices, these crystals need to be sliced into wafers of thicknesses typically lesser than the diffusion length of charge carriers (of the order of 100 μm for single crystals). As this material is brittle and has a low shear modulus (of the order 10 GPa), they cannot be sliced down to these thickness regimes[12,13]. Therefore, the only viable option to fabricate a single crystal/highly-crystalline hybrid perovskite device, is to grow the crystals of these materials directly on to the device substrates. Even though thin methylammonium lead bromide ($MAPbBr_3$) crystals were easier to grow over substrates, methylammonium lead iodide ($MAPbI_3$) crystal growth over planar substrates was difficult to achieve due to the intrinsic anisotropic growth of tetragonal crystals[14,15]. Thin $MAPbI_3$ crystals were later grown in between two parallel substrates and solar cells were fabricated employing them. However, their lateral dimensions were of the order of a few millimeters thus impeding it from scaling up to large device areas[16]. Increasing the lateral dimensions of these thin monocrystals or improving the crystallinity of the perovskite polycrystalline films deposited over substrates is the realistic solution to completely harness their stellar optoelectronic material properties. The precursors play

an important role in the crystallization and crystal growth of lead halide perovskites. It was found that solvents form coordination complexes with the perovskite precursors, and the precursor-solvent complexes form a colloidal dispersion[17]. Thus, a systematic optimization of the crystallization process should accompany a rigorous investigation of the nature of solvents used.

The work presented here are based on the following hypothesis:

1. Reduced material crystallinity in thin film devices leads to underutilization of its excellent optoelectronic properties which are inherent to hybrid lead perovskite material system.
2. Precursors play a crucial role in the crystallization of lead halide perovskites and a meticulous study of precursors can help to induce the growth of perovskite crystals on device substrates.
3. Initiation of nucleation sites away from the substrate surface during crystallization prevents the growth of highly crystalline perovskite films as well as perovskite single crystals over substrates. Confining the nucleation centers on the substrates results in highly oriented, thin and crystalline films suitable for perovskite photovoltaics.
4. Usage of highly crystalline and thin perovskite film in photovoltaic devices and photodetectors improves their device performances and efficiencies. Grain boundaries of perovskite materials in devices not only result in inferior optoelectronic device performances, but also adversely affect the device stability.

1.2 Research Objectives and Scope

Based on the discussed hypothesis, the objectives of our research are:

1. To investigate and develop new strategies for growing highly crystalline and oriented perovskite films on device substrates.

   (a) Modulating the crystallinity and orientation of perovskite film growth by investigating the precursor chemistry and optimizing the crystallization processes.

(b) Modifying the crystallization techniques by confining the nucleation sites and restricting the crystal growth to achieve a uniform two-dimensional growth over the substrates.

2. To study the fundamental material properties of the highly crystalline perovskite film.

   (a) Investigating and comparing the material properties of the highly crystalline perovskite film with that of a normal polycrystalline thin film.

   (b) The effects of grain boundaries on the ambient stability of the film have to be studied.

3. To fabricate optoelectronic devices and to investigate the optoelectronic device properties of high crystallinity perovskites.
   (a) Fabricating model photodetectors/photovoltaic cells and characterizing them to study the fundamental device and material characteristics.
   (b) The effect of crystallinity on the electronic and device properties has to be investigated.

1.3 Dissertation Overview

Chapter 1 states the background and need for inducing the growth of lead halide perovskite crystals on device substrates outlining the motivations and hypothesis leading to it.

Chapter 2 presents a detailed literature review on lead halide perovskites and their exemplary optoelectronic properties. The chapter also compares the characteristics of perovskite crystal based photodetectors and photovoltaic cells with their thin film counterparts. The classical theory of nucleation and crystal growth are also discussed.

Chapter 3 outlines the normal thin film deposition and device fabrication procedures used in this thesis. In addition, it explains the various experimental techniques used to evaluate the crystallinity, orientation, optical and electronic properties of the materials.

Chapter 4 discusses the colloidal chemistry of lead halide precursors in different solvents. The chapter also explains the mechanism of anti-solvent vapor crystallization (AVC) for lead halide perovskites. The standard AVC technique is modified to grow $MAPbBr_3$ and $MAPbI_3$ crystals on substrates. The crystallinity, orientation and ambient stability of the grown crystal films are investigated.

Chapter 5 utilizes the findings on perovskite precursors from Chapter 4 and modifies the spin coating process to induce heterogeneous nucleation on substrates. By confining the nucleation and growth to the substrate surface, close packed crystals of high aspect ratio are grown, and their material properties are investigated.

Chapter 6 harnesses the crystallization techniques discussed in Chapter 4 and Chapter 5 to fabricate photodetectors and photovoltaic cells. The characteristics and performances are compared to normal thin film based devices. The effect of grain boundaries on device performances are explained.

Chapter 7 discusses the scientific insights from the works explained in the above chapters and the possible future work in this field.

1.4 Findings and Outcomes

The thesis presents the following outcomes:

1. The investigations on the mechanism of crystal growth of lead halide perovskites by anti-solvent vapor crystallization (AVC) revealed the critical role of crystallization dish surfaces on nucleation and growth. This thesis elucidates the mechanism of AVC of perovskites and develops a new crystallization technique for the first time.
2. The studies on the nature of lead halide perovskite precursors were applied to optimize the normal spin coating process to grow highly crystalline films of $MAPbI_3$ spherulitic grains on substrates. *X*-ray diffraction and electron diffraction studies of these films revealed a high level of preferential orientation of these films with respect to the substrate surface.

3. The highly crystalline and oriented films prepared were utilized to fabricate optoelectronic devices like photodetectors and photovoltaic cells to unfold the role of crystallinity on the operational characteristics of these devices. The studies on films of varying levels of crystallinity revealed that a reduction in grain boundaries can enhance the room ambient stability and enhance the ionic conductance of their films.

In short, two methods were developed for growing crystalline, pinhole free layers of lead halide perovskites on device substrates. These films of varying crystallinity were utilized to investigate the effects of grain boundaries on optoelectronic device characteristics, ambient stability and ionic conductance.

1.5 References

1. DADAX. World Population by Year - Worldometers.

2. Scharber, M. C. & Sariciftci, N. S. Efficiency of bulk-heterojunction organic solar cells. *Prog. Polym. Sci.* **38**, 1929–1940 (2013).

3. Kojima, A., Teshima, K., Shirai, Y. & Miyasaka, T. Organometal Halide Perovskites as Visible- Light Sensitizers for Photovoltaic Cells. *J Am Chem Soc* **131**, 6050–6051 (2009).

4. *Best Research-Cell Efficiency Chart* Available at: https://www.nrel.gov/pv/cell-efficiency.html.

5. Tidhar, Y. *et al.* Crystallization of methyl ammonium lead halide perovskites: Implications for photovoltaic applications. *J. Am. Chem. Soc.* **136**, 13249–13256 (2014).

6. Jeon, N. J. *et al.* Solvent engineering for high-performance inorganic-organic hybrid perovskite solar cells. *Nat. Mater.* **13**, 897–903 (2014).

7. Yang, W. S. *et al.* High-performance photovoltaic perovskite layers fabricated through intramolecular exchange. *Science.* **348**, 1234–1237 (2015).

8. Saidaminov, M. I., Abdelhady, A. L., Maculan, G. & Bakr, O. M. Retrograde solubility of formamidinium and methylammonium lead halide perovskites enabling rapid single crystal growth. *Chem. Commun.* **51**, 17658–17661 (2015).

9. Shi, D. *et al.* Low trap-state density and long carrier diffusion in organolead trihalide perovskite single crystals. *Science.* **347**, 519–522 (2015).

10. Dong, Q. *et al.* Electron-hole diffusion lengths > 175 μm in solution-grown $CH_3NH_3PbI_3$ single crystals. *Science.* **347**, 967–970 (2015).

11. Saidaminov, M. I. *et al.* High-quality bulk hybrid perovskite single crystals within minutes by inverse temperature crystallization. *Nat. Commun.* **6**, 1–6 (2015).

12. Rolston, N. *et al.* Mechanical integrity of solution-processed perovskite solar cells. *Extrem. Mech. Lett.* **9**, 353–358 (2016).

13. Feng, J. Mechanical properties of hybrid organic-inorganic $CH_3NH_3BX_3$ (B = Sn, Pb; X = Br, I) perovskites for solar cell absorbers. *APL Mater.* **2**, 081801 (2014).

14. Peng, W. *et al.* Solution-Grown Monocrystalline Hybrid Perovskite Films for Hole-Transporter-Free Solar Cells. *Adv. Mater.* **28**, 3383–3390 (2016).

15. Saidaminov, M. I. *et al.* Planar-integrated single-crystalline perovskite photodetectors. *Nat Commun* **6**, 8724 (2015).

16. Chen, Z. *et al.* Single-Crystal $MAPbI_3$ Perovskite Solar Cells Exceeding 21 % Power Conversion Efficiency. *ACS Energy Lett.* **4**, 1258–1259 (2019).

17. Yan, K. *et al.* Hybrid Halide Perovskite Solar Cell Precursors: Colloidal Chemistry and Coordination Engineering behind Device Processing for High Efficiency. *J. Am. Chem. Soc.* **137**, 4460–4468 (2015).

Chapter 2

Literature Review

Lead halide perovskites have emanated as an exciting optoelectronic material, finding its application in devices like photovoltaic cells, photodetectors, light emitting diodes, transistors, X-ray detectors and so on. This chapter gives a glimpse on the emergence of lead halide perovskites to the prominence of optoelectronic research, emphasizing its material properties and processing techniques. Photovoltaic cells and photodetector applications are emphasized here, as these devices are the focus of our work. The chapter also compares the characteristics of perovskite crystal based devices with their thin film counterparts. The classical theory of nucleation and crystal growth are also discussed in brief.

2.1 Lead Halide Perovskites and its Material Properties.

Materials with structures similar to that of $CaTiO_3$ (ABX_3 structure in general) are known as perovskites, named after Lev Perovski, a Russian mineralogist. Later on, Victor Goldschmidt, a Norwegian mineralogist did extensive studies on the crystal structure and sizes of constituent ions forming the ABX_3 structure. Lead halide perovskites can be classified as materials having the same ABX_3 structure with A an organic or inorganic cation (like Cs, Rb, methylammonium, formamidinium), B a heavy metal (like Pb or Sn), X a halogen (like Cl, Br, I). The relative radii and oxidation states of A, B and X ions determine whether a structure is thermodynamically stable or not. An index called tolerance factor (t) was developed empirically to predict the stability of perovskite crystal structures. Tolerance factor can be defined as:

$$t = \frac{r_A + r_B}{\sqrt{2}(r_A + r_B)}$$

Where, r_A and r_B are the relative radii of the ions. The perovskite structure is stable if $0.8 < t < 1$.

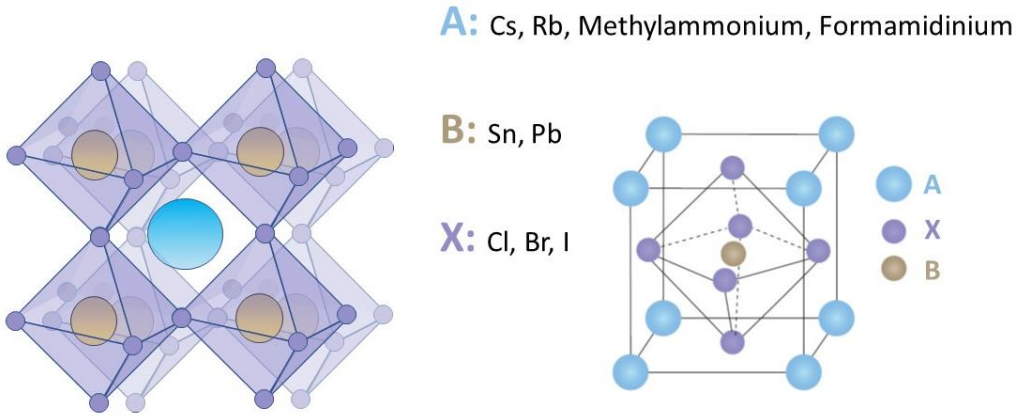

Figure 2.1: The general ABX_3 structure of lead halide perovskites[6].

Almost all the intriguing properties of this class of materials can be attributed to its interesting electronic band structure and its unusual defect physics. In methylammonium lead iodide ($CH_3NH_3PbI_3$), CH_3NH_3 donates one electron, Pb donates two electrons to three I ions. The material has a band gap of 1.5 eV. The

CH_3NH_3 molecule and its orientation do not directly contribute to the band gap, as the band gap is decided by the Pb-I framework and its orientation[1]. The valence and conduction band are formed by hybridization of 5p orbital of iodine and 6s, 6p orbitals of lead. The valence band maxima have bonding orbitals formed by Pb(6p) and I(5p) σ antibonding. The conduction band minima comprise of Pb(6p) and I(5s) σ antibonding as well as Pb(6p) and I(5s) π antibonding orbitals. This is said to be the reason for the material's defect tolerance. For a material with such a band structure, the defects formed as a result of dangling bonds do not create any energy level in the band gap of the material[2].

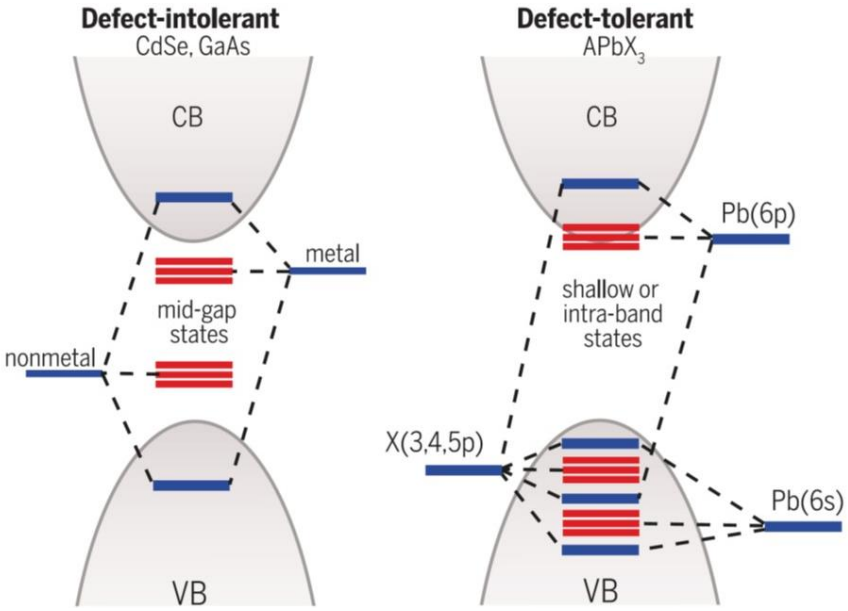

Figure 2.2: The formation of electronic band structure in $MAPbI_3$ and the origin of its defect tolerance[3].

It has also been found that the defects caused by I vacancy create a shallow energy level near the conduction band, resulting in n-type doping. p-type self-doping is formed by Pb and MA vacancies, which form energy levels close to the valence band maximum[4].

A cations do not contribute directly to the band edges. The band gap of these materials can be tuned by varying the halide component, X. As the halides are changed from iodide to bromide and bromide to chloride the band gap increases. Perovskites with

specific band gaps can be prepared by mixing the halides in the required ratios[5]. These band-gap tuned perovskites find its applications in tandem solar cells and light emitting devices[6–8]. Even though the cations don't have a direct effect on the band gap, cations can affect the tilt, expansion or contraction of the lead halide octahedra. This can in turn vary the band structure of the material. In short, cations have an indirect contribution to the band gap of the material[9].

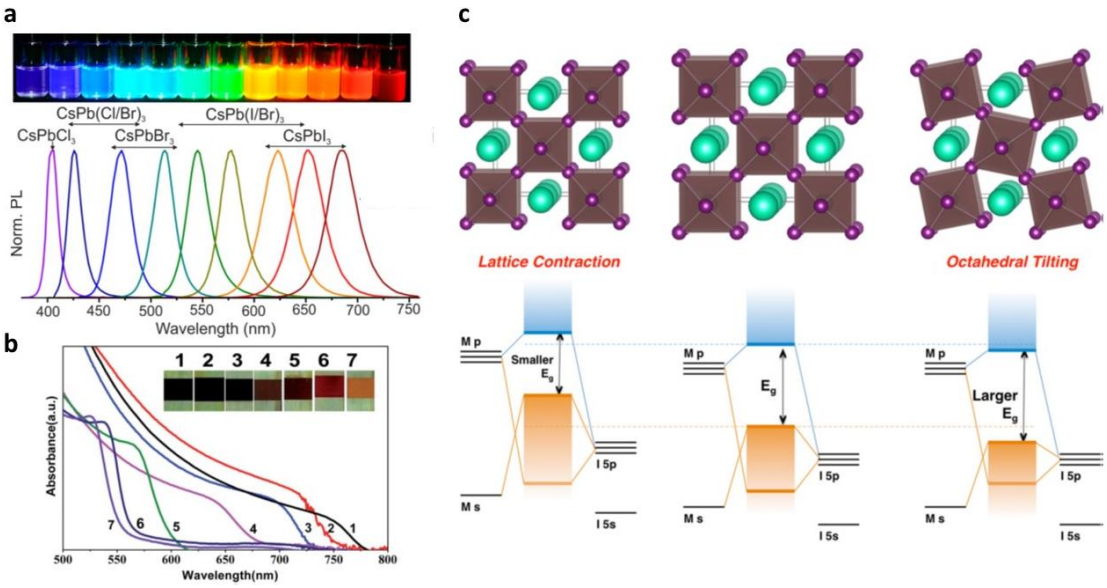

Figure 2.3: (a) Composition tuned band gap of lead perovskite nanocrystals with emissions spanning the visible spectrum, (b) UV-Visible absorption spectra of mixed halide hybrid lead perovskites, (c) Effect of cations on the size and tilt of lead / tin halide octahedra of perovskites and the resulting variation in band structure[5–7].

If the sizes of the cations go beyond a particular limit, they cannot be accommodated in the cuboctahedron cavities formed by the 3-dimensional lead iodide network. The larger cations break the 3D lead iodide network to 2D and 1D structures. 2D sheet structures are formed by the corner shared $[PbI_6]^{4-}$ octahedra to form Ruddlesden-Popper (RP) or Dion-Jacobson (DJ) perovskites[10,11]. RP perovskites have a general formula $A_{n-1}A^*_2B_nX_{3n+1}$ where A^* is a bulky organic aliphatic or aromatic alkylammonium cation. DJ perovskites have a general formula of $A_{n-1}A^*B_nX_{3n+1}$ and here the larger cation A^* attaches to two 2D sheet structures of $[PbI_6]^{4-}$ octahedra. 1D

perovskites have a general formula of $A_nA_2^*B_nX_{3n+2}$ whereas 0D perovskites have a formula $A_{n-1}A_2^*B_nX_{3n+3}$ which consist of isolated $[PbI_6]^{4-}$ octahedra[12]. Lower dimensional perovskites can be pure dimensional or multi-dimensional. 2D perovskite octahedral planes form quantum well structures with the bulky cations forming the high bandgap region. By varying the number of 2D plane sheets the width as well as optoelectronic properties of the quantum well structures can be tuned[13,14].

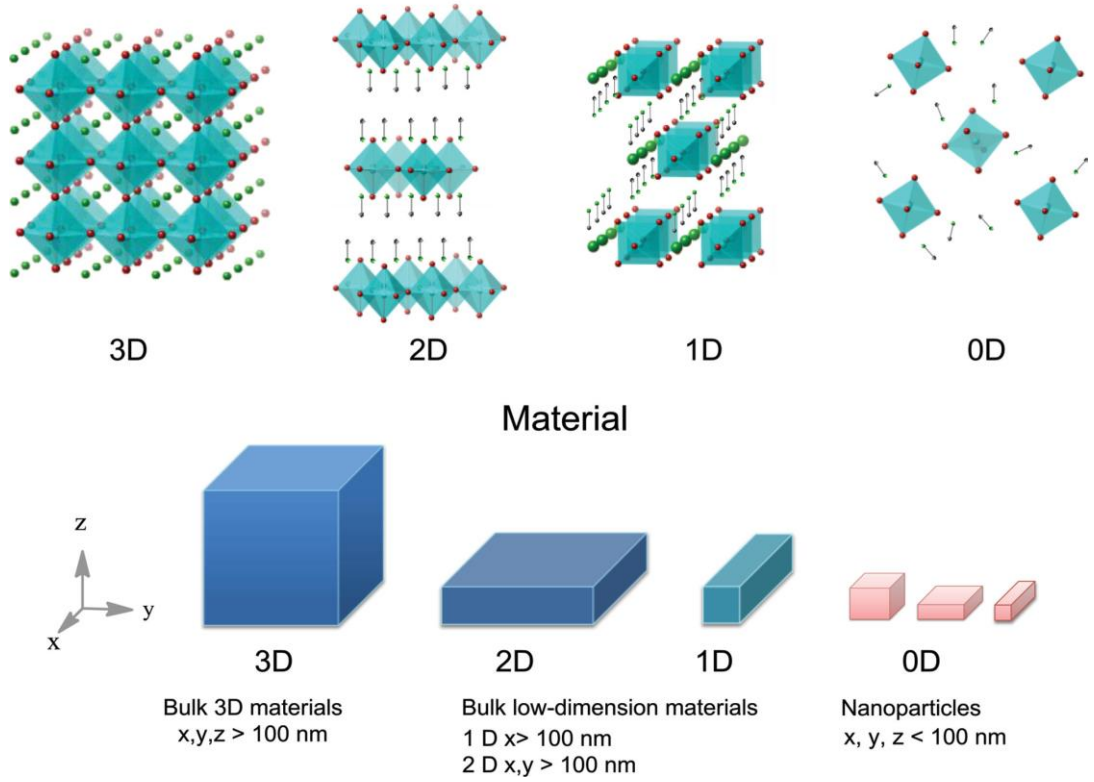

Figure 2.4: Lead halide perovskite frameworks with different dimensionalities and charge carrier confinements[12].

2.2 Crystallization Techniques of Lead Halide Perovskites.

Lead halide perovskites have found its applications on a plethora of electronic and optoelectronic devices. The most important attribute that aided its widespread application is the fairly simple techniques which can be used for their crystallization. The material is solution processable and doesn't need any high temperature step for its formation unlike normal inorganic semiconductors. The perovskite precursor plays a

very important role in the formation of polycrystalline thin films and bulk monocrystals.

2.2.1 Perovskite Precursor Solution

Polar organic solvents are solvents like dimethyl formamide (DMF), dimethyl sulfoxide (DMSO), γ-butyrolactone (GBL), n-methyl pyrrolidone (NMP) and acetonitrile (ACN)[15–18]. It has been found that perovskite precursors dissolved in common solvents like DMSO and GBL are not exactly solutions but colloids. The precursors form stable complex composites with the solvents used to dissolve them[19].

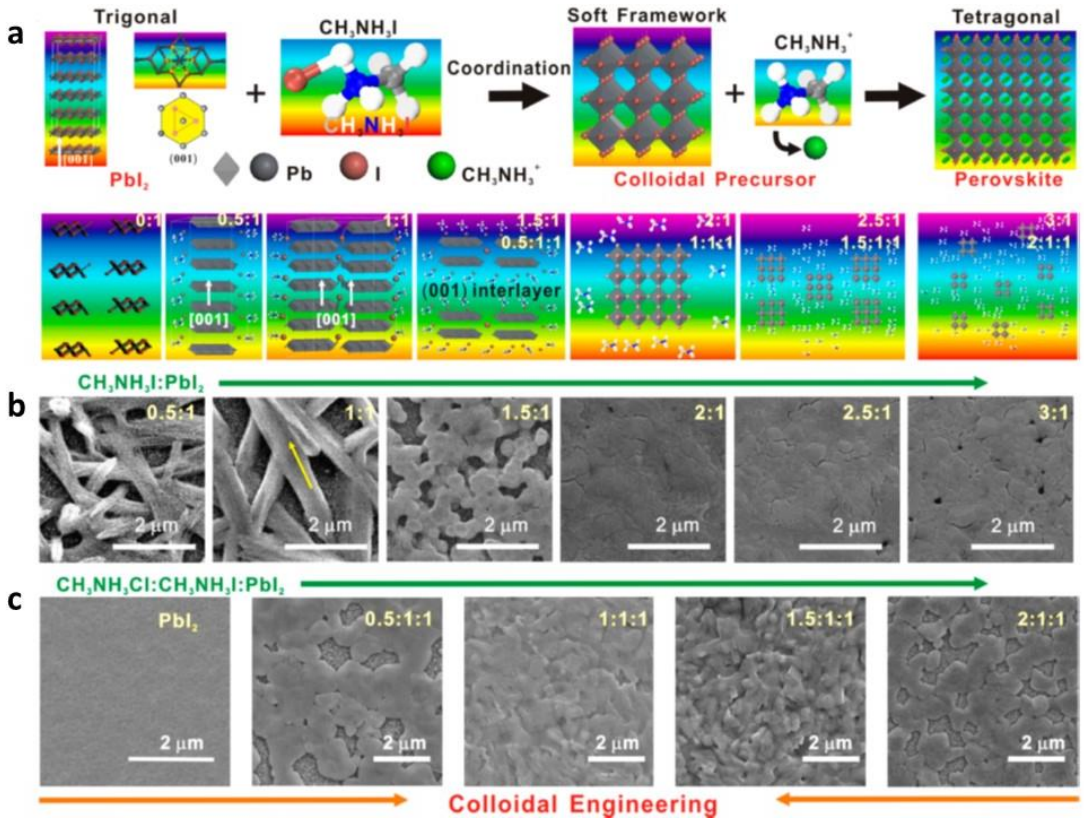

Figure 2.5: (a) Co-ordination of perovskite precursors with solvents and the formation of colloids, (b) Variation in spin coated thin film morphology for various precursor ratios, (c) Variation in film morphology with addition of methylammonium chloride to $MAPbI_3$ precursor[19].

The sizes of these colloids can be varied by varying precursor ratios. The size and nature of the colloids affect the morphology and crystallinity upon film coating process and in turn alter the device characteristics[19,20]. Solvent solute co-ordination was also found to play a critical role in the crystallization of lead halide perovskites. Gutmann's donor number (D_N) of the solvent was used as a parameter to measure their ability to co-ordinate with Pb^{2+} ions and their solvents. The solvents with higher D_N provides a better control over the crystallization process and the resultant film morphology[21]. Solvent co-ordination was found to have a significant effect on other thin film deposition processes like blade coating and sequential deposition. Selecting proper solvents can accelerate as well as retard the rate of crystallization and can be used to tune the optoelectronic device characteristics[22,23].

Solvents and solvent co-ordination also affect the growth of single crystals of lead halide perovskites. It has been found that perovskites show retrograde solubilities with temperature in specific solvents which is explained in the following section.

2.2.2 Inverse Temperature (ITC) and Anti-solvent Vapor crystallization (AVC)

Normally, ionic materials dissociate into constituent ions upon dissolution in solvents. The increased kinetic energy of the solvent molecules at elevated temperatures allows the solvent to easily break up the solute molecules which are adhered together by intermolecular and intramolecular forces.

In the case of lead halide perovskites, it was found that the solubility reduces with temperature and at elevated temperatures the material crystallizes out[24]. This method of crystallization was termed as inverse temperature crystallization (ITC). Initially the ITC technique was reported for $MAPbBr_3$ and $MAPbI_3$ crystals. The technique was found to be solvent dependent. $MAPbBr_3$ showed ITC in DMF while $MAPbI_3$ exhibited it in GBL. Later on the technique was extended to $MAPbCl_3$ single crystals as well, with a 1:1 mixture of DMF and DMSO used as the solvent[25]. The process for formamidinium (FA) based lead halides were also developed and all these crystal growth techniques showed rapid crystal growth rates. Even though the crystallization processes were rapid, the crystals showed extremely low trap densities and superior

optoelectronic properties, even comparable to monocrystalline silicon[26,27]. A number of modified ITC techniques were reported for mixed halide and 2D perovskites[28,29]. It was found that modifying the surface tension of the precursors lead to non-symmetric crystals[29,30]. Thin wafers of lead halide perovskites were grown by modifying the surface energies of precursors.

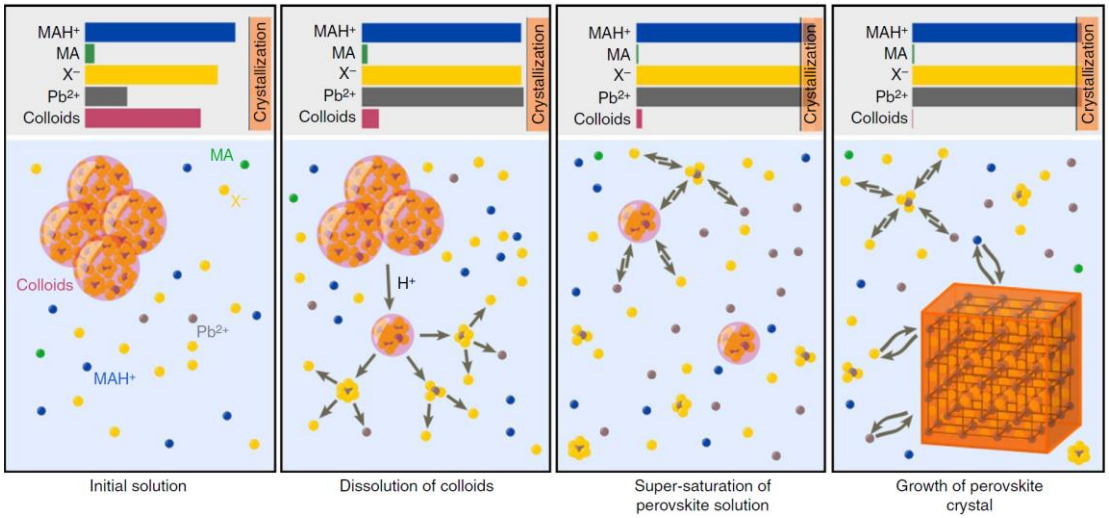

Figure 2.6: The mechanism of retrograde solubility with temperature and crystallization of hybrid lead halide perovskites by ITC[31].

There are very few works investigating the mechanism of retrograde solubility with temperature and inverse temperature crystallization of lead halide perovskites. It was found that the stable colloidal nature of the precursors was the reason for its retrograde solubility. As temperature was increased the colloids which were stable at lower temperatures disintegrate and break up, thereby increasing the ionic concentration. As the ionic concentration is increased and supersaturation is reached, the material crystallizes out[31]. Atomistic mechanism of the nucleation step of $MAPbI_3$ in GBL was studied using well-tempered metadynamics (WTMetaD). The simulation revealed that Pb_2^+ and I^- ions form a PbI_2 like cluster along with the solvent. This is followed with diffusion of MA^+ ions to the cluster to form $MAPbI_3$ nuclei[32].

Lead halide perovskites were also crystallized by anti-solvent vapor crystallization techniques (AVC), where a bad solvent is made to evaporate slowly to perovskite

precursors kept in crystallization dishes[33]. The bad solvent drives out the good solvent creating supersaturation and crystallization. AVC was used to grow cubic $MAPbI_3$ crystals by adding traces of larger cations like ethylammonium iodide in the precursor[34]. Monocrystalline layers of $MAPbBr_3$ were grown on substrates by promoting heterogeneous nucleation on the substrates. An ultrasound pulse was used to initiate the heterogeneous nucleation by microbubble implosions[35]. These monocrystalline films were a few mm in lateral dimensions and cannot be used for fabricating large area optoelectronic devices.

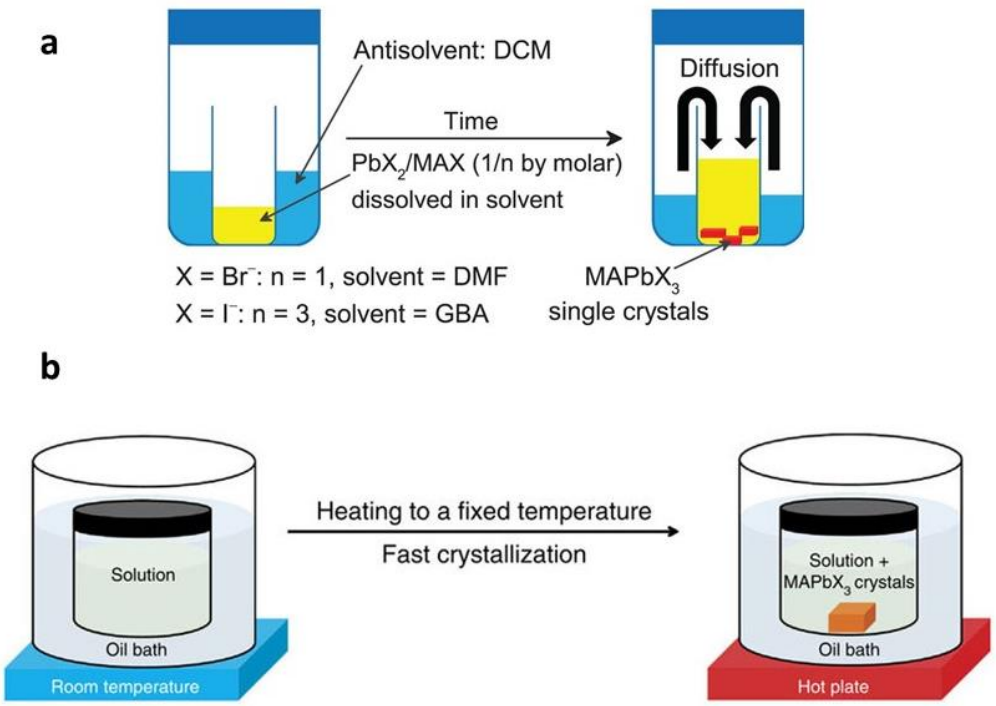

Figure 2.7: Schematic illustration of crystallization techniques of lead halide perovskites (a) Anti-solvent vapor crystallization (AVC), (b) Inverse temperature crystallization (ITC)[24,33].

2.2.3 Crystallization by Spin Coating and Crystal Growth on Substrates

For photovoltaic cells, spin coating is the most widely used technique for forming the perovskite polycrystalline film. Here, the precursor is spun on substrates to form a uniform coating and later the perovskite is crystallized upon annealing.

A number of methods were implemented to improve the crystallinity of spin coated polycrystalline thin films in perovskite devices. Crystallinity, orientation and morphology of thin films were modified by varying annealing temperatures[36], including additives in the precursors and anti-solvents[37,38], solvent engineering[39,40], solvent annealing[41], and so on. It was found that annealing at higher temperatures for shorter duration significantly increases the grain sizes of polycrystalline films[36].

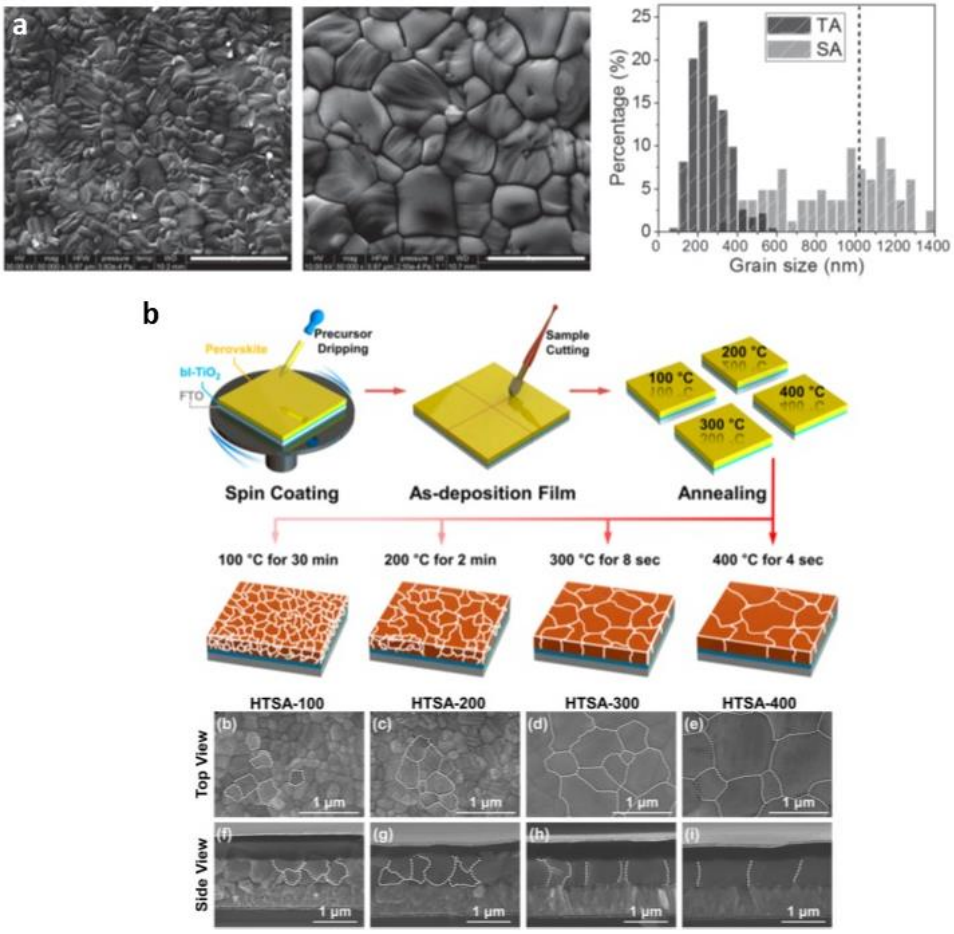

Figure 2.8: (a) Enhanced crystallinity of polycrystalline $MAPbI_3$ with solvent annealing, (b) Enhanced crystallinity of perovskite layer with high temperature short time annealing[36,41].

A plethora of additives were added to perovskite precursors to improve its crystallinity. The additives used in precursors include carbon based additives like graphene nanofibers[42], graphene oxide[37]; polymers like polystyrene[43], poly(4-vinylpyridine)[44];

other additives like ammonium thiocyanate[45], formamidinium acetate[46] and so on. Additives used in anti-solvents were also found to improve the crystallinity and morphology of perovskite layers. These additives include acids like acetic acid[38], polymers like poly(methyl methacrylate)[47] etc. Crystallinity and grain sizes were significantly modified by techniques like methylamine gas treatment[48] and solvent annealing procedures[41,49]. Even surface modification of the electron transporting layer were found to have effects on the crystallinity of perovskite layers spin coated over them[50–52]. Interface engineering was used to initiate the nucleation on the substrate surface itself and thereby increasing the material crystallinity.

Even though there are several works on the growth of bulk single crystals and improving the crystallinity of polycrystalline films, there are very few works on the growth of thin crystal wafers for the fabrication of optoelectronic devices. AVC was modified with an ultrasound pulse to grow μm thick $MAPbBr_3$ crystals over substrates. The crystals had a lateral dimension of a few millimeters[35].

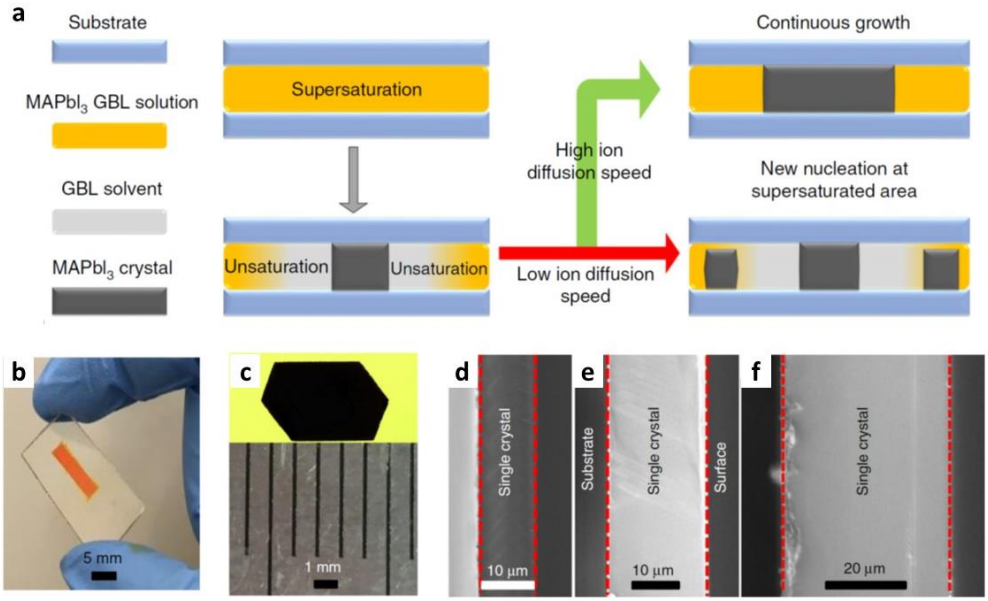

Figure 2.9: (a) Space confined growth of lead halide perovskites thin crystals between two substrates. High diffusion of ions results in continuous growth of large crystals. (b)$MAPBBr_3$, (c) $MAPbI_3$ thin crystals grown by space confined ITC. (d, e and f) thickness of thin crystals can be varied by varying the thickness of spacers between the substrates[53].

Single crystal thin films of $MAPbCl_3$, $MAPbBr_3$, $MAPbI_3$ were grown in between two substrates by top seeded solution growth technique. The lateral dimensions of these crystals were very low to fabricate photovoltaic cells[54]. The lateral dimensions of thin $MAPbI_3$ crystals were increased by modifying the surface energy of the substrates used for the space confined growth technique[53]. The $MAPbI_3$ solar cells fabricated by these thin crystals had an efficiency around 18 %. The crystal growth technique was optimized later on to enhance the device efficiencies above 21 %[55,56]. The space confined growth were applied for fully inorganic $CsPbCl_3$ crystals as well, for fabricating monocrystalline photodetectors[57]. Space confined ITC were used to grow $MAPbBr_3$ crystals of different morphologies from 2D square sheets to 1D wires[58]. All these crystals had lateral dimensions above a few millimeters and were unable to scale up in sizes.

Spin coating techniques were modified to grow highly crystalline and oriented thin films of $MAPbBr_3$ and $MAPbI_3$ over substrates[59,60]. Highly crystalline and oriented films of lead halide perovskites can be deposited over large areas by modified spin coating methods. They can mimic the properties of single crystals and may be used for large area devices with monocrystalline device performances.

2.3 Theory of Nucleation and Epitaxial Growth of Crystals

Lead halide perovskites form polycrystalline films of varying levels of crystallinity upon the film formation process. The first stage in any crystallization process is nucleation, where a new thermodynamic phase or a new structure spontaneously form from the precursors. The nucleation is a stochastic process starting from the state of metastability[61,62]. During nucleation, a small number of ions, atoms or molecules get arranged, forming a site where additional particles are deposited as the particle grows in dimension. The nucleation process can be broadly classified as homogeneous and heterogeneous nucleation. In homogeneous nucleation, same kinds of particles agglomerate upon supersaturation and start growing in dimensions. In heterogeneous nucleation, the agglomeration takes place on other materials like impurities or interfaces. Both these nucleation processes have to overcome a free energy barrier

(ΔG^*) to sustain the crystal growth[63]. In the case of thin film crystallization the crystallites grow in dimensions until they intersect their adjacent crystallites to form well defined grains[64,65]. A detailed explanation on the processes of nucleation and growth is provided in the following chapters.

The crystal growth over crystalline substrates, in which the newly grown crystalline layers formed are in a well-defined orientation with respect to the substrate is termed as epitaxial growth[66]. The formed crystalline film is termed as epitaxial layer. The process is widely used in fabrication of conventional semiconductor devices[67]. There are different modes of epitaxial thin film growth. In Volmer-Weber (VW) mode, the deposited adatom-adatom interaction supersedes adatom-substrate interaction. It leads to the formation of island like 3 dimensional clusters of adatoms. If the adatom-substrate interaction is significantly higher than the inter-adatom interaction, adatoms will preferentially attach to the substrate forming atomically smooth layer of atoms over the substrate. This growth process is termed as Frank van der Merwe (FM) mode. An intermediate situation, when the island formation occurs after a critical thickness of 2D layer formation is called Stranski-Krastanov (SK) growth mode[68].

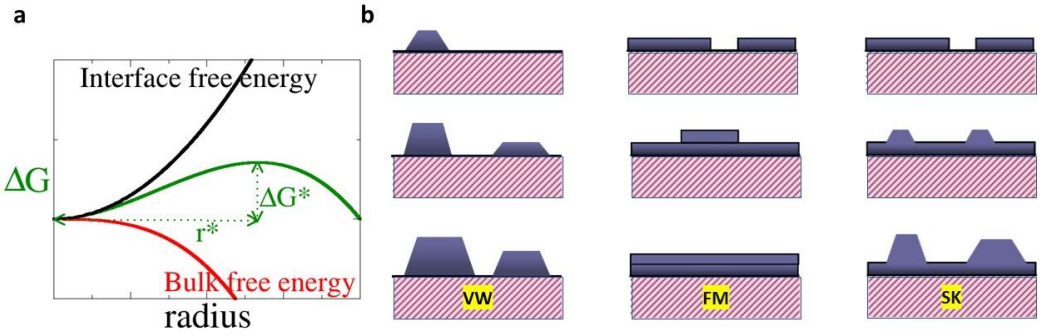

Figure 2.10: (a) The bulk free energy competes with surface free energy of the nuclei. The nucleation process has to overcome a free energy barrier of ΔG*, (b) Different growth modes of epitaxial layer formation.

Conventional epitaxial growth requires substrates to be lattice matched with the epitaxial layer to be grown. Hence the process is highly substrate selective and is its major shortcoming. However, there are a few reports where highly oriented thin

crystals of materials were grown amorphous substrates. In 1978, crystallites of KCl with [100] orientation were grown over amorphous silicon substrates. The surface of the substrate was modified by creating grating microstructures and the direction of growth of [100] plane was parallel to the grating axis[69]. TiO_2 epitaxial thin films were grown over amorphous glass substrates by lateral solid phase epitaxy. The crystals had an out of plane orientation of [001] and had lateral sizes of 10 μm approximately[70]. InP epitaxial layers were grown on amorphous SiO_2 substrates and the performances of photodetectors as well as transistors fabricated employing them were comparable to the conventional state of the art epitaxially grown devices[71]. Epitaxial CdTe thin films were grown by MOCVD on amorphous SiO_2 by using a single crystalline graphene as a buffer layer in between. The grown CdTe had [111] out of plane orientation[72].

There are very limited number of reports on the growth of highly oriented and epitaxial lead halide perovskite films on device substrates[73]. Since optoelectronic properties of semiconductors are highly dependent on its crystal orientation, growth of highly oriented films of lead halide perovskites merits sublime importance[74–76].

2.4 Optoelectronic Applications of Lead Halide Perovskites

Lead halide perovskites have exceptional material properties when compared to other electronic and optoelectronic materials. As a result of these properties perovskites have found a wide range of applications.

2.4.1 Remarkable Optoelectronic Properties of Lead Halide Perovskites

The optoelectronic properties which make this material so versatile include, tunable bandgap, high absorption coefficient, defect tolerance or low defect density, larger carrier lifetimes and diffusion lengths and low exciton binding energy.

As explained in the previous section, lead halide perovskites have tunable bandgaps and the bandgaps can be significantly varied by varying halide composition[5]. The pure iodide-based perovskites like $MAPbI_3$ have optimal bandgaps to be used for photovoltaic devices. $MAPbI_3$ has an absorption coefficient $\sim 10^5$ cm^{-1} at a wavelength

of 450 nm which is significantly higher than most of the conventional inorganic semi-conductors[77]. Similar to the defect tolerance of lead halide perovskites as explained before, the high absorption coefficient of the material can also be traced back to its band structure. The optical absorption in materials results from valence band to conduction band transitions. As explained before, the valence and conduction band edges are formed by hybridization of p-orbital of iodine and s, p-orbitals of lead. The inter-band p to p transitions in $MAPbI_3$ are more efficient when compared to s to p transitions, as p-orbitals exhibit less dispersion than s-orbitals[78]. Since the material has a higher absorption coefficient resulting from its higher joint density of states, a very thin layer of $MAPbI_3$ can be used to absorb photons of the entire solar spectrum.

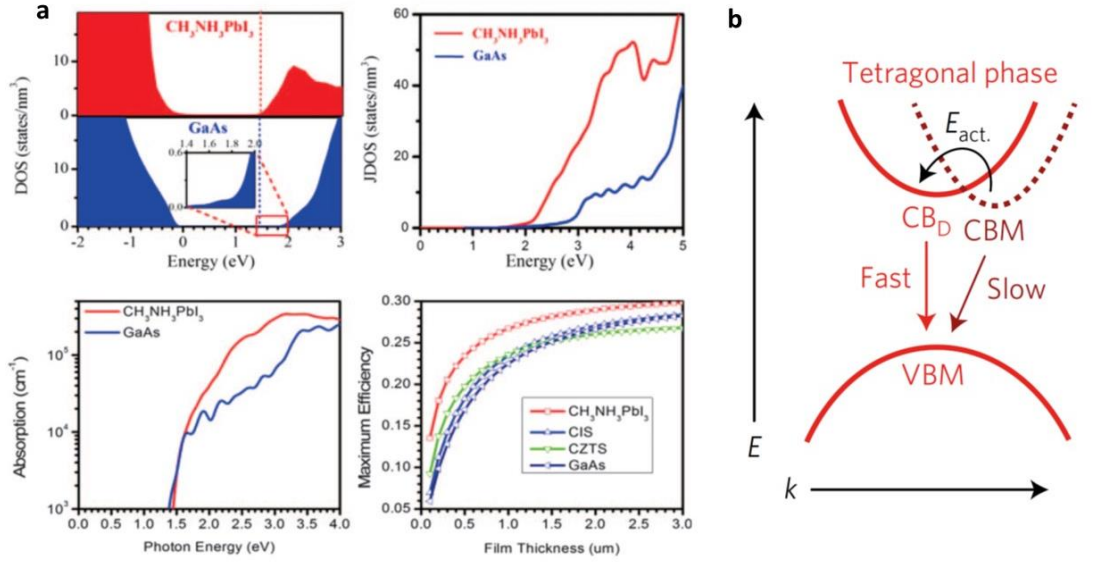

Figure 2.11: (a) Density of states of $MAPbI_3$ in comparison with GaAs. $MAPbI_3$ has a higher joint density of states when compared to GaAs and a thinner layer of $MAPbI_3$ can be used to absorb photons of the entire solar spectrum. (b) The direct-indirect band structure of tetragonal $MAPbI_3$, with the conduction band minimum at a small offset in *k*-space with respect to valence band maximum[78,79].

Studies showed that the band gap of tetragonal (room temperature) $MAPbI_3$ has a direct-indirect nature, with its conduction band minimum (CBM) slightly shifted in k-space, with respect to its valence band maximum (VBM)[79]. The slight indirect nature

of the band gap will have a significant effect on the lifetimes of photogenerated carriers. Along with the defect tolerant nature of the material $MAPbI_3$ exhibits very long photo carrier lifetimes and large carrier diffusion lengths. The measured diffusion length for this class of materials ranges from around 1 μm in the thin films to over 175 μm in single crystals[80,81]. The high absorption cross-section and relatively low exciton binding energies make this material a perfect choice for photovoltaics. The exciton binding energy of methylammonium lead iodide is found to be as low as 16meV at low temperatures. It results in spontaneous free charge carrier generation up on photon absorption[82]. The density functional theory analysis of lead iodide perovskite estimated the effective masses of electrons and holes to be 0.23 m_0 and 0.29 m_0 respectively. This leads to an easy and balanced transport of electrons and holes through the material[83]. All these material properties of hybrid perovskite are comparable to that of high purity inorganic semiconductors synthesized and processed by high cost and energy intensive technologies. These factors make it the material for the next generation photovoltaics.

2.4.2 Hybrid Lead Halide Perovskites for Thin Film Photovoltaics

The process of photosynthesis always fascinated the world and researchers tried to mimic this process to harness energy from the ultimate energy source, the sun[84]. This led to the development of the so-called dye sensitized cells, where a pigment resembling the chlorophyll absorb the solar energy and converts it to electric energy[85]. Hybrid lead perovskites found its way to photovoltaics in 2009, when T. Miyasaka and co-workers used methylammonium lead bromide and iodide to replace the then commonly used dyes[86]. The devices fabricated by them yielded an efficiency of above 3 %. The nano sized particles of the hybrid lead halide perovskites coated on mesoporous TiO_2 layer were used as a sensitizer to absorb light from the solar spectrum. The device however suffered from severe room ambient stability issues. An organic solution containing lithium halide and halogen was used as the electrolyte. The usage of such a liquid electrolyte had serious effects on the robustness of the device. The turning point of hybrid perovskite solar cells happened in 2012, when Nam-Gyu Park and group replaced the liquid electrolyte with a solid hole transporting material

(HTM)[87]. The usage of Spiro-OMeTAD, the solid HTM not only gave robustness to the device but also boosted the efficiency up to 9 %. The device was also characterized by high photocurrents (exceeding 17 mA/cm^2). These devices also had superior stability (up to 500 hours) in room ambience. This work established the hybrid lead halide perovskite system as one of the widely sought-after material for photovoltaics. It resulted in intensive research activities centered on this class of materials.

Over the course of few years, several modifications were done, both to material processing and device fabricating methods. H. Snaith and coworkers employed a meso-superstructured configuration in which a layer of mesoporous Al_2O_3 was coated over the compact TiO_2 and these devices showed high photo-voltages over 1.1 volts[88]. A wide variety of electron extraction layers like ZnO and SnO_2 were also tried in place of TiO_2[89,90]. Usage of these materials also reduced the processing temperature without compromising for the efficiency of the device and thereby reducing the energy payback time of the device. Planar devices were introduced where the device stack is made without any mesoscopic material layer. The initial efficiencies of these planar devices were lower when compared to mesoscopic devices. By careful control of interfaces in the devices and tuning the morphology of the perovskite films, Hagfeldt and coworkers were successful in attaining planar device efficiencies very close to that of mesoscopic devices[91].

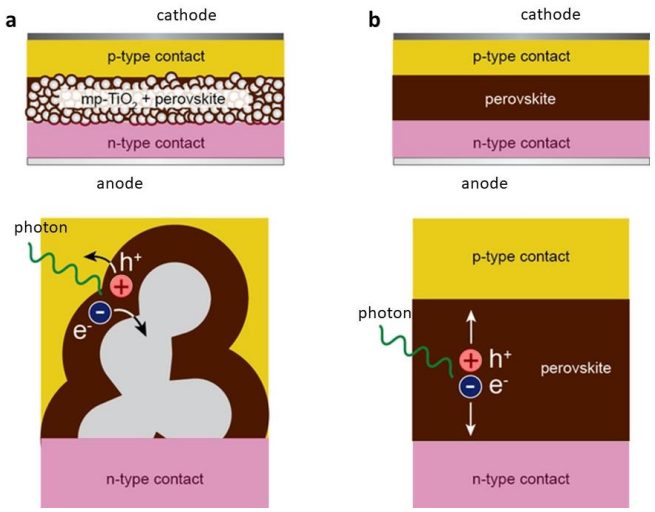

Figure 2.12: The two commonly used device architectures of perovskite solar cells (a) Mesoporous architecture, (b) Planar architecture.

Because of intense research activities in the area, hybrid lead halide perovskite solar cells reached a 'stellar' efficiency of 25.2 % in 2020[92]. It should be noted that the widely commercialized Silicon based solar cells took decades to reach a record efficiency of above 25 %[92]. Presently, hybrid perovskite solar cells are the hottest area of research in photovoltaics[93].

2.4.3 Thin Film photodetectors and Other Optoelectronic Devices

As explained in the case of photovoltaic cells, lead halide perovskites have all the material properties needed to be used as a light absorber in photodetectors. Photodetectors are a class of devices including photoconductors, photodiodes and phototransistors. All these device configurations have been reported for lead halide perovskites. The three important figures of merit used to evaluate a photodetector include responsivity (*R*), detectivity (*D**) and response time (τ) (a detailed explanation is given in the following chapters)

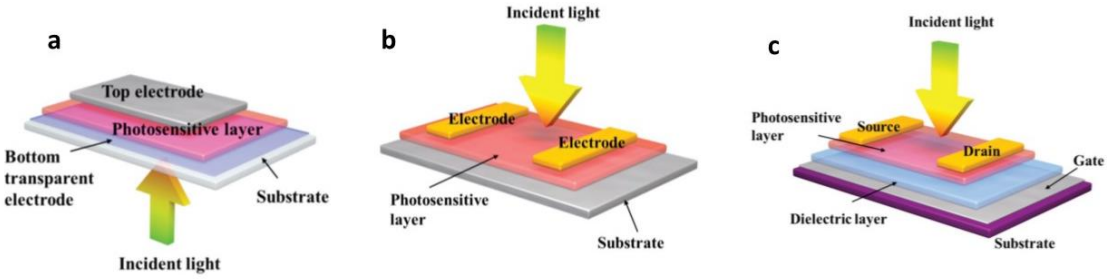

Figure 2.13: Different photodetector configurations (a) Photodiode, (b) Photoconductor, (c) Phototransistor[94].

The first reported 3D perovskite based photodetectors used a spin coated perovskite layer on polyethylene terephthalate (PET) substrate patterned with planar ITO electrodes[95]. The device showed a responsivity of 3.49 AW^{-1} in the UV regime. The first vertical photodetector device used a $MAPbI_{3-x}Cl_x$ absorber sandwiched between PEDOT: PSS and PCBM as HTM and ETL. The device showed an excellent detectivity of 10^{14} Jones. These devices also showed faster response times (τ_{rise} = 180 μs and τ_{fall}

= 160 μs)[96]. Numerous photodetectors were fabricated following these works exhibiting state of the art device characteristics. $MAPbI_3$ based phototransistors were fabricated with SiO_2 used as the gate dielectric and Au as source/drain electrodes[97]. The responsivity of these photodetectors reached 320 AW^{-1} for white light illuminations, which was among the largest reported values for phototransistors. Photodetectors with a device configuration ITO/$MAPbI_3$/TDP-Si_2/MoO_3/Ag was fabricated in 2015. These devices showed impressive response times of 10 μs rise-time and a fall-time of 5.7 μs. The device had a responsivity of 242 AW^{-1} at 740 nm[98]. 2D Ruddlesden Popper perovskites like $(C_4H_9NH_3)_2PbBr_4$ and perovskite nanocrystals were also used for photodetector applications[99–101]. Perovskite nanocrystals were mainly used as light absorber in phototransistor configurations. Apart from photodetectors, perovskite thin films have found its applications in other electronic devices like LEDs, lasing, transistors etc. The first room temperature light emission from perovskite LEDs were reported in 2014. A 15 nm thick $CH_3NH_3PbBr_3$ and $CH_3NH_3PbI_{3-x}Cl_x$ were used as the emissive layer[102]. By varying the halide composition, they also showed that the PL emission can be set at green and infra-red wavelengths. The first light emitting field effect transistor was demonstrated at 77 K by Soci et al. in 2015[103]. Lead halide perovskites have also found their application in neuromorphic computing devices which can combine data storage and processing capabilities[104].

2.4.4 Perovskite Single Crystal Based Devices

Owing to the complexity of fabrication processes, the number of perovskite single crystal based devices reported so far is considerably lower than normal polycrystalline thin film optoelectronic devices.

For fabricating photovoltaic cells using single crystals, the thickness of the crystal should be less than the diffusion lengths of the charge carriers. It implies that the crystals should grow in an asymmetric manner, with the growth happening in planar 2 dimensions and confined in the 3rd dimension. Thin crystals of $MAPbBr_3$ were asymmetrically grown on device substrates by a cavitation triggered crystallization

technique to fabricate photovoltaic cells. An ETL/HTM free solar cells (ITO/$MAPbBr_3$/Au) was fabricated with > 5 % efficiency and almost 100 % internal quantum efficiency[105]. $MAPbBr_3$ crystals grown by space confined growth with a device configuration, FTO/TiO_2/$MAPbBr_3$/HTM/Au yielded an efficiency above 7 %[106]. Single crystals of $MAPbI_3$ were first employed as light absorber in photovoltaics in 2017. The single crystals with lateral dimensions of 5 mm and thickness ranging from 10 to 40 μm were grown on device substrates. They were employed in solar cells having ITO/PTAA/$MAPbI_3$/PCBM/C_{60}/BCP/Cu with an efficiency around 18 % for 10 μm thick crystals[53]. A further optimized space confined growth technique with device structure ITO/PTAA/$MAPbI_3$/C_{60}/BCP/Cu pushed the efficiency above 21 %[56,107].

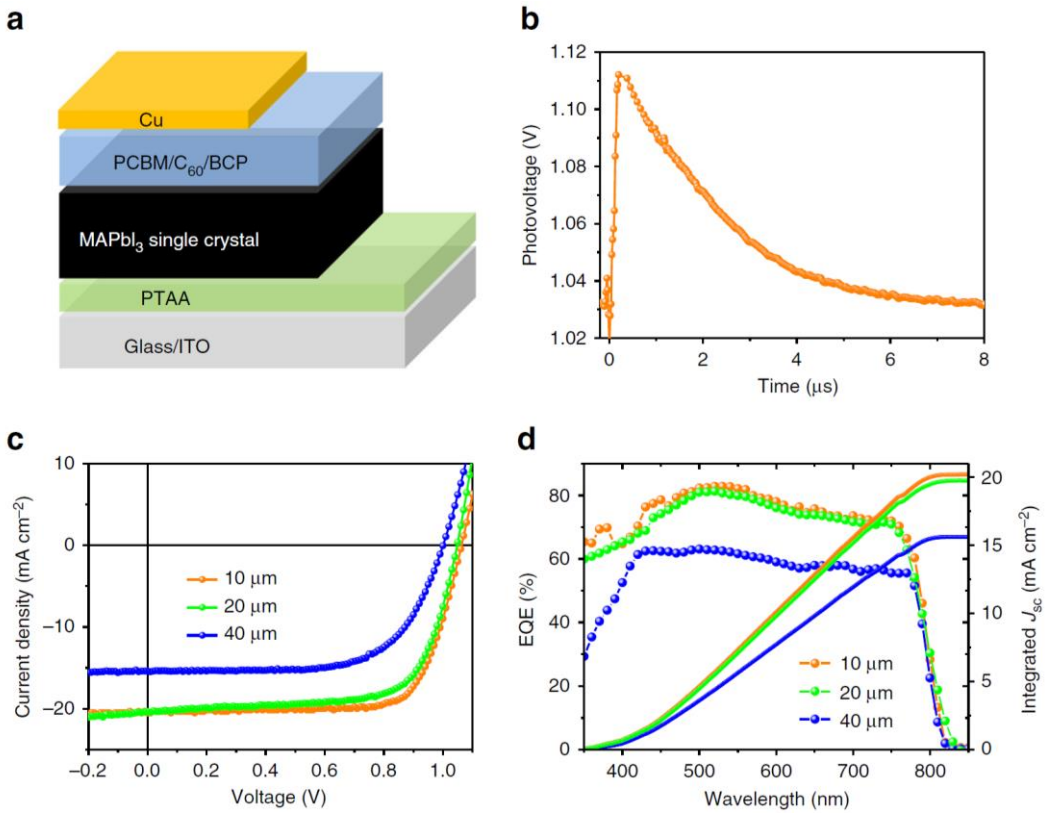

Figure 2.14: (a) Device architecture of a typical single crystal solar cell, (b) Transient photovoltaic curve of single crystal solar cell under 1 sun illumination, (c) Current density – voltage curve and (d) external quantum efficiency of single crystal solar cells with different crystal thicknesses[53].

In 2017 single crystal $MAPbBr_3$ micro-platelets were used to fabricate LEDs with green emissions. The device had a very simple structure of ITO/$MAPbBr_3$/Au. Low temperature electroluminescence was achieved by freezing the ionic motion and the device showed a stable luminescence of 5000 cdm^{-2} for 24 hours without degradation[108]. Single crystals of lead halide perovskites can be easily applied in photoconductors owing to its simple device configurations. $MAPbI_3$ single crystal-based broadband photodetectors were fabricated by depositing Au electrodes on [100] plane of the crystal by vacuum deposition[109]. The devices showed a responsivity of 953 AW^{-1}. A planar substrate integrated MAPbBr3 based photodetector was fabricated in photoconductor configuration with interdigitated ITO as electrodes[110]. The devices showed an excellent responsivity over 4000 AW^{-1}. $FAPbI_3$ bulk single crystals were grown by ITC and were sliced down to thin wafers mechanically. Interdigitated Au electrodes were deposited by thermal evaporation to fabricate an array of photodetectors[111].Thin crystals of $MAPbI_3$ were grown in a microreactor system by modifying ITC to fabricate photodetector arrays. The array of photodetectors fabricated had very high photocurrents[112]. Apart from these broadband photodetectors, perovskite bulk crystals were employed in narrow-band photodetectors as well. A perovskite micro-crystalline film was deposited on interdigitated ITO/glass substrate. When illuminated from the crystal side, the device worked as a narrow band photodetector[113]. A perovskite single crystal sandwiched between two electrodes, Au and Ga can also act as a narrowband photodetector with very sharp response peak (20 nm FWHM)[114]. The thin layer of Au acts as the transparent electrode. The photogenerated carriers with excitation wavelengths significantly higher than the bandgap of the material are trapped by the surface traps of the crystals and do not generate photocurrents. Perovskite single crystal films with controlled thickness were printed with a facile seed printing strategy on device substrates. Owing to the state of the art device characteristics of lead halide perovskite single crystal photodetectors, a perovskite single crystal image sensor was fabricated and demonstrated by depositing an array of electrodes on top of the crystal[115].

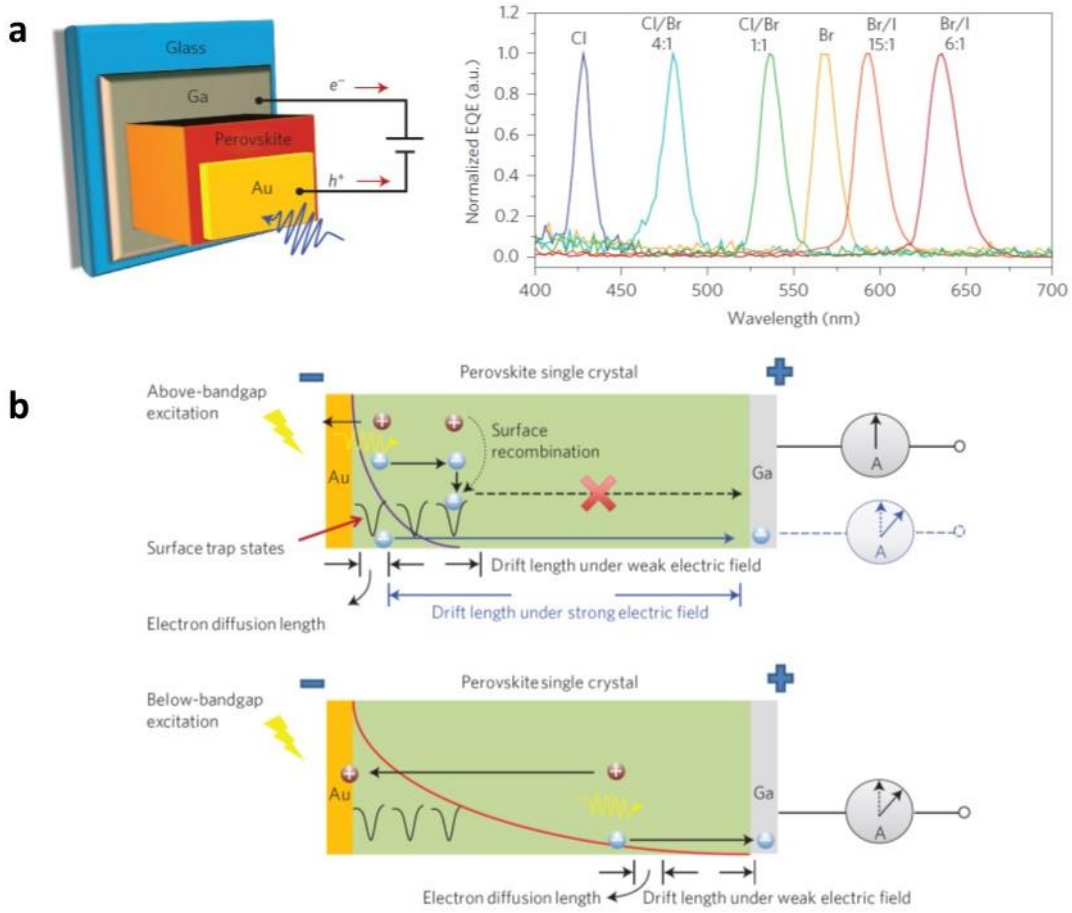

Figure 2.15: (a) The device structure and band pass nature of bulk narrowband photodetectors, (b) The mechanism of photocurrent generation for below bandgap excitations[114].

Lead halide perovskite single crystals were also used in other applications like high energy *X*-ray and *γ*-ray detectors. The single crystal *X*-ray detectors used conventional lead halide perovskites like $MAPbBr_3$ and lead-free perovskites like $Cs_2AgBiBr_6$. The $MAPbBr_3$ *X*-ray detectors were hyper-sensitive and had the potential to reduce the dose by 15 to 120 fold compared to the state of the art systems for *X*-ray imaging[116,117]. $CsPbBr_3$ based *γ*-ray detectors showed high resolution and extremely stable device performances which were even better than the conventional radiation detectors[118]. All these results demonstrate that employing high quality single crystals in optoelectronic devices can enhance their device performances and efficiencies.

2.5 Effects of Crystallinity and Grain Boundaries on Perovskite Thin Film Devices

Though hybrid perovskites have achieved remarkable efficiencies in photovoltaic devices, it suffers from device instability and poor repeatability. The device efficiency also varies with different V-I scans applied on the device and is termed as the device hysteresis. The effect of grain boundaries on PV device performances is still a topic of hot research. There are contradicting results on the effect of crystal grains on perovskite device characteristics. Initial studies conducted by Yun et al. by using Kelvin Probe Force Microscopy (KPFM) and Conducting Atomic Force Microscopy (C-AFM) revealed that higher photo-voltage and short circuit photocurrent are obtained along the grain boundaries, thus confirming the beneficial role of grain boundaries in efficient photogenerated charge collection[119]. KPFM measurement also revealed existence of a potential barrier along the grain boundary. They also claimed that the grain boundaries may be beneficial for effectively collecting the photo generated carriers. Later in 2016 an in-depth study by Yun and coworkers revealed that the grain boundaries act as a channel for ion migration. This ionic motion accelerated by the presence of grain boundaries leads to device hysteresis and poor reproducibility of device characteristics[120]. Pulsed voltage – current measurements were carried out on thin films of $MAPbI_3$ with various grain sizes. The study demonstrates that grain boundaries work as a channel for ion migration and engineering the grain boundaries can be used as a strategy to decrease ion migration[121]. Another study done on the effects of grain boundaries on photovoltaic performance indicates that the grain boundaries accelerates the electron hole recombination in $MAPbI_3$ by increasing electron phonon non-adiabatic coupling[122]. The results also showed that chlorine doping of the grain decreases the electron phonon coupling and brings the recombination down. A contradictory result was reported in 2019 that the optoelectronic quality of polycrystalline perovskite films are not necessarily related to the orientation and size of crystalline domains[123]. A work by Snaith and coworkers shows that films with poor crystallinity are less stable towards ambient humidity[124]. According to this work the presence of grain boundaries accelerates the absorption of water molecules and acts as a channel through which the moisture can seep inside the material. The work also revealed that the degradation of the material gets initiated from the grain boundaries.

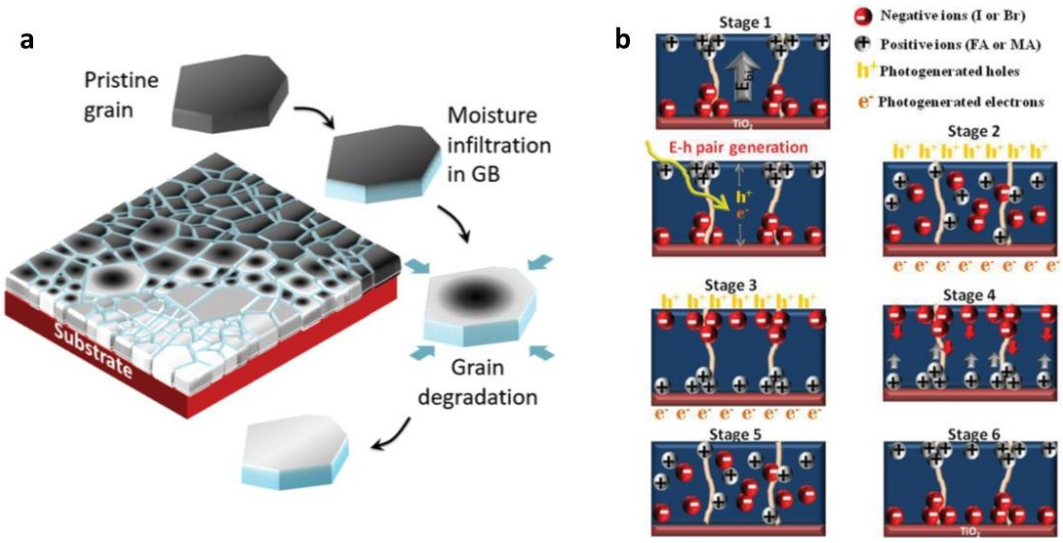

Figure 2.16: (a) The mechanism of moisture ingress and degradation of perovskite thin film, (b) Grain boundary accelerated ion migration in perovskite solar cells[121,124].

By using confocal microscopy imaging, it was confirmed that reduction in grain boundaries results in improved moisture stability and device efficiency for solar cells[125]. Even though grain boundaries are the initiators of moisture ingress and degradation, it was found that grain boundaries have similar photo-responses to the bulk of the crystal. This indicates that microstructures of the film do not have strong effects on the intrinsic photo-response of the material[126]. The work also reported a surprising result that the photo-degradation process begins with bulk grain disintegration and not from the boundaries between grains. Even though there are quite a few papers investigating and discussing the effect of grain boundaries in ionic migration and device hysteresis, many questions are still unanswered. Hence future research has to focus on the following queries: (a) Does ion migration cause device hysteresis? (b) Do the grain boundaries accelerate the ionic migration? (c) Does ionic migration have any adverse effect on device stability?

2.6 References

1. Yin, W.-J., Shi, T. & Yan, Y. Unusual defect physics in $CH_3NH_3PbI_3$ perovskite

solar cell absorber. *Appl. Phys. Lett.* **104**, 063903 (2014).

2. Brandt, R. E., Stevanović, V., Ginley, D. S. & Buonassisi, T. Identifying defect-tolerant semiconductors with high minority-carrier lifetimes: beyond hybrid lead halide perovskites. *MRS Commun.* **5**, 265–275 (2015).

3. Kovalenko, M. V., Protesescu, L. & Bodnarchuk, M. I. Properties and potential optoelectronic applications of lead halide perovskite nanocrystals. *Science* **358**, 745–750 (2017).

4. Kim, J., Lee, S. H., Lee, J. H. & Hong, K. H. The role of intrinsic defects in methylammonium lead iodide perovskite. *J. Phys. Chem. Lett.* **5**, 1312–1317 (2014).

5. Kulkarni, S. A. *et al.* Band-gap tuning of lead halide perovskites using a sequential deposition process. *J. Mater. Chem. A* **2**, 9221–9225 (2014).

6. Sutherland, B. R. & Sargent, E. H. Perovskite photonic sources. *Nat. Photonics* **10**, 295–302 (2016).

7. Protesescu, L. *et al.* Nanocrystals of Cesium Lead Halide Perovskites ($CsPbX_3$, X = Cl, Br, and I): Novel Optoelectronic Materials Showing Bright Emission with Wide Color Gamut. *Nano Lett.* **15**, 3692–3696 (2015).

8. McMeekin, D. P. *et al.* A mixed-cation lead mixed-halide perovskite absorber for tandem solar cells. *Science* **351**, 151–155 (2016).

9. Prasanna, R. *et al.* Band Gap Tuning via Lattice Contraction and Octahedral Tilting in Perovskite Materials for Photovoltaics. *J. Am. Chem. Soc.* **139**, 11117–11124 (2017).

10. Stoumpos, C. C. *et al.* Ruddlesden-Popper Hybrid Lead Iodide Perovskite 2D Homologous Semiconductors. *Chem. Mater.* **28**, 2852–2867 (2016).

11. Mao, L. *et al.* Hybrid Dion-Jacobson 2D Lead Iodide Perovskites. *J. Am. Chem. Soc.* **140**, 3775–3783 (2018).

12. González-Carrero, S., Galian, R. E. & Pérez-Prieto, J. Organometal Halide

Perovskites: Bulk Low-Dimension Materials and Nanoparticles. *Part. Part. Syst. Charact.* **32**, 709–720 (2015).

13. Ahmad, S. *et al.* Dion-Jacobson Phase 2D Layered Perovskites for Solar Cells with Ultrahigh Stability. *Joule* **3**, 794–806 (2019).

14. Wang, N. *et al.* Perovskite light-emitting diodes based on solution-processed self-organized multiple quantum wells. *Nat. Photonics* **10**, 699–704 (2016).

15. Cao, X. *et al.* Fabrication of Perovskite Films with Large Columnar Grains via Solvent-Mediated Ostwald Ripening for Efficient Inverted Perovskite Solar Cells. *ACS Appl. Energy Mater.* **1**, 868–875 (2018).

16. Ahn, N. *et al.* Highly Reproducible Perovskite Solar Cells with Average Efficiency of 18.3 % and Best Efficiency of 19.7 % Fabricated via Lewis Base Adduct of Lead(II) Iodide. *J. Am. Chem. Soc.* **137**, 8696–8699 (2015).

17. Jo, Y. *et al.* High Performance of Planar Perovskite Solar Cells Produced from PbI_2(DMSO) and PbI_2(NMP) Complexes by Intramolecular Exchange. *Adv. Mater. Interfaces* **3**, 1–7 (2016).

18. Noel, N. K. *et al.* A low viscosity, low boiling point, clean solvent system for the rapid crystallisation of highly specular perovskite films. *Energy Environ. Sci.* **10**, 145–152 (2017).

19. Yan, K. *et al.* Hybrid Halide Perovskite Solar Cell Precursors: Colloidal Chemistry and Coordination Engineering behind Device Processing for High Efficiency. *J. Am. Chem. Soc.* **137**, 4460–4468 (2015).

20. Khlyabich, P. P. & Loo, Y. L. Crystalline Intermediates and Their Transformation Kinetics during the Formation of Methylammonium Lead Halide Perovskite Thin Films. *Chem. Mater.* **28**, 9041–9048 (2016).

21. Hamill, J. C., Schwartz, J. & Loo, Y. L. Influence of Solvent Coordination on Hybrid Organic-Inorganic Perovskite Formation. *ACS Energy Lett.* **3**, 92–97 (2018).

22. Deng, Y. *et al.* Tailoring solvent coordination for high-speed, room-temperature blading of perovskite photovoltaic films. *Sci. Adv.* **5**, 1–9 (2019).

23. Wu, Y. *et al.* Retarding the crystallization of PbI_2 for highly reproducible planar-structured perovskite solar cells via sequential deposition. *Energy Environ. Sci.* **7**, 2934–2938 (2014).

24. Saidaminov, M. I. *et al.* High-quality bulk hybrid perovskite single crystals within minutes by inverse temperature crystallization. *Nat. Commun.* **6**, 7586 (2015).

25. Maculan, G. *et al.* $CH_3NH_3PbCl_3$ Single Crystals: Inverse Temperature Crystallization and Visible-Blind UV-Photodetector. *J. Phys. Chem. Lett.* **6**, 3781–3786 (2015).

26. Saidaminov, M. I., Abdelhady, A. L., Maculan, G. & Bakr, O. M. Retrograde solubility of formamidinium and methylammonium lead halide perovskites enabling rapid single crystal growth. *Chem. Commun.* **51**, 17658–17661 (2015).

27. Saidaminov, M. I. *et al.* Planar-integrated single-crystalline perovskite photodetectors. *Nat. Commun.* **6**, 8724 (2015).

28. Wang, W. *et al.* Growth of mixed-halide perovskite single crystals. *CrystEngComm* **20**, 1635–1643 (2018).

29. Liu, Y. *et al.* Surface-Tension-Controlled Crystallization for High-Quality 2D Perovskite Single Crystals for Ultrahigh Photodetection. *Matter* **1**, 465–480 (2019).

30. Zhumekenov, A. A. *et al.* The Role of Surface Tension in the Crystallization of Metal Halide Perovskites. *ACS Energy Lett.* **2**, 1782–1788 (2017).

31. Nayak, P. K. *et al.* Mechanism for rapid growth of organic inorganic halide perovskite crystals. *Nat. Commun.* **7**, 1–8 (2016).

32. Ahlawat, P. *et al.* Atomistic Mechanism of the Nucleation of Methylammonium Lead Iodide Perovskite from Solution. *Chem. Mater.* **32**, 529–536 (2020).

33. Shi, D. *et al.* Low trap-state density and long carrier diffusion in organolead

trihalide perovskite single crystals. *Science* **347**, 519–522 (2015).

34. Peng, W. *et al.* Engineering of $CH_3NH_3PbI_3$ Perovskite Crystals by Alloying Large Organic Cations for Enhanced Thermal Stability and Transport Properties. *Angew. Chemie - Int. Ed.* **55**, 10686–10690 (2016).

35. Peng, W. *et al.* Solution-Grown Monocrystalline Hybrid Perovskite Films for Hole-Transporter-Free Solar Cells. 3383–3390 (2016).

36. Kim, M. *et al.* High-Temperature-Short-Time Annealing Process for High-Performance Large-Area Perovskite Solar Cells. *ACS Nano* **11**, 6057–6064 (2017).

37. Zhang, X. *et al.* Graphene oxide as an additive to improve perovskite film crystallization and morphology for high-efficiency solar cells. *RSC Adv.* **8**, 987–993 (2018).

38. Li, Y. *et al.* Acetic Acid Assisted Crystallization Strategy for High Efficiency and Long-Term Stable Perovskite Solar Cell. *Adv. Sci.* **7**, 1–10 (2020).

39. Jeon, N. J. *et al.* Solvent engineering for high-performance inorganic–organic hybrid perovskite solar cells. *Nat. Mater.* **13**, 897–903 (2014).

40. Chang, C. W., Kwang, Z. W., Hsieh, T. Y., Wei, T. C. & Lu, S. Y. High performance perovskite solar cells fabricated from porous $PbI_{2-x}Br_x$ prepared with mixture solvent pore generation treatment. *Electrochim. Acta* **292**, 399–406 (2018).

41. Xiao, Z. *et al.* Solvent Annealing of Perovskite-Induced Crystal Growth for Photovoltaic-Device Efficiency Enhancement. *Adv. Mater.* **26**, 6503–6509 (2014).

42. Li, Y. & Leung, W. W. F. Introduction of Graphene Nanofibers into the Perovskite Layer of Perovskite Solar Cells. *ChemSusChem* **11**, 2921–2929 (2018).

43. Kim, H. P., Bin Mohd Yusoff, A. R. & Jang, J. Polystyrene enhanced

crystallization of perovskites towards high performance solar cells. *Nanoscale Adv.* **1**, 76–85 (2019).

44. Zuo, L. *et al.* Polymer-modified halide perovskite films for efficient and stable planar heterojunction solar cells. *Sci. Adv.* **3**, 1–12 (2017).

45. Liu, Z. *et al.* Enhanced Crystallinity of Triple-Cation Perovskite Film via Doping NH_4SCN. *Nanoscale Res. Lett.* **14**, (2019).

46. Gao, C. *et al.* Additive engineering to improve the efficiency and stability of inverted planar perovskite solar cells. *J. Mater. Chem. C* **6**, 8234–8241 (2018).

47. Bi, D. *et al.* Polymer-templated nucleation and crystal growth of perovskite films for solar cells with efficiency greater than 21 %. *Nat. Energy* **1**, 1–5 (2016).

48. Seewald, T., Schütz, E. R., Ebenhoch, C. & Schmidt-Mende, L. Curing perovskites—a way towards control of crystallinity and improved stability. *J. Phys. Energy* **2**, 021001 (2020).

49. Liang, Q. *et al.* Enhancing the crystallization and optimizing the orientation of perovskite films via controlling nucleation dynamics. *J. Mater. Chem. A* **4**, 223–232 (2015).

50. Liu, D. *et al.* Improved crystallinity of perovskite via molecularly tailored surface modification of SnO_2. *J. Power Sources* **441**, (2019).

51. Liu, K. *et al.* Fullerene derivative anchored SnO_2 for high-performance perovskite solar cells. *Energy Environ. Sci.* **11**, 3463–3471 (2018).

52. Wang, Y. Q., Xu, S. Bin, Deng, J. G. & Gao, L. Z. Enhancing the efficiency of planar heterojunction perovskite solar cells via interfacial engineering with 3-aminopropyl trimethoxy silane hydrolysate. *R. Soc. Open Sci.* **4**, (2017).

53. Chen, Z. *et al.* Thin single crystal perovskite solar cells to harvest below-bandgap light absorption. *Nat. Commun.* **8**, 1890 (2017).

54. Chen, Y. X. *et al.* General Space-Confined On-Substrate Fabrication of Thickness-Adjustable Hybrid Perovskite Single-Crystalline Thin Films. *J. Am.*

Chem. Soc. **138**, 16196–16199 (2016).

55. Chen, Z. *et al.* Single-Crystal $MAPbI_3$ Perovskite Solar Cells Exceeding 21 % Power Conversion Efficiency. *ACS Energy Lett.* 1258–1259 (2019).

56. Alsalloum, A. Y. *et al.* Low-Temperature Crystallization Enables 21.9 % Efficient Single-Crystal $MAPbI_3$ Inverted Perovskite Solar Cells . *ACS Energy Lett.* **5**, 657–662 (2020).

57. Gui, P. *et al.* Space-Confined Growth of Individual Wide Bandgap Single Crystal $CsPbCl_3$ Microplatelet for Near-Ultraviolet Photodetection. *Small* **15**, 1–6 (2019).

58. Li, Y. *et al.* Confined-solution process for high-quality $CH_3NH_3PbBr_3$ single crystals with controllable morphologies. *Nano Res.* **11**, 3306–3312 (2018).

59. Noel, N. K. *et al.* Highly Crystalline Methylammonium Lead Tribromide Perovskite Films for Efficient Photovoltaic Devices. *ACS Energy Lett.* **3**, 1233–1240 (2018).

60. Cho, N. *et al.* Pure crystal orientation and anisotropic charge transport in large-area hybrid perovskite films. *Nat. Commun.* **7**, 13407 (2016).

61. Venables, J. A., Spiller, G. D. T. & Hanbucken, M. Nucleation and growth of thin films. *Reports Prog. Phys.* **47**, 399–459 (1984).

62. Joop, H. & Sefcik, J. *The Handbook of Continuous Crystallization* (2020).

63. Kashchiev, D. & van Rosmalen, G. M. Review: Nucleation in solutions revisited. *Cryst. Res. Technol.* **38**, 555–574 (2003).

64. Thompson, C. V. Grain growth in thin films. *Annu. Rev. Mater. Sci.* **20**, 245–268 (1990).

65. Thompson, C. V. Structure Evolution During Processing of Polycrystalline Films. *Mater. Sci.* (2000).

66. Bachmann, K. J. Epitaxy. *Encycl. Mater. Sci. Technol.* 2791–2799 (2001).

67. Pohl, U. W. *Epitaxy of Semiconductors Introduction to Physical Principles*.

(2012).

68. Brune, H. Growth Modes. *Encycl. Mater. Sci. Technol.* 3683–3692 (2001).

69. Smith, H. I. & Flanders, D. C. Oriented crystal growth on amorphous substrates using artificial surface-relief gratings. *Appl. Phys. Lett.* **32**, 349–350 (1978).

70. Taira, K. *et al.* Lateral solid-phase epitaxy of oxide thin films on glass substrate seeded with oxide nanosheets. *ACS Nano* **8**, 6145–6150 (2014).

71. Chen, K. *et al.* Direct growth of single-crystalline III-V semiconductors on amorphous substrates. *Nat. Commun.* **7**, 1–6 (2016).

72. Mohanty, D. *et al.* Growth of epitaxial CdTe thin films on amorphous substrates using single crystal graphene buffer. *Carbon N. Y.* **144**, 519–524 (2019).

73. Chang, J. Spin Coating Epitaxial Films. *Cailiao Daobao/Materials Reports* **33**, 1919–1920 (2019).

74. Zhao, T. *et al.* Realization of a Highly Oriented $MAPbBr_3$ Perovskite Thin Film via Ion Exchange for Ultrahigh Color Purity Green Light Emission. *ACS Energy Lett.* **3**, 1662–1669 (2018).

75. Chiang, C. H. & Wu, C. G. A Method for the Preparation of Highly Oriented $MAPbI_3$ Crystallites for High-Efficiency Perovskite Solar Cells to Achieve an 86 % Fill Factor. *ACS Nano* (2018).

76. Meng, X. *et al.* Surface-Controlled Oriented Growth of FASnI3 Crystals for Efficient Lead-free Perovskite Solar Cells. *Joule* **4**, 902–912 (2020).

77. Green, M. A., Ho-Baillie, A. & Snaith, H. J. The emergence of perovskite solar cells. *Nat. Photonics* **8**, 506–514 (2014).

78. Yin, W. J., Shi, T. & Yan, Y. Structural, electronic, and optical properties of lead halide perovskites. *RSC Energy Environ. Ser.* **2016-Janua**, 177–201 (2016).

79. Hutter, E. M. *et al.* Direct-indirect character of the bandgap in methylammonium lead iodide perovskite. *Nat. Mater.* **16**, 115–120 (2017).

80. Sum, T. C. & Mathews, N. Advancements in Perovskite Solar Cells: Photophysics behind the Photovoltaics. *Energy Environ. Sci.* 2518–2534 (2014).

81. Xing, G. *et al.* Long-range balanced electron- and hole-transport lengths in organic-inorganic $CH_3NH_3PbI_3$. *Science* **342**, 344–347 (2013).

82. Miyata, A. *et al.* Direct measurement of the exciton binding energy and effective masses for charge carriers in organic–inorganic tri-halide perovskites. *Nat. Phys.* **11**, 582–587 (2015).

83. Giorgi, G., Fujisawa, J. I., Segawa, H. & Yamashita, K. Small photocarrier effective masses featuring ambipolar transport in methylammonium lead iodide perovskite: A density functional analysis. *J. Phys. Chem. Lett.* **4**, 4213–4216 (2013).

84. Gerischer, H., Michel-Beyerle, M. E., Rebentrost, F. & Tributsch, H. Sensitization of charge injection into semiconductors with large band gap. *Electrochim. Acta* **13**, 1509–1515 (1968).

85. O'Regan, B. & Gratzel, M. A Low-Cost, High-Efficiency Solar-Cell Based on Dye-Sensitized Colloidal TiO_2 Films. *Nature* **353**, 737–740 (1991).

86. Kojima, A., Teshima, K.,, Shirai, Y., and Miyasaka, T. Organometal Halide Perovskites as Visible- Light Sensitizers for Photovoltaic Cells. *J Am Chem Soc* **131**, 6050–6051 (2009).

87. Kim, H.-S. *et al.* Lead Iodide Perovskite Sensitized All-Solid-State Submicron Thin Film Mesoscopic Solar Cell with Efficiency Exceeding 9 %. *Sci. Rep.* **2**, 591 (2012).

88. Lee, M.; Teuscher, J.; Miyasaka, T.; Murakami, T.; Snaith, H. Efficient Hybrid Solar Cells Based on Meso-Superstructured Organometal Halide Perovskites. *Science* **338**, 643–648 (2012).

89. Liu, D. & Kelly, T. L. Perovskite solar cells with a planar heterojunction structure prepared using room-temperature solution processing techniques. *Nat. Photonics* **8**, 133–138 (2013).

90. Ke, W. *et al.* Low-temperature solution-processed tin oxide as an alternative electron transporting layer for efficient perovskite solar cells. *J. Am. Chem. Soc.* **137**, 6730–6733 (2015).

91. Anaraki, E. H. *et al.* Highly efficient and stable planar perovskite solar cells by solution-processed tin oxide. *Energy Environ. Sci.* **9**, 3128–3134 (2016).

92. National Renewable Energy Laboratory. NREL Photovoltaic Research. *Web* Efficiency Chart (2016).

93. Brittman, S., Adhyaksa, G. W. P. & Garnett, E. C. The expanding world of hybrid perovskites: materials properties and emerging applications. *MRS Commun.* **5**, 7–26 (2015).

94. Zhou, J. & Huang, J. Photodetectors Based on Organic–Inorganic Hybrid Lead Halide Perovskites. *Adv. Sci.* **5**, (2018).

95. Hu, X. *et al.* High-performance flexible broadband photodetector based on organolead halide perovskite. *Adv. Funct. Mater.* **24**, 7373–7380 (2014).

96. Dou, L. *et al.* Solution-processed hybrid perovskite photodetectors with high detectivity. *Nat. Commun.* **5**, 5404 (2014).

97. Li, F. *et al.* Ambipolar solution-processed hybrid perovskite phototransistors. *Nat. Commun.* **6**, 8238 (2015).

98. Dong, R. *et al.* High-Gain and Low-Driving-Voltage Photodetectors Based on Organolead Triiodide Perovskites. *Adv. Mater.* **27**, 1912–1918 (2015).

99. Tan, Z. *et al.* Two-Dimensional $(C_4H_9NH_3)_2PbBr_4$ Perovskite Crystals for High-Performance Photodetector. *J. Am. Chem. Soc.* **138**, 16612–16615 (2016).

100. Gong, M. *et al.* High-Performance All-Inorganic $CsPbCl_3$ Perovskite Nanocrystal Photodetectors with Superior Stability. *ACS Nano* **13**, 1772–1783 (2019).

101. Ramasamy, P. *et al.* All-inorganic cesium lead halide perovskite nanocrystals for photodetector applications. *Chem. Commun.* **52**, 2067–2070 (2016).

102. Tan, Z. K. *et al.* Bright light-emitting diodes based on organometal halide

perovskite. *Nat. Nanotechnol.* **9**, 687–692 (2014).

103. Chin, X. Y., Cortecchia, D., Yin, J., Bruno, A. & Soci, C. Lead iodide perovskite light-emitting field-effect transistor. *Nat. Commun.* **6**, 1–9 (2015).

104. John, R. A. *et al.* Ionotronic halide perovskite drift-diffusive synapses for low-power neuromorphic computation. *Adv. Mater.* **30**, 1–8 (2018).

105. Peng, W. *et al.* Solution-Grown Monocrystalline Hybrid Perovskite Films for Hole-Transporter-Free Solar Cells. *Adv. Mater.* **28**, 3383–3390 (2016).

106. Rao, H. S., Chen, B. X., Wang, X. D., Kuang, D. Bin & Su, C. Y. A micron-scale laminar $MAPbBr_3$ single crystal for an efficient and stable perovskite solar cell. *Chem. Commun.* **53**, 5163–5166 (2017).

107. Chen, Z. *et al.* Single-Crystal $MAPbI_3$ Perovskite Solar Cells Exceeding 21 % Power Conversion Efficiency. *ACS Energy Lett.* **4**, 1258–1259 (2019).

108. Chen, M., Shan, X., Geske, T., Li, J. & Yu, Z. Manipulating Ion Migration for Highly Stable Light-Emitting Diodes with Single-Crystalline Organometal Halide Perovskite Microplatelets. *ACS Nano* **11**, 6312–6318 (2017).

109. Lian, Z. *et al.* High-Performance Planar-Type Photodetector on (100) Facet of $MAPbI_3$ Single Crystal. *Sci. Rep.* **5**, 16563 (2015).

110. Saidaminov, M. I. *et al.* Planar-integrated single-crystalline perovskite photodetectors. *Nat Commun* **6**, 8724 (2015).

111. Liu, Y. *et al.* 20-mm-Large Single-Crystalline Formamidinium-Perovskite Wafer for Mass Production of Integrated Photodetectors. 1829–1837 (2016).

112. Liu, Y. *et al.* Thinness- and Shape-Controlled Growth for Ultrathin Single-Crystalline Perovskite Wafers for Mass Production of Superior Photoelectronic Devices. *Adv. Mater.* **28**, 9204–9209 (2016).

113. Saidaminov, M. I. *et al.* Perovskite Photodetectors Operating in Both Narrowband and Broadband Regimes. *Adv. Mater.* 8144–8149 (2016).

114. Fang, Y., Dong, Q., Shao, Y., Yuan, Y. & Huang, J. Highly narrowband

perovskite single-crystal photodetectors enabled by surface-charge recombination. *Nat. Photonics* **9**, 679–686 (2015).

115. Gu, Z., Huang, Z., Li, C., Li, M. & Song, Y. A general printing approach for scalable growth of perovskite single-crystal films. 1–9 (2018).

116. Wei, W. *et al.* Monolithic integration of hybrid perovskite single crystals with heterogenous substrate for highly sensitive X-ray imaging. *Nat. Photonics* **11**, 315–321 (2017).

117. Pan, W. *et al.* a Low Detection Limit. *Nat. Photonics* **11**, 1–8 (2017).

118. He, Y. *et al.* High spectral resolution of gamma-rays at room temperature by perovskite $CsPbBr_3$ single crystals. *Nat. Commun.* **9**, 1–8 (2018).

119. Yun, J. S. *et al.* Benefit of grain boundaries in organic-inorganic halide planar perovskite solar cells. *J. Phys. Chem. Lett.* **6**, 875–880 (2015).

120. Yun, J. S. *et al.* Critical Role of Grain Boundaries for Ion Migration in Formamidinium and Methylammonium Lead Halide Perovskite Solar Cells. *Adv. Energy Mater.* **6**, 1–8 (2016).

121. Khassaf, H., Yadavalli, S. K., Zhou, Y., Padture, N. P. & Kingon, A. I. Effect of Grain Boundaries on Charge Transport in Methylammonium Lead Iodide Perovskite Thin Films. *J. Phys. Chem. C* **123**, 5321–5325 (2019).

122. Long, R., Liu, J. & Prezhdo, O. V. Unravelling the Effects of Grain Boundary and Chemical Doping on Electron-Hole Recombination in $CH_3NH_3PbI_3$ Perovskite by Time-Domain Atomistic Simulation. *J. Am. Chem. Soc.* **138**, 3884–3890 (2016).

123. Muscarella, L. A. *et al.* Crystal Orientation and Grain Size: Do They Determine Optoelectronic Properties of $MAPbI_3$ Perovskite? *J. Phys. Chem. Lett.* **10**, 6010–6018 (2019).

124. Wang, Q. *et al.* Scaling behavior of moisture-induced grain degradation in polycrystalline hybrid perovskite thin films. *Energy Environ. Sci.* **10**, 516–522

(2017).

125. Yang, R. *et al.* Inhomogeneous degradation in metal halide perovskites. *Appl. Phys. Lett.* **111**, (2017).

126. Chu, Z. *et al.* Impact of grain boundaries on efficiency and stability of organic-inorganic trihalide perovskites. *Nat. Commun.* **8**, 1–8 (2017).

Chapter 3

Experimental Methodology

The chapter describes the rationale behind choosing the methods and characterizations discussed in the thesis. This chapter elucidates the concept of different material characterization techniques used in the work, their advantages, and limitations in studying the particular characteristic. The chapter also explains the fabrication and testing protocols adopted for the optoelectronic devices discussed in the upcoming chapters.

3.1 Rationale for Method Selection

The stellar efficiencies as well as device performances reported for perovskite based solar cells and other optoelectronic devices are fueled by optimizations in material processing and device fabrication. Optimizations in material processing can be broadly classified into three: (a) optimization of precursors, (b) optimization in spin coating and anti-solvent dripping procedures (c) optimization in annealing and post annealing procedures. All these approaches modify the crystallinity and morphology of perovskite films thus affecting the device performances.

It has been found that perovskite precursors form co-ordination complexes with solvents[1]. Hence the selection and optimization of the used solvents is of utmost importance. The work reported here is also instigated by the investigation of precursor complexes. The processes of crystallization of bulk perovskite crystals and crystallization of thin films are entirely different. While the former process bank on the formation of few homogeneous nuclei and growth into large bulk crystals, the latter one relies on numerous heterogeneous nucleation sites on the substrate surface and its growth into a pinole free thin film. Crystallization techniques were systematically developed to grow highly crystalline and oriented films of lead halide perovskites in this work. The substrate surfaces also play a vital role on the substrate induced heterogeneous nucleation and crystallization. *X*-ray diffraction based characterization techniques were used to examine the material crystallinity and orientation of these films. Optical microscopy and scanning electron microscopy (SEM) imaging were used to identify the microstructure as well as grain sizes of the films. The crystallization processes were optimized so as to deposit pin hole free films over substrates for optoelectronic device fabrication. The materials were optically and electrically characterized before fabricating devices.

Optoelectronic devices like photodetectors and photovoltaic devices were fabricated and characterized (a detailed explanation of fabrication procedures is provided in the following sections) The crystallinity and orientation of the films play an important role in the device characteristics. The device characteristics of crystal based devices are compared with the characteristics of normal thin film based devices. As the crystallinity affects the ambient stability of the material and the consistency of the fabricated

optoelectronic devices, stability studies were also performed[2]. Lead halide perovskites are ionic materials and ionic migration is a common phenomenon observed in these materials. The role of grain boundaries in ionic migration through the materials were also investigated by galvanostatic and impedance measurements.

3.2 *X*-ray Diffraction Based Techniques for Crystallinity and Orientation Investigations

X-rays are electromagnetic radiations with their wavelengths of the order of inter-atomic lattice spacing of crystals. When X-rays irradiate materials, the crystal lattices act as scattering centers and in material systems with long range order the scattered X-rays constructively interfere to form diffraction patterns[3]. Since the diffraction angle depends on the inter-lattice spacings, the diffraction patterns act as unique attributes for materials. The lattice spacing of atomic planes in a material, d can be calculated from its diffraction pattern by using Bragg's law as

$$\lambda = 2d \ sin\,\theta$$

where λ is the wavelength of *X*-rays used, 2θ (in degrees) is the angle between diffracted and transmitted *X*-ray beams as shown the figure below.

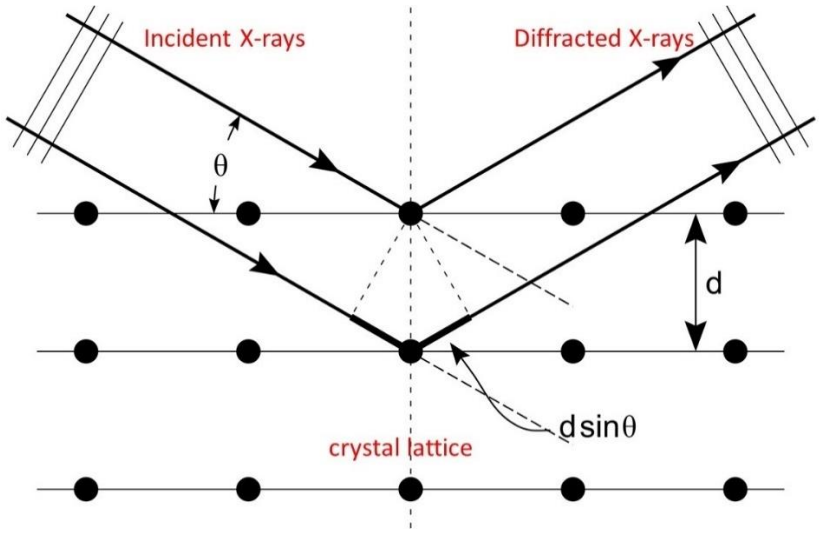

Figure 3.1: *X*-ray diffraction from crystal lattice and Braggs law.

X-ray diffractometry is a powerful technique that can be used to identify the crystallinity, crystal symmetry, crystal orientation and strains in the crystal structures of materials. Crystallinity and strain in the crystal lattice can be identified from diffraction peak broadening. Williamson-Hall analysis can be carried out to identify the lattice strain[4]. The crystallinity or mean size of crystalline domains (τ) in a polycrystalline thin film can be identified by using Scherrer equation as

$$\tau = \frac{K\lambda}{\beta \cos\theta}$$

where K is a dimensionless shape factor (K = 0.9), β is the full width half maximum (FWHM) of the diffraction peak under analysis in radians (β = FWHM of peak measured – instrument broadening) and θ is the Bragg diffraction angle in degrees. However, this analysis is applicable only for nano-sized crystallites (typically less than 0.1 μm).

In this work, XRD patterns were obtained on Bruker D8 Advance and Panalytical XPert Pro diffractometers with a Cu target. K_α of X-Rays produced were of wavelength 1.5418 Å at 40 kV and 40 mA. The step size used for measuring the crystallinity was 0.02^o with a step duration of 1.5 seconds. For measuring the ambient stability, a quicker scan was used with 0.03^o step size and 1 second step duration. For measuring the full width half maximum, the samples were scanned with a much smaller step size of 0.005^o with a step duration of 1 second.

3.2.1 *X*-ray Pole Figure Analysis

Pole figures are graphical representations used to express the orientation of objects in space. Pole figures can be used to represent crystallographic textures (alignment of crystallographic planes in a particular direction from a reference plane) of materials and films. The stereographic projections of normal to crystallographic planes of a crystal are used to form its characteristic pole figures. In crystallography, a pole figure is a representation of the crystal plane normal plotted with respect to a sample frame of reference. The sample frame is a sphere with an equatorial plane passing through the sample surface. Angle of *X*-ray incidence and diffraction detection are set for specific

crystallographic planes. The sample is tilted and rotated to cover the entire hemisphere over the sample.

The diffracted intensities from crystal planes hit distinct areas on the scanning hemisphere. Unit vectors from all the crystal planes intersecting the sphere are projected through the equatorial plane to the opposite 'north pole' of the sphere. The intersections of these unit vectors with the equatorial reference plane are plotted to create the characteristic pole figure. The measurements were carried out using a Bruker D8 Discover diffractometer using a Cu target, scanned at a step size of 5° for χ and Φ.

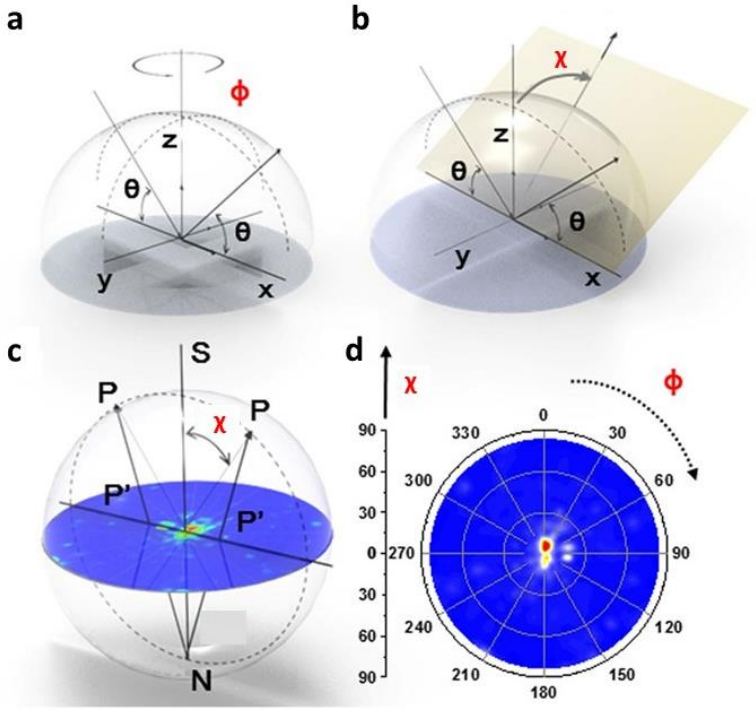

Figure 3.2: The (a) rotation and (b) tilt angles of the sample with respect to the reference sphere, (c) Projection of poles to the opposite pole of the sphere, (d) The formed pole figure on the equatorial plane[5].

3.3 Morphology and Microstructure Investigations

Morphology and microstructures are investigated by using imaging techniques such as optical microscopy and scanning electron microscopy (SEM). The resolution capacity of the techniques determines the smallest feature that can be observed.

3.3.1 Optical Microscopy

The most straightforward microscopy technique where the sample to be observed is illuminated with light of the visible electromagnetic spectrum (400 nm to 700 nm). The setup consists of an objective lens, an eyepiece (ocular) lens, lens tube, sample stage and beam splitter. The magnified morphology can be observed by naked eye or can be photographed using CCD / CMOS camera.

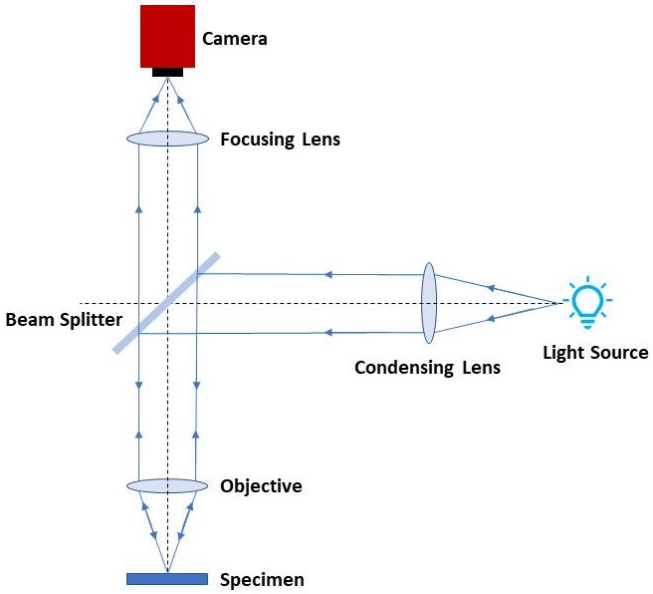

Figure 3.3: Principle of operation of optical microscope with a camera.

The smallest distance between two points that can be resolved using a normal optical microscope is given by Abbe's criterion as[6]

$$d = \frac{\lambda}{2n\ sin\,\alpha}$$

where *n* is the refractive index of the medium between the specimen and the objective lens, α is the light collection angle of the objective, λ is the wavelength used to illuminate the sample. For an optical microscope, the resolution is limited by the wavelength used for illumination.

Therefore, for imaging smaller features optical microscopy fails and microscopy techniques like scanning electron microscopy are employed.

In this work, optical microscopy images are obtained by Leica DMLS microscope coupled with a CS505CU – Kiralux colour CMOS camera from Thorlabs by employing Thorcam software.

3.3.2 Scanning Electron Microscopy (SEM)

In SEM, the sample to be observed is raster scanned with a focused electron beam of energy ranging from 1 to 20 keV[7]. The scanning is done on a rectangular area where the imaging has to be carried out and the wavelength associated with the electron beam depends on the applied accelerating voltage.

While their interaction with the specimen, the electrons get elastically and inelastically scattered producing a variety of signals. The incident electrons penetrate a few microns into the sample bulk and produces back scattered electrons, secondary electrons and X-rays, which are detected and processed. The back scattered electrons are elastically scattered from the sample and it depends on atomic mass. Thus, they are used to identify various composites of the sample. Secondary electrons are inelastically scattered and have lower energies (< 5 eV). Hence, they are used to identify topographical information[8].

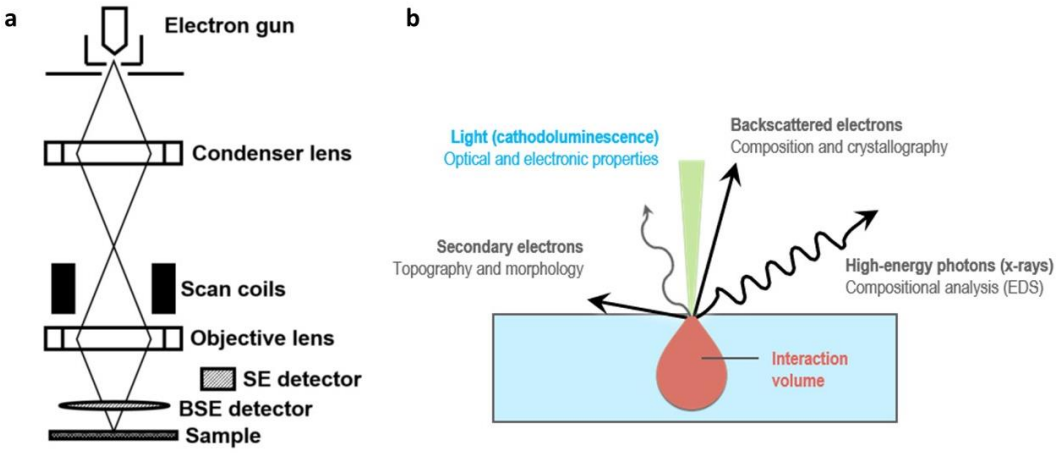

Figure 3.4: (a) Schematic diagram of basic parts of SEM, (b) Interaction of electron beam with the specimen and the produced signals[9].

As the high energy electron beam hits the sample, it removes the inner shell electrons from the atoms of the sample. This leads to the production of *X*-rays which are unique for the element from which it is emitted. These *X*-rays are employed to identify the atomic compositional information of the specimen using a technique known as energy dispersive *X*-ray spectroscopy. As electrons are used to image the samples, insulating specimen lead to surface charge accumulation. Thus, the samples should be either conducting or should be coated with thin layer of metals like Au or Pt (by sputtering) before imaging.

In this work, SEM was extensively used to identify the microstructures and morphology of crystalline films. Cross-sectional SEM imaging was used to study the crystal and device layer thicknesses. Electron microscopy in this work is carried out by using a field emission scanning electron microscope JEOL JSM-7600F. The samples to be imaged are platinum sputtered to reduce the charging effects during the imaging process. The accelerating voltage was kept at 5 kV for all the measurements.

3.4 Electron Backscatter Diffraction (EBSD)

EBSD is a technique used to determine grain morphology and crystalline orientation. The characterization technique employs the same equipment as an SEM, but the information gathering technique is different, which uses specific horizontally placed scintillator detectors and a CCD/CMOS camera. Similar to an SEM, EBSD utilizes an electron beam to raster scan the sample surface. The technique utilizes high energy backscattered (elastically scattered) electrons from the sample to generate the orientation information. In order to collect the backscattered electron efficiently, the sample is tilted at an angle of 70^{o} to the horizontal (as shown in Figure 3.5). When electron beams hit the sample, they get Bragg diffracted from the crystal planes. The diffracted electron beams from the sample undergo constructive interference to form a pattern of intersecting bands on the scintillator plate, representing the diffracting planes at the specific location. These bands are known as Kikuchi bands and they give information about the structure of the lattice. The symmetry of the pattern, its width and intensity are related to the symmetry of the crystal lattice and spacing of the atoms in the crystallographic plane. The angle between Kikuchi bands is equal to the angle

between crystallographic planes. Kikuchi patterns are obtained for all points on the scanning area to create a crystal orientation map. To interpret the orientation from the Kikuchi pattern, its Hough transform is carried out to convert the bands to distinct points which can represent specific crystallographic planes.

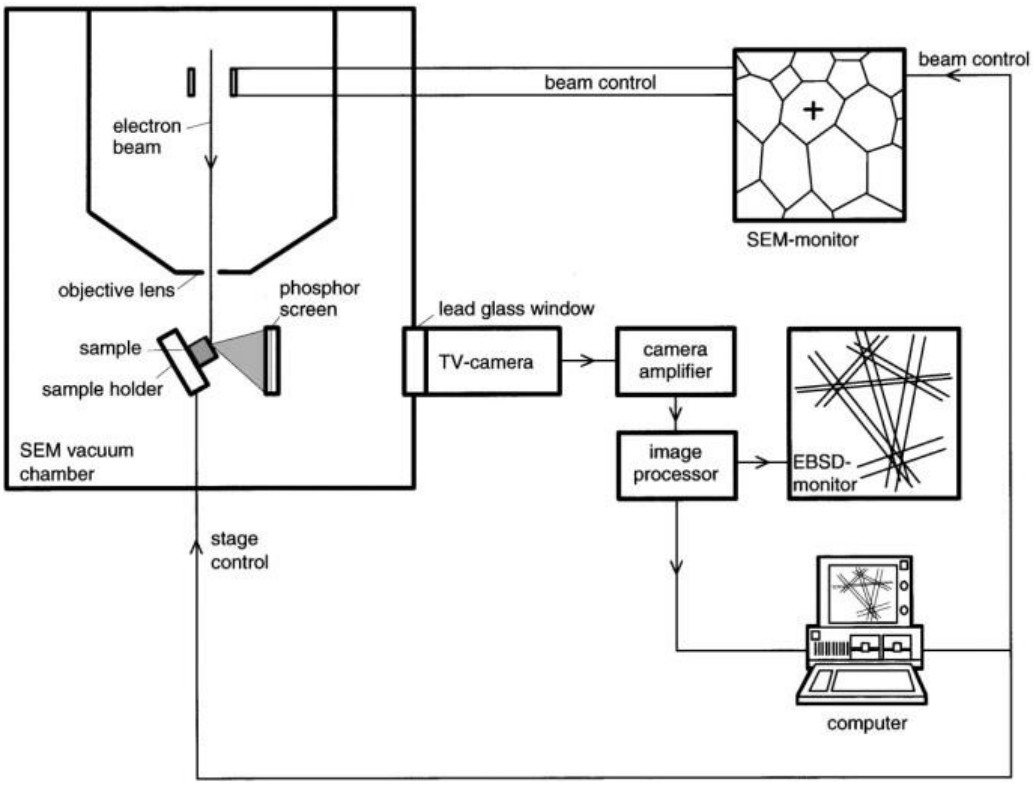

Figure 3.5: Schematic diagram of EBSD setup attached to a SEM[10]

The orientation information obtained from Kikuchi patterns are then mapped on the topographic image to get a simultaneous information on grain morphology and its crystal orientation. The Kikuchi pattern information can be utilized to create pole figures of crystal planes and to generate a schematic representation of the orientation.

The EBSD sensor (Symmetry from Oxford Instruments) is attached to 7800F PRIME scanning electron microscope with an accelerating voltage of 15 kV and a probe current of 1 nA.

3.5 Steady State Optical Spectroscopic Techniques

Semiconductors are materials with discrete electronic energy band levels separated by a forbidden band gap. The transition of electrons between valance and conduction bands are coupled with emission and absorption of electromagnetic waves. The wavelength of these emissions and absorptions ranges from near infrared to ultraviolet regimes. Hence the absorption and emission spectra of these materials in these wavelengths give information about its electronic band structure. If the samples are illuminated by continuous light sources and the spectral information is collected as functions of wavelength then the measurements are considered as steady state spectroscopic measurements.

3.5.1 Steady State Absorption Spectroscopy

This spectroscopic technique is based on absorption of electromagnetic radiation, where the samples are illuminated by a continuous monochromatic source. The wavelength of the monochromatic source is continuously varied to plot the attenuation spectrum, as it passes through the sample. The mathematical relation between absorption, concentration and path length of light through the sample is given by Bouguer-Lambert-Beer law as[11]

$$log\left(\frac{I_0}{I}\right)_\lambda = log\left(\frac{100}{T(\%)}\right)_\lambda \equiv A_\lambda = \varepsilon_\lambda cd$$

Where $log\left(\frac{I_0}{I}\right)_\lambda = A_\lambda$ is the absorbance, $\frac{I}{I_0} * 100 = T_\lambda$ (in %) is the transmittance, I_0 is the incident monochromatic light intensity, I is the transmitted beam intensity, ε_λ is the molar extinction coefficient, c is the molar concentration of the sample and d is the path length of the sample. If the concentration of the sample is high ($>10^{-2}$mol L^{-1}), ε_λ becomes independent of the sample concentration and the equation is no longer valid. For thin film samples the absorption coefficient can be calculated from its reflectance and transmittance spectra as,

$$\alpha_{film}(\lambda) = \frac{1}{d_{film}}\left(\frac{1 - R_{film}(\lambda)}{T_{film}(\lambda)}\right)$$

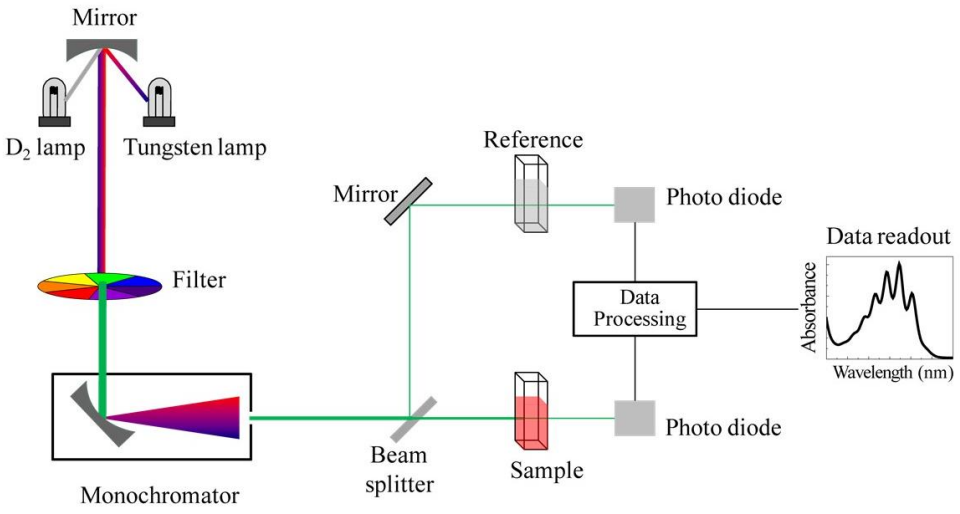

Figure 3.6: Schematic working principle of UV-Visible-NIR spectrophotometer.

Where d_{film} is the thickness of the sample, $R_{film}(\lambda)$ and $T_{film}(\lambda)$ are its reflectance and transmittance respectively. Band gap of semiconductors can be calculated from Tauc plot using the measured absorption coefficient. In Tauc plot hυ (on x-axis) is plotted with $(\alpha h\upsilon)^{\frac{1}{p}}$ (on y-axis). The exponent p shows the nature of transitions between valence band and conduction band of semiconductors. $p = \frac{1}{2}$ for direct and $p = 2$ for indirect transitions[12].

Urbach energy is deduced as the width of the tail of localized defect states in the optical bandgap of materials[13]. Urbach energy can be calculated from the absorption coefficient (α).

$$\alpha = \alpha_0 \, exp(\frac{h\upsilon}{E_{urb}})$$

$$ln(\alpha) = ln(\alpha_0) + \frac{h\upsilon}{E_{urb}}$$

Where α_0 is a constant, hυ is the energy of incident photons and E_{urb} is the Urbach energy. Urbach energy is calculated from the slope of $ln(\alpha) - h\upsilon$ plot.

In this work steady state absorption spectroscopy is used to measure the optical band gap of the samples produced. A UV-Visible spectrophotometer – SHIMADZU UV-3600 was used to record the absorption spectrum. An integrating sphere ISR-3100 was

used in all the measurements. For solutions a quartz cuvette was used as the sample holder.

3.5.2 Steady State Photoluminescence (PL) Spectroscopy

In this spectroscopic technique, the samples are excited by light beams with specific wavelengths. The excitation wavelength is selected in such a way that it falls under the absorption regime of the material and can create a band to band electronic transition. The intensity of light emitted from the material is detected using a photodetector and plotted with respect to the wavelength of emission. The steady state photoluminescence measurements give information about the types of radiative recombination in the material. The intensity of photoluminescence reveals the magnitude of radiative recombination while the wavelength of the PL maximum shows the electronic states responsible for this recombination.

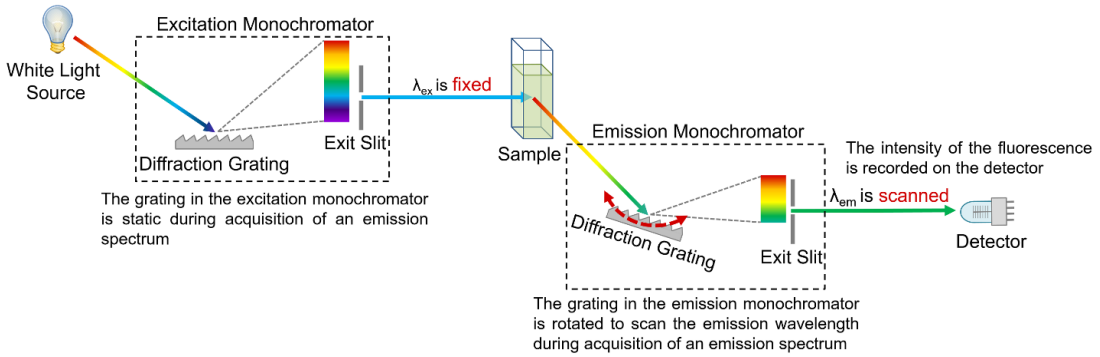

Figure 3.7: Schematic showing the working of a steady state PL spectro-fluorometer[14].

In this work, PL spectroscopy was used to study the electronic band structures of the materials. All the steady state photoluminescence measurements were carried out using HORIBA Scientific Fluoromax-4 Spectro-fluorometer.

3.6 Space Charge Limited Current (SCLC) Based Trap Density Measurements

Space charge limited current method can be used to measure the trap density of inorganic, organic and polymer semiconductors. For SCLC measurements, the

semiconductor is sandwiched between two metal electrodes. At least one of the metal-semiconductor contacts should be non-blocking and ohmic. The voltage across the semiconductor is varied and current through the semiconductor is recorded. At lower voltages, the current through the semiconductor is limited by the resistance of the semiconductor and gives rise to ohmic conduction. As the voltage is increased and when trapping centers are present, the traps capture the injected charge carriers and contributes to the trapping-liberating mediated conduction. This area of trap filling region can be used to calculate the density of traps in the material. When the applied voltage is higher than the average energy associated with trap density the conduction through the semiconductor acts as trap free space charge limited current[15–17].

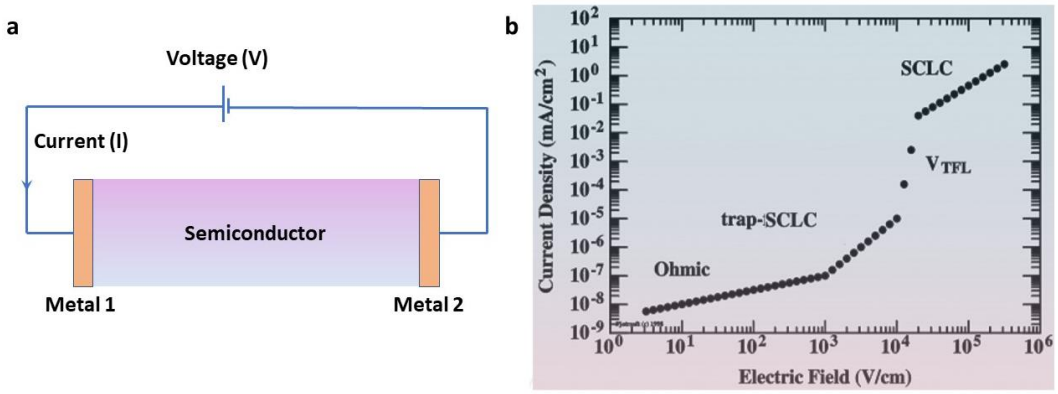

Figure 3.8: (a) The measurement set up for SCLC based trap density measurements, (b) A typical current-voltage curve through a semiconductor with charge traps[18].

A probe station and Keithley-4200 Semiconductor Characterization System was used to record the Voltage (V) - Current (I) curve. A $log_{10}V$ - $log_{10}I$ curve was plotted to identify the trap filling voltage (V_{TFL}), characterized by a sudden increase in the current passing through the semiconductor. The trap densities were calculated using the expression,

$$N_{traps} = \frac{2\varepsilon V_{TFL}}{qL^2}$$

Where ε is the dielectric constant of the material, L is the distance between electrodes and q is the electronic charge.

Pre-patterned interdigitated FTO electrodes deposited over glass substrate were used to conduct the SCLC measurements. After cleaning the substrates, thin films were spin coated over the substrates by the commonly used one-step deposition process, at 5000 rpm for 12 seconds along with anti-solvent dripping. The films were annealed at 90^{o}C for 5 minutes. The same substrates were used to grow crystals over them. The cleaned substrates were dipped in perovskite precursor solution and crystals were grown by the ultrasound mediated growth technique (to be discussed in Chapter 4). SCLC measurement was carried out over this substrate integrated crystals to measure the trap density.

3.7 Surface Energy Measurements of Substrates by OWRK model

Surface energy of substrates plays a vital role in crystallization as it can act as a center of heterogeneous nucleation. Energy of surfaces are usually identified by its wetting angles and the surfaces with high energies have low wetting angles. The wetting (hydrophilicity / hydrophobicity) arises from interaction between molecules of solvents with the surface atoms. There are several models to calculate the surface energies. Owens, Wendt, Rabel and Kaeble popularly known as OWRK method is commonly used for surface energy measurements with polar solvents[19–22].

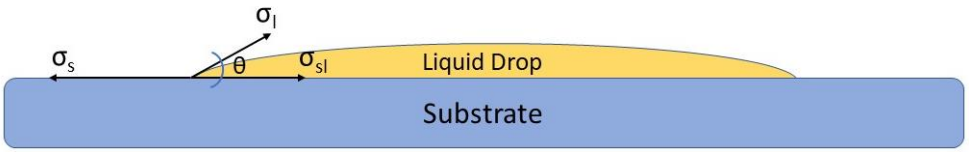

Figure 3.9: Equilibrium forces acting on a liquid dropped on a solid surface.

Consider a liquid droplet in equilibrium on any solid surface as shown above. The liquid drop is kept at equilibrium by the surface energy of the substrate (σ_s), surface energy of the liquid (σ_l) and the interface energy between the substrate and the liquid (σ_{sl}). As per the equilibrium force equation

$$\sigma_s = \sigma_{sl} + \sigma_l cos\theta$$

where θ is the contact angle made by the liquid on the substrate and this equation is called Young's equation. As per the OWRK model the surface tension can be split into two components – tension due to dispersive interactions of the solid and the liquid (σ_s^d, σ_l^d) and tension due to polar interactions of the solid and liquid (σ_s^p, σ_l^p). I.e.

$$\sigma_s = \sigma_s^d + \sigma_s^p$$

$$\sigma_l = \sigma_l^d + \sigma_l^p$$

By OWRK model, interfacial energy can be calculated from the contribution of the liquid and solid by:

$$\sigma_{sl} = \sigma_s + \sigma_l - 2\left(\sqrt{\sigma_s^d . \sigma_l^d} + \sqrt{\sigma_s^p . \sigma_l^p}\right)$$

Substituting the above in the Young's equation forms a linear equation in two variables as the form $y = ax + b$ with

$$y = \frac{1 + cos\theta}{2} \frac{\sigma_l}{\sqrt{\sigma_l^d}} \ , x = \sqrt{\frac{\sigma_l^p}{\sigma_l^d}} \ , a = \sqrt{\sigma_s^p} \ and \ b = \sqrt{\sigma_s^d}$$

Since the resulting equation is linear with two variables *x* and *y*, it is required to use at least two liquids of different surface energies to measure the surface energy of the solid. Solving the Young's equation σ_s can be calculated.

Here three liquids were used viz, deionized water, dimethylformamide and dimethyl-sulfoxide to measure the surface energy of the solid. The surface energy of substrates modified with self-assembled monolayers (the procedure of surface modification is explained in the following sections) are measured and the results are compared to the surface energy of bare glass substrates. The measurement of surface energies is performed right after the surface treatment steps. The surface energy of the solid substrates was calculated using liquid contact angle measurements using SCA 20 software by using OWRK model.

3.8 Dynamic Light Scattering (DLS) Measurements of Precursors in Solvents

DLS measurements are used to determine the hydrodynamic size of dispersed particles in a solvent by measuring its Brownian motion. Brownian motion is the random movement of particles which results from their collision with solvent molecules. Smaller particles diffuse more quickly, and larger particles diffuse slowly in the solvent medium. The rate of Brownian motion is quantified by the translational diffusion co-efficient represented by D. Hydrodynamic size measured by DLS is defined as the size of a sphere that diffuses at the same rate as the particle being measured. This sphere comprises of a core particle and its associated surface bound entities like ions.

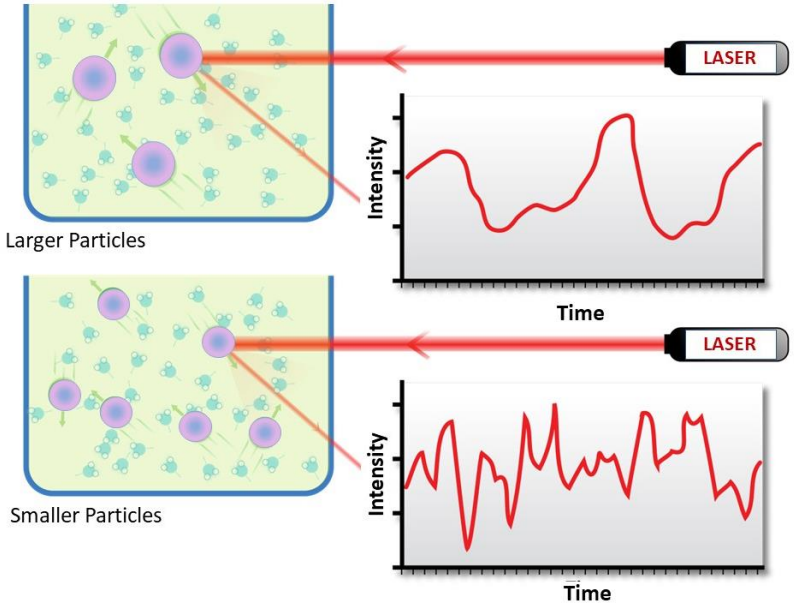

Figure 3.10: The principle of operation of DLS measurements to measure the dispersed particle size distribution.

DLS measures the diffusion rates to calculate the hydrodynamic size. If the particles are illuminated with a laser, they scatter the incident light in all directions because of its random motion in the solvent[23]. The scattered intensity is measured using a detector and due to the Brownian motion, the scattered intensity varies over time. The detected light scattered from large number of particles combines to create a fluctuating intensity signal function. The fluctuating function is created by interference of light scattered

from each individual particle. The intensities change over time as the particles diffuse continuously. The speed of intensity fluctuation is dependent on the particle diffusion rate. Smaller particles can diffuse quickly and can create a rapidly fluctuating scattered intensity function and vice versa[24].

The fluctuating intensity signal at the detector is autocorrelated with different time delays. The smaller highly mobile particles cause the auto-correlation function to drop quickly while larger particles delay the drop of the autocorrelation function. The translational diffusion coefficient (*D*) is calculated from the autocorrelation function. The hydrodynamic diameter of the particles is calculated from *D* by Stokes-Einstein equation as

$$d_H = \frac{kT}{3\pi\eta D}$$

where d_H is the hydrodynamic diameter, k is the Boltzmann's constant and η is the viscosity of the used solvent.

Using DLS size distribution of dispersed particles (ranging from a few nanometers to tens of micrometers) can be calculated. In this work the precursors of different concentration were filled in quartz cuvette and measured using Zetasizer Nano ZS.

3.9 Galvanostatic Measurements for Ionic and Electronic Conductance

Galvanostatic measurements can be used to measure ionic and electronic conductance of mixed ionic electronic conductors (MIEC)[25]. Lead halide perovskites are known ionic and electronic conductors. The measurement is carried out by depositing ion blocking electrodes on the material and applying a constant current in between.

Applying a constant current across the electrode leads to polarization of the material and the formation of a potential gradient. Applying the boundary conditions (as shown in Figure 3.10) initially at $t = 0$, the conductance has electronic (σ_e) and ionic (σ_i) components. i.e.

$$\sigma_{tot} = \sigma_e + \sigma_i$$

As t increases (as $K \rightarrow \infty$), the total conductance becomes purely electronic as the whole ionic current get saturated. i.e.

$$\sigma_{tot} = \sigma_e$$

When the current through the material is switched off, the potential across the material drops to V_d

$$V_d = V_s \frac{\sigma_i}{\sigma_{tot}}$$

These results can be utilized to calculate the ionic and electronic conductivity of the material. The materials were deposited on pre-patterned interdigitated FTO or ITO ion blocking electrodes for the galvanostatic measurements. The measurements are carried out by using a Keithley 4200 SCS with the aid of a probe station.

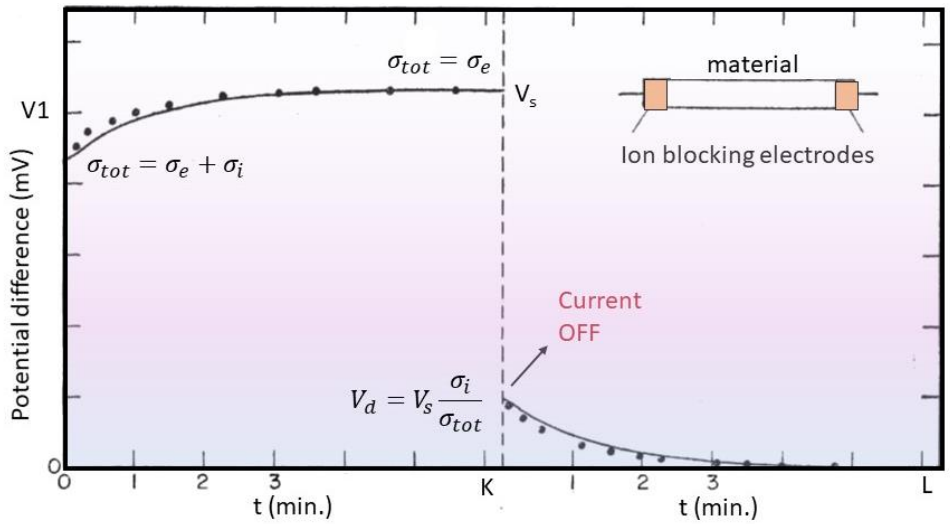

Figure 3.11: Galvanostatic measurements of a typical mixed ionic electronic conductor and the corresponding boundary conditions.

3.10 Impedance Spectroscopy for Ion Migration Investigation

The ionic and electronic conductance can be decoupled in mixed ionic electronic conductors by applying an AC bias across the material and measuring the impedance offered[26]. The equivalent circuit of a polycrystalline MIEC can be explained as given below.

The electronic and ionic drifts are associated to the resistances: R_e, the resistance offered for the electronic current through the material; R_i, the resistance offered for the ionic current. The ionic transport through polycrystalline materials are impeded by brain boundaries contributed by R_{gb} and C_{gb} in series with the ionic resistance. If the

electrodes are ion blocking the ions get accumulated at the material-electrode interfaces and contribute to an interface ionic capacitance, C_i. In addition, a capacitance called geometrical capacitance, C_{geom}, acts in parallel to all these components due to the dielectric constant of the material. The generic impedance curve for such a circuit is given in Figure 3.11b.

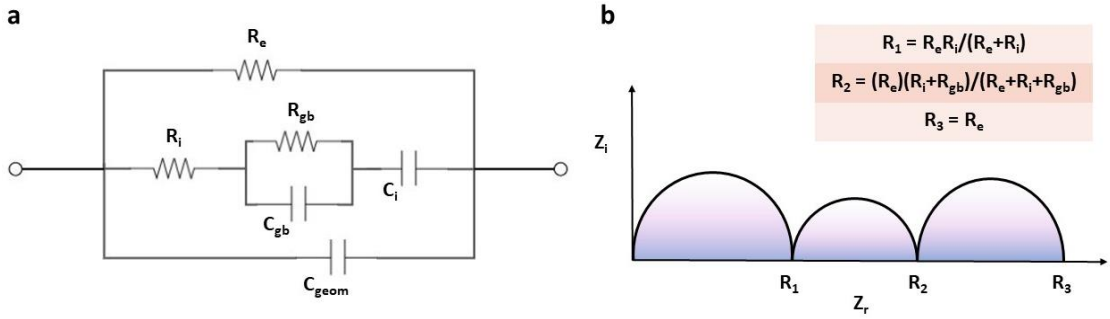

Figure 3.12: (a) The equivalent circuit of a polycrystalline MIEC sandwiched between hole blocking electrodes, (b) The generic impedance curve of the equivalent circuit.

Ionic conductance can be identified from the values of intercepts of the curve on the real impedance axis. The intercept at the lowest frequency, R_3 is equal to the shunt resistance R_e for electronic conductance. i.e.

$$R_3 = R_e$$

The intercept at the next higher frequency is a result of the combination of R_e and the sum of R_i and R_{gb} in parallel. The intercept can be calculated as

$$\frac{1}{R_2} = \frac{1}{R_e} + \frac{1}{R_i + R_{gb}} \equiv R_2 = \frac{R_e(R_i + R_{gb})}{R_e + R_i + R_{gb}}$$

The intercept at the highest frequency R_1 is given by a parallel combination of R_e and R_i as R_{gb} get shunted out by the grain boundary capacitance C_{gb}. Therefore

$$\frac{1}{R_1} = \frac{1}{R_e} + \frac{1}{R_i} \equiv R_1 = \frac{R_e R_i}{R_e + R_i}$$

Total conductance, G_{tot} can be calculated as

$$G_{tot} = G_i + G_e = \frac{1}{R_i} + \frac{1}{R_e}$$

Where G_i and G_e are ionic and electronic conductance, respectively.

This technique is particularly useful for polycrystalline lead halide perovskites as it can decouple bulk ionic and grain boundary assisted ionic conductance. This makes it possible to analyze the role of grain boundaries on the ionic conductivity of the material. Impedance measurements were carried out in two electrode configuration by employing a Metrohm Autolab potentiostat–galvanostat.

3.11 Surface Modification of Substrates and Crystallization Dish

The glass substrates were cleaned with Decon solution, dilute HCl, water, DI water, acetone, ethanol and were dried under nitrogen blowing. The substrates were UV-ozone cleaned for 30 minutes prior to incubation. 10 µl of APTMS was dispersed in 10 ml of anhydrous ethanol and kept in a well cleaned glass incubation petri dish. The UV-ozone cleaned substrates were quickly transferred to the petri dish and kept undisturbed at room ambience for 20 minutes. After 20 minutes the substrates were taken out and were cleaned by anhydrous ethanol by placing it in the bath sonicator for 10 minutes. The substrates were later dried by nitrogen blowing.

The crystallization dishes were cleaned as per the same procedure described for the glass substrates. 4 µl of OTS was dispersed in 20 ml of anhydrous toluene and was poured into the crystallization dishes which were UV–ozone cleaned for 30 minutes. The crystallization dishes were closed and kept in room ambience undisturbed for 2 hours. After 2 hours the toluene containing OTS was poured out of the crystallization dish and cleaned thrice by rinsing with fresh toluene. The glass wares were dried under nitrogen blowing and kept in a drying oven (at 70 ^{o}C) for 2 hours.

All these chemicals were from Sigma Aldrich and were used without any further purification.

3.12 Anti-solvent Vapor Crystallization for $MAPbBr_3$ and $MAPbI_3$

In Anti-solvent Vapor Crystallization (AVC) process, as discussed in previous chapter, the anti-solvent vapor is allowed to slowly evaporate to the solvent precursor solution, which creates supersaturation and crystallization. The crystal growth system has to be

kept vibration free for better crystal growth to take place. Here, the process recipe was fine tuned for $MAPbBr_3$ and $MAPbI_3$ so as to grow large free standing crystals. For $MAPbBr_3$ crystals, 0.20 M $PbBr_2$ and 0.20 M MABr were dissolved in 10 ml Dimethylformamide (DMF) to form the precursor solution. For $MAPbI_3$, 0.20 M PbI_2 and 0.24 M MAI were dissolved in γ-Butyrolactone (GBL) to form the precursor (a detailed explanation on the selection of solvents is provided in Chapter 4). The precursor solutions were filtered using 0.2 µm PTFE filter and transferred to a 50 ml crystallization dish. The crystallization dish was sealed and a hole of approximate cross section of 0.5 mm was provided for the antisolvent to diffuse inside. The precursor solution and substrate containing crystallization dish is kept inside a 250 ml beaker with 50 ml Dichloromethane (DCM) inside. The outer 250 ml beaker is tightly sealed so that the DCM, upon evaporation percolates to the crystallization dish kept inside through the tiny hole provided. As the anti-solvent moves to the precursor solution it creates supersaturation inside and the bulk crystals (of several millimeters in dimension) start growing in 3 days.

3.13 Fabrication and Characterization of Photodetectors

The FTO substrates with interdigitated electrodes on glass substrates were patterned by laser etching. The channel length used was 100 µm with a width of 3.17 cm. The perovskite films were spin coated as per the procedure previously reported and the crystals were grown over this prepatterned substrate to create the photodetector. The photodetectors thus fabricated were bottom illuminated (from the glass side) with a wavelength of 445 nm and was placed at a vacuum of 10^{-3} bar during all the photodetector measurements. The device figure of merits like responsivity, detectivity, rise-time and fall-time were calculated (a detailed explanation is given in the following chapter). The incident light power on the device were varied from 3 µW to 10^4 µW and pulsed using a Thorlabs DC2200 LED driver and Solis-445C blue light LED source. The device characteristics were measured by using a Keithley 4200 SCS with the help of a probe station. The rise-time and fall-time were measured by using a Keysight B2912A Precision Source/Measure Unit, to achieve a better time resolution.

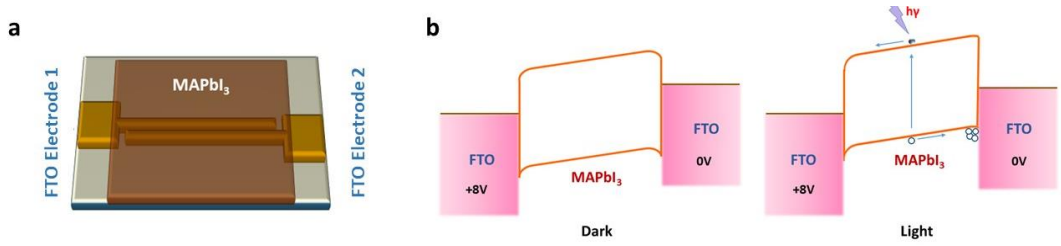

Figure 3.13: (a) The device configuration of the fabricated photoconductor, (b) Schematic energy band diagram of the device biased at 8V, assuming the material to be intrinsic

3.14 Fabrication and Characterization of Photovoltaic Cells

This work utilized planar device configurations with n-i-p structure for photovoltaic devices. Glass-ITO substrates were cleaned with decon soap, water, DI water, acetone, ethanol, and dried under nitrogen blowing. The substrates were UV-ozone cleaned for 30 minutes prior to SnO_2 deposition, which was used as ETL for the devices. SnO_2 quantum dots were synthesized in DI water from $SnCl_2.2H_2O$ and thiourea by a procedure reported in the literature[27]. The SnO_2 dispersed in DI water was spin coated over the cleaned substrates at a spin speed of 4000 rpm for 15 seconds. The deposited SnO_2 was annealed at 200 ^oC for 1 hour at room ambience. After the annealing process, the substrates are immediately transferred to argon gloveboxes. The substrates are UV-ozone cleaned prior to the deposition of perovskite layers. $MAPbI_3$ was used as the photo absorber throughout the work. Normal thin films of $MAPbI_3$ was deposited by spin coating at 5000 rpm as per the solvent engineering procedure reported before[28]. The $MAPbI_3$ crystals were grown on the substrate as per the procedure explained in the following chapter. The Spiro-OMeTAD layer was subsequently deposited by spincoating Spiro-OMeTAD solution (72 mg/mL in CBZ), used as the hole transporting layer. The solution had the following additives: 4-TBP (28.5 µL), LiTFSI (17.5 µL; taken from an ACN stock solution with a concentration of 520 mg/mL). The spiro layer was spin coated at a speed of 4000 rpm for 30 s. Gold (Au) electrode of thickness 100 nm was thermally evaporated under high vacuum (10^{-6} Torr) through a metal shadow mask of an active area of 0.2 cm^2.

Photovoltaic characterizations are carried out using AM 1.5G solar simulator (model 81172, Oriel) using a 450 W xenon lamp. A reference Si photodiode was used to calibrate the intensity of the solar simulator lamp to match AM 1.5G sunlight (100 mW/cm^2). A Keithley 2612A digital source meter was used to apply an external bias as well as to measure and record the I-V characteristics of the cells. The voltage scan is done at 100 mV/s from -0.1 to 1.2 V using exponential scan mode. The devices were measured by masking the active device area with a measurement mask of 0.09 cm^2. Incident-photon-to-current conversion efficiency (IPCE) is measured using a PVE300 (Bentham), with a dual xenon/quartz halogen light source, measured in DC mode, with no bias light.

3.15 References

1. Yan, K. *et al.* Hybrid Halide Perovskite Solar Cell Precursors: Colloidal Chemistry and Coordination Engineering behind Device Processing for High Efficiency. *J. Am. Chem. Soc.* **137**, 4460–4468 (2015).
2. Wang, Q. *et al.* Scaling behavior of moisture-induced grain degradation in polycrystalline hybrid perovskite thin films. *Energy Environ. Sci.* **10**, 516–522 (2017).
3. Cullity, B. D. *Elements Of X Ray Diffraction*. (Addison-Wesley Publishing Company, 1956).
4. Williamson, G. K. & Hall, W. H. Discussion of the Theories of Line Broadening. *Acta Metall.* **1**, 22 (1953).
5. Shi, F. *et al.* Strong texturing of lithium metal in batteries. *Proc. Natl. Acad. Sci. U. S. A.* **114**, 12138–12143 (2017).
6. Lipson, S. G., Lipson, H. & Tannhauser, D. S. *Optical Physics*. (Cambridge University Press, 1995).
7. McMullan, D. Scanning Electron Microscopy 1928–1965. *Scanning* **17**, 175–185 (1995).
8. Zhou, W. & Lin, Z. *Scanning Microscopy for Nanotechnology*.(2007).
9. Why Use Cathodo-Luminescence (2020) Available at https://whatiscl.info/overview/why-use-cathodoluminescence.

10. Randle, V. Texture. in *Encyclopedia of Materials: Science and Technology* (eds. Buschow, K. H. J. et al.) 9119–9129 (Elsevier, 2001)
11. Perkampus, H.-H. *UV-VIS Spectroscopy and Its Applications*. (Springer-Verlag, 1992).
12. Cesaria, M., Caricato, A. P. & Martino, M. Realistic absorption coefficient of ultrathin films. *J. Opt.* **14**, 105701 (2012).
13. Urbach, F. The long-wavelength edge of photographic sensitivity and of the electronic Absorption of Solids [8]. *Phys. Rev.* **92**, 1324 (1953).
14. What is a Spectrometer? (2020) Available at: https://www.edinst.com/blog/.
15. Lampert, M. A., Rose, A. & Smith, R. W. Space-charge-limited currents as a technique for the study of imperfections in pure crystals. *J. Phys. Chem. Solids* **8**, 464–466 (1959).
16. Moiz, S. A., Khan, I. A., Younis, W. A. & Karimov, K. S. Space Charge–Limited Current Model for Polymers. *Conduct. Polym.* (2016).
17. Bube, R. H. Trap Density Determination by Space-Charge-Limited Currents. *J. Appl. Phys.* **33**, 1733–1737 (1962).
18. Peter, S. *Electrical Characterization of Organic Electronic Materials and Devices*. (Wiley and Sons Ltd., 2009).
19. Owens, D. K. & Wendt. Estimation of the Surface Free Energy of Polymers. *J. Appl. Polym. Sci.* **13**, 1741–1747 (1969).
20. Rabel, W. Some aspects of wetting theory and their application to the investigation and modification of the surface properties of polymers. *Farbe und Lack* **77**, 997–1005 (1971).
21. Kaelble, D. H. Dispersion-Polar Surface Tension Properties of Organic Solids. *J. Adhes.* **2**, 66–81 (1970).
22. Marshall, S. J., Bayne, S. C., Baier, R., Tomsia, A. P. & Marshall, G. W. A review of adhesion science. *Dent. Mater.* **26**, 10–16 (2010).
23. Johnson, C. S. & Gabriel, D. A. Laser light scattering. *Spectrosc. Biochem.* **2**, 177–272 (2018).
24. Pecora, R. Doppler shifts in light scattering from pure liquids and polymer solutions. *J. Chem. Phys.* **40**, 1604–1614 (1964).

25. Yokota, I. On the Theory of Mixed Conduction with Special Reference to Conduction in Silver Sulfide Group Semiconductors. *J. Phys. Soc. Jpn.* **16**, 2213-2223 (1961)
26. Huggins, R. A. Simple method to determine electronic conductivity and ionic components of the conductors in mixed conductors a review. *Ionics (Kiel).* **8**, 300–313 (2002).
27. Yang, G. *et al.* Effective Carrier-Concentration Tuning of SnO2 Quantum Dot Electron-Selective Layers for High-Performance Planar Perovskite Solar Cells. *Adv. Mater.* **30**, 1–9 (2018).
28. Jeon, N. J. *et al.* Solvent engineering for high-performance inorganic–organic hybrid perovskite solar cells. *Nat. Mater.* **13**, 897–903 (2014).

Chapter 4

Perovskite Precursors and Crystallization by Sonication Modified Anti-solvent Vapor Crystallization (S-AVC).

Developing a crystallization technique from solution needs to be instigated by a meticulous study on the chemistry of precursors. In this chapter a brief discussion on the nature and colloidal chemistry of lead halide precursors in different solvents is provided. The chapter also explains the mechanism of anti-solvent vapor crystallization (AVC) for methylammonium based lead halide perovskites. Our systematic study on the mechanism of crystallization enabled us to modify the standard AVC technique to grow $MAPbBr_3$ and $MAPbI_3$ crystals over substrates. The crystallinity as well as optoelectronic quality of the grown film are also investigated and discussed.

Data and figures in this chapter are adapetd from: Riyas Ahmad, Abhijith Surendran, P. C. Harikesh, Reinhard Haselsberger, Nur Fadilah Jamaludin, Rohit Abraham John, Teck Ming Koh, Annalisa Bruno, Wei Lin Leong, Nripan Mathews, Maria-Elisabeth Michel-Beyerle, Subodh G. Mhaisalkar, Perturbation-Induced Seeding and Crystallization of Hybrid Perovskites over Surface-Modified Substrates for Optoelectronic Devices, *ACS Applied Materials and Interfaces*, 31, 27727–27734 (2019)

4.1 Introduction

Single crystals of bulk lead halide perovskites were easily grown by inverse temperature crystallization (ITC) and anti-solvent vapor crystallization (AVC) as discussed in Chapter 2[1–3]. Later on, $MAPbBr_3$ crystals of a few millimeters in lateral dimensions were grown on substrates by introducing microbubble implosion in AVC system[4]. ITC was modified to grow thin crystals of $MAPbI_3$, $MAPbBr_3$ and $MAPbCl_3$ in between two parallel substrates separated by a spacer[5,6]. Photovoltaic cells were fabricated using $MAPbI_3$ crystals grown between two parallel substrates, which yielded efficiencies above 21 %[7,8]. However, the lateral dimensions of these crystals were of the order of a few millimeters and were unable to scale up to larger dimensions. Increasing the lateral dimensions of these thin monocrystals or improving the crystallinity of the perovskite polycrystalline films deposited over substrates is required to completely utilize their exceptional optoelectronic material properties. It was found that the lifetime, diffusion length, and mobility of carriers approach the single crystalline regimes as the grain sizes reach around hundred micrometers[9]. Our motivation was to grow films of lead halide perovskites with monocrystal-like characteristics. The mechanism of crystal growth of perovskites by AVC was investigated and was modified to grow perovskite crystals on substrates. The precursors play a cardinal role in the crystallization and crystal growth of lead halide perovskites. It was found that solvents form coordination complexes with perovskite precursors, and the precursor-solvent complexes form colloidal dispersions[10]. Thus, a systematic optimization of the crystallization process should accompany a rigorous investigation of the nature of solvents used.

This chapter gives a glimpse about the work done on ultrasound mediated AVC crystal growth technique over device substrates. The anti-solvent vapor crystallization commonly used to grow bulk single crystals of perovskites was modified for $MAPbI_3$ and $MAPbBr_3$ to grow a well packed crystal film over a variety of substrates. The highly crystalline film grown by this method yielded impressive optoelectronic performances. The crystal films also showed better ambient stabilities when compared

to normal spin coated thin films. The chapter also discusses the work done on perovskite precursors and a brief examination of the solvent precursor interactions.

4.2 Perovskite Precursors: The Complex Colloidal Dispersion

Dimethyl sulfoxide (DMSO), dimethyl formamide (DMF), acetonitrile (ACN) and γ-butyrolactone (GBL) are the most commonly used solvents for perovskite thin film deposition and crystal growth. Guttmann's donor number is used as the parameter to indicate the coordination capacity of solvents with perovskite precursors[11].

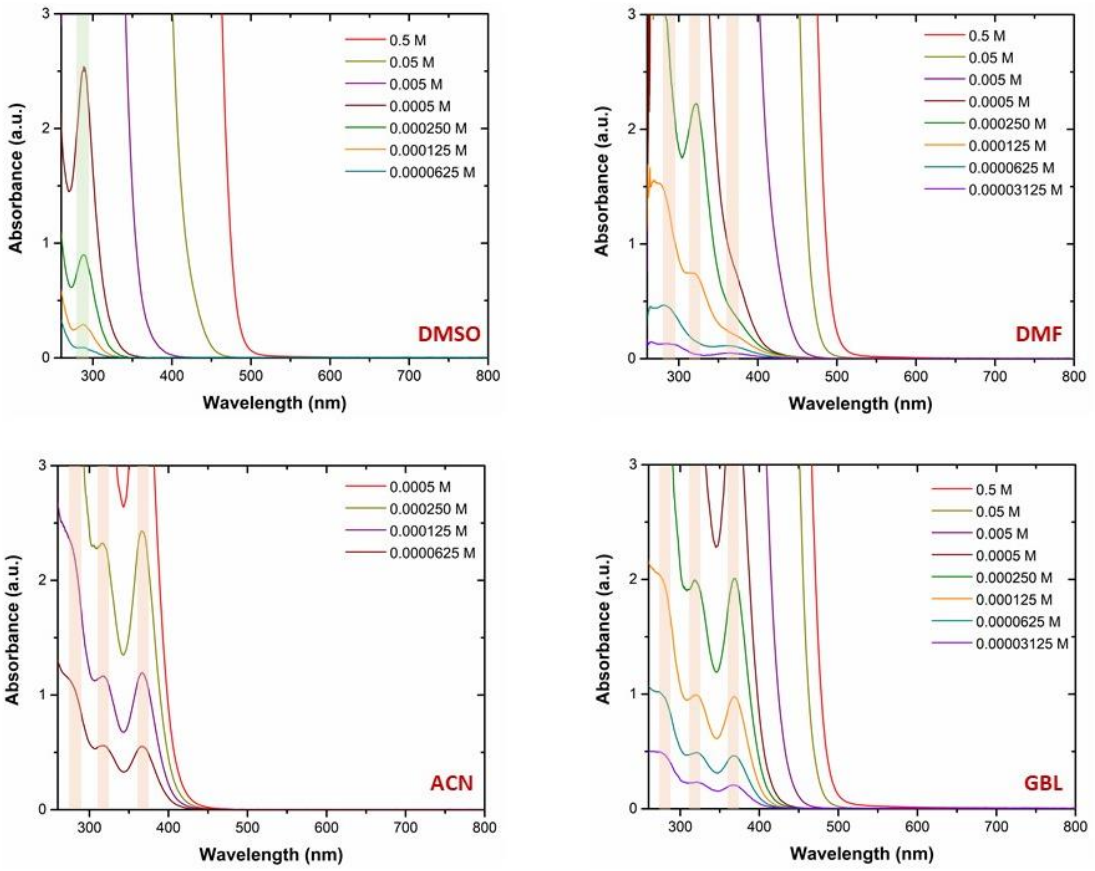

Figure 4.1: The UV-Vis absorption characteristics of perovskite precursors employing different solvents. The absorption peaks correspond to different complex coordination species.

As per the donor number, the coordination capability varies in the order DMSO > DMF > GBL > ACN. UV-visible absorption spectra of the precursors were carried out to analyze the chemical nature of precursors. The precursors (0.5 M for DMSO, DMF, GBL and 0.0005 M for ACN) are kept for overnight stirring before measuring their UV-visible absorption spectra. For the lower molar concentrations, the stock solution was diluted and used. The higher concentration (0.005 M and more) precursors are unable to show any absorption features owing to the high extent of light scattering and the limitations of Lambert-Beer's law at such high concentration levels (Figure 4.1). The absorption features at lower concentrations were similar for DMF, ACN and GBL. The absorption peaks correspond to different lead iodide coordination complexes (the solvents form a coordination complex of general formula $[PbI_mX_n]^{2-m}$ where X denote the solvent molecule)[12,13]. It is evident that in DMSO the precursor exists only in $[PbIX_n]^+$ form, whereas in GBL, ACN and DMF, they exist as a combination of multiple plumbate complexes (Table 4.1). Since DMSO has the highest Guttmann's donor number in the lot, it is expected to form the strongest coordination complex.

Table 4.1: The absorption peak and the corresponding coordination complexes formed in the precursors.

	A_{PbI^+} **(nm)**	A_{PbI_2} **(nm)**	$A_{PbI_3^-}$ **(nm)**
DMSO	290	----	----
DMF	280	320	360
ACN	275	315	365
GBL	275	320	365

A similar analysis was performed for $MAPbBr_3$ as well. $MAPbBr_3$ has poor solubility in ACN and GBL and hence the solvents were limited to DMF and DMSO. It was found that the precursor exists only in $[PbBrX_n]^+$ form for both DMF and DMSO (refer to appendix Figure A1).

4.3 Selection of Solvents for Anti-solvent Vapor Crystallization (AVC)

Though there are many works on the selection of solvents for the growth of bulk single crystals of lead halide perovskites by inverse temperature crystallization (ITC)[14,15], the crystallization mechanism and solvent selection for AVC were not commonly investigated.

Table 4.2: The nature of crystallization of perovskites with different solvent based precursors. Dichloromethane (DCM) was used as anti-solvent.

	$MAPbI_3$	**$MAPbBr_3$**
DMF	solvent composite crystallization	perovskite crystallization
DMSO	solvent composite crystallization	perovskite crystallization
GBL	perovskite crystallization	low solubility
ACN	low solubility	low solubility

Here, the crystallization process of perovskites by AVC was examined employing dichloromethane (DCM) as the common anti-solvent. DCM has a boiling point of 39.8 ^{o}C, which will get evaporated at room temperature and can slowly trickle down to the crystallization dish containing precursors. $MAPbI_3$ and $MAPbBr_3$ showed very low solubility in ACN and were not investigated. $MAPbBr_3$ showed low solubility in GBL as well and was not investigated.

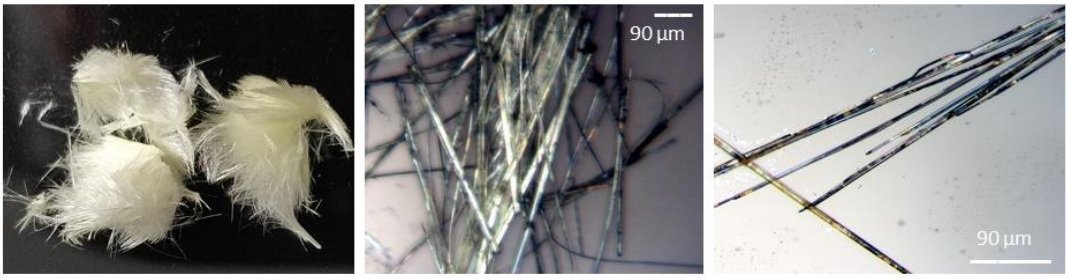

Figure 4.2: The crystallized solvent – precursor composite upon anti-solvent introduction to the MAPbI3 precursor in DMSO.

In DMF and DMSO, $MAPbBr_3$ precursors were highly soluble. Large bulk single crystals were crystallized out from both these solvents upon anti-solvent percolation. For $MAPbI_3$ precursors, DMF, DMSO and GBL provided significant solubilities. However, upon slow DCM introduction, only GBL was able to grow $MAPbI_3$ crystals. On DCM introduction, precursors based on DMF and DMSO crystallized out lead iodide – solvent composites at room temperature, instead of $MAPbI_3$. The solvent composite was dendritic in morphology as given in Figure 4.2. From the powder XRD data of the composite in Bragg-Brentano configuration, it was identified as $MA_2Pb_3I_8{\cdot}2DMSO$[16,17]. It was able to convert the precursor solvent composite to $MAPbI_3$ by treating it with methylammonium iodide (MAI) dissolved in isopropanol (Figure 4.3).

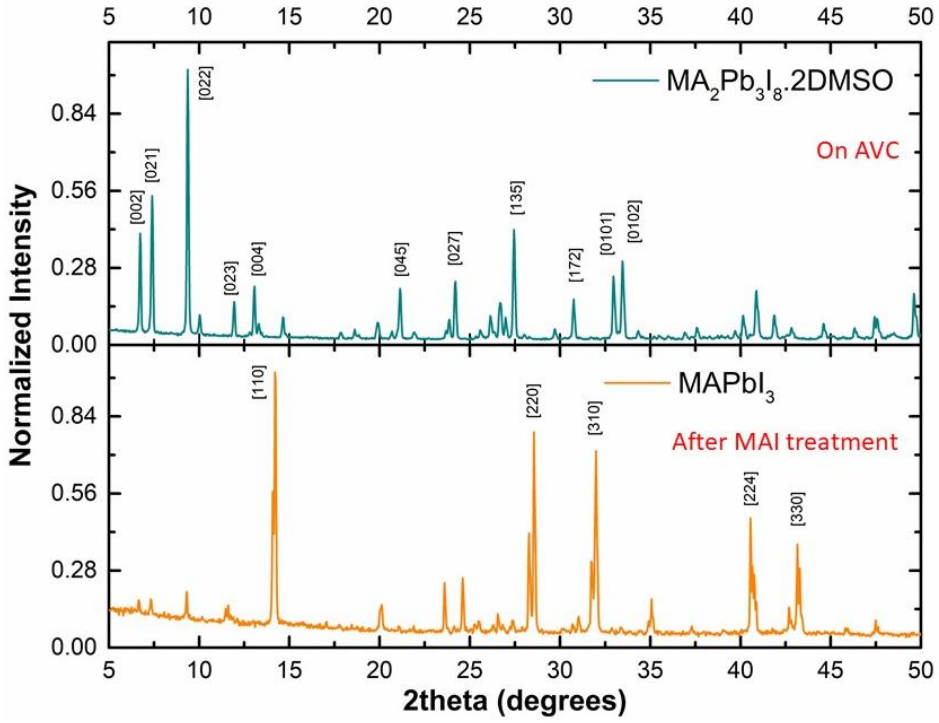

Figure 4.3: Powder XRD of the crystallized precursor-DMSO composite. The composite can be converted to $MAPbI_3$ by reacting it with MAI.

Concluding the observations, it can be inferred that low coordination solvents are required to crystallize out lead halide perovskites by AVC at room temperature. From

the nature of crystallization, GBL was selected for the growth of $MAPbI_3$ crystals, and DMF was chosen for crystallizing out $MAPbBr_3$. The mechanism of crystallization by anti-solvent percolation to the precursors was studied in the upcoming section for $MAPbI_3$ and $MAPbBr_3$ by employing these solvents.

4.4 Mechanism of $MAPbI_3$ and $MAPbBr_3$ Crystal Growth by Anti-solvent Vapor Crystallization (AVC).

The solvents were narrowed down to GBL and DMF for crystallizing $MAPbI_3$ and $MAPbBr_3$ respectively by AVC. The mechanism of crystallization by AVC needs to be unearthed, in order to modify and induce the crystal growth on device substrates.

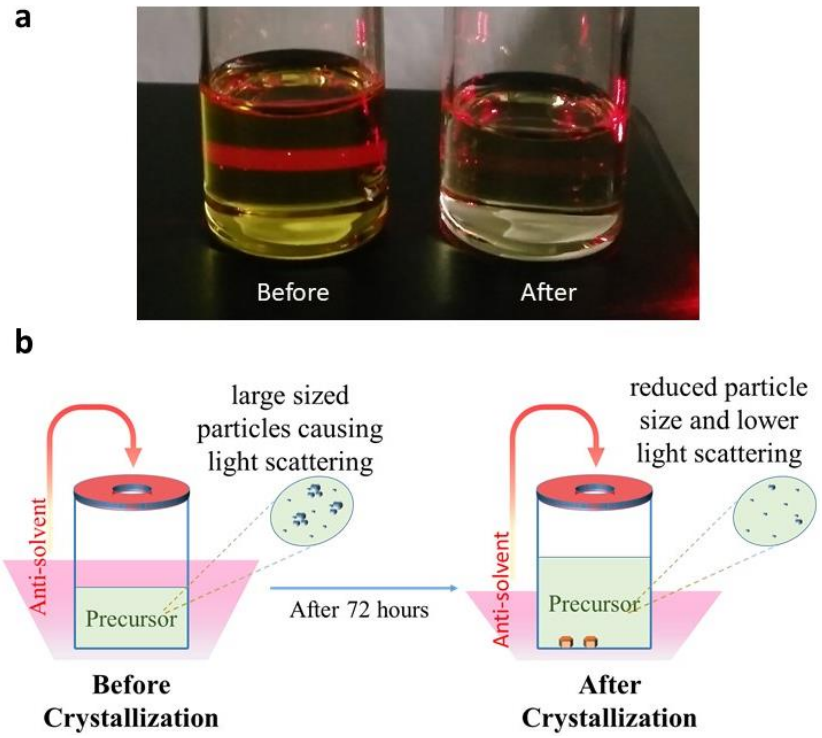

Figure 4.4: (a) The light scattered before and after crystallization from the precursor dispersion, (b) Schematic representation of the AVC crystallization process.

Light scattering was observed if a 650 nm laser beam was illuminated through the precursor solution. Both precursors showed significant light scattering as a result of

their colloidal nature, with the particle size of the order of hundreds of nanometers, revealed by dynamic light scattering (DLS) measurements (Appendix Figure A2). These results were well in accordance with the previous reports regarding the behavior of perovskite precursors. The solvent molecules formed coordination complexes with lead halides in the dispersion and resulted in the formation of large colloidal particles, which are stabilized by the presence of other organic ions in the system[10,18]. The anti-solvent vapor was allowed to slowly diffuse to these precursor dispersions to facilitate crystallization. In conventional anti-solvent crystallization methods (e.g., NaCl, Na_2CO_3 crystals), anti-solvent introduction drives out the dissolving solvents and thereby creates supersaturation and crystal growth in the precursor, which is associated with an increase in the colloidal particle size[19–21]. In contrast, perovskite precursors showed a reduced Tyndall effect after millimeter-sized crystals had grown out of them. This shows a reduction in the particle size of the precursors, and this reduction in the particle size is due to the consumption of precursors from the dispersion during crystallization (Figure 4.4). To get a deeper insight into the crystallization procedure, UV−Vis absorption spectroscopy was carried out for the precursor dispersion before, during, and after the anti-solvent introduction and crystallization (Appendix Figure A3). The spectrum before anti-solvent introduction showed sharp absorption edges at 490 and 400 nm for $MAPbI_3$ and $MAPbBr_3$, respectively. The absorption edges were blue-shifted upon antisolvent introduction. As anti-solvents were introduced and caused crystallization by consuming the precursors from the 'dispersion' bulk, it resulted in the dilution of the precursor. As the concentration decreased, the ratio of metal halide to ligand varied, causing the formation of smaller coordination complexes, which appeared as blue-shifted absorption edges. This was verified by observing the absorption edge of a 1000× diluted precursor using the same solvents (DMF and GBL for $MAPbBr_3$ and $MAPbI_3$, respectively). It was found that the absorption edge was further blue-shifted upon dilution. Surprisingly, the precursor dispersion during and after anti-solvent introduction did not show any $MAPbBr_3$ or $MAPbI_3$ perovskite crystal absorption peaks, not even after crystals of millimeter sizes were formed out of them. At the precursor concentrations used (0.2 M), it was observed that the perovskite crystals were always forming over the walls of the crystallization dish and the precursor

remained transparent throughout the crystallization procedure. To confirm that no colloidal perovskite nanocrystals were formed in the precursor, it was illuminated with UV at different stages of anti-solvent evaporation. The precursor did not show any photoluminescence at normal perovskite emission regimes. Summarizing all these results and observations, it was deduced that the crystallization happened exclusively on the surfaces of the crystallization dish (heterogeneous nucleation and growth) and not at the bulk of precursor dispersion. The energy to overcome the nucleation barrier is provided by the crystallization dish surface, and the crystals kept on growing over the surfaces by consuming the precursors surrounding the nuclei. As more precursors were consumed for the crystal growth, the coordination chemistry changed and the sizes of the particles in the colloid were reduced, which is evident from the reduced Tyndall effect (Figure 4.4a). The formation of large and stable coordination complexes in the precursor might be the reason for this distinct kind of crystallization for hybrid perovskites.

Figure 4.5: The wetting angles for DI water on various glass surfaces.

To confirm our hypothesis regarding the effect of surface energy of the crystallization dish on the crystallization process, AVC process with surface-modified crystallization dishes were carried out. Surfaces of the crystallization dishes were coated with self-assembled monolayers (SAM) of hydrophobic octadecyltrichlorosilane (OTS) and hydrophilic aminopropyltrimethoxysilane (APTMS) to respectively reduce and increase the surface energy[22–25](Figure 4.5). From OWRK model for estimation of surface energy, it was found that the surface energy of APTMS modified glass is three times higher than that of OTS modified glass surface (Table 4.3). The crystals grown

in dishes with increased surface energy had large facet area parallel to the walls of crystallization dishes, and crystals started to form over both horizontal and vertical walls of the dish.

Table 4.3: Surface energy calculated for the surface modified substrates by OWRK model.

	DI Water	**DMF**	**DMSO**	**OWRK surface energy (mN/m)**
Bare glass	31.8°	26.7°	26.9°	65
OTS glass	109.5°	54.9°	66.7°	23
APTMS glass	5.0°	3.9°	4.8°	80

However, in the case of reduced surface energy, no crystals were found over the vertical or horizontal walls of the dish. Instead, numerous tiny crystals started to crystallize out at the corners formed by the intersection of horizontal and vertical walls of the crystallizing dish, where the surface energy could be predominantly high (Figure 4.6). All these results vindicate our assumption that the surface energy of crystallization dishes provided the energy to overcome the nucleation barrier in AVC and the crystallization process takes place exclusively on the surfaces of crystallization dishes.

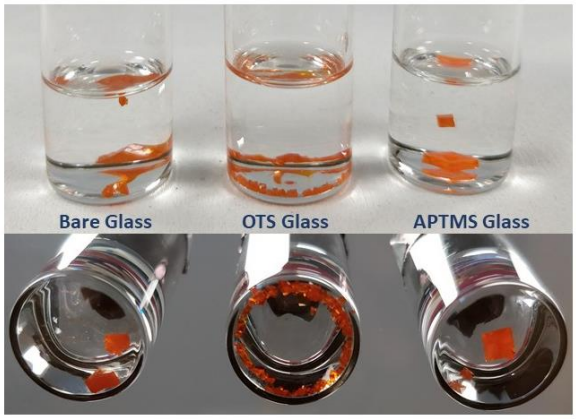

Figure 4.6: The nature of AVC crystal growth in surface energy modified crystallization dishes.

4.5 Sonication-Modified AVC (S-AVC) for Inducing Crystal Growth Over Substrates

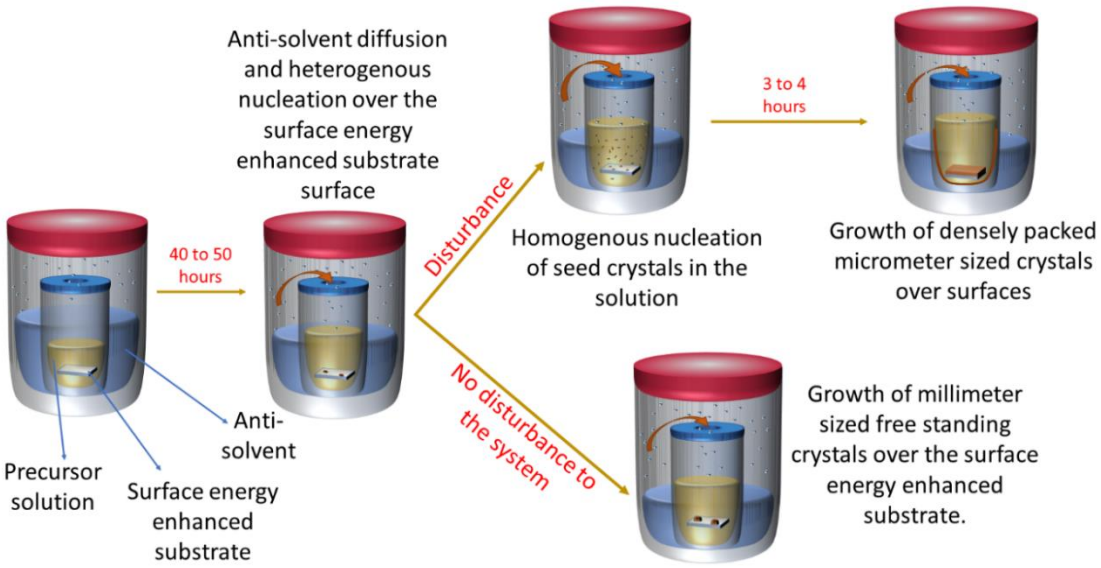

Figure 4.7: Schematic showing the crystallization procedure by sonication modified AVC (S-AVC).

Our investigation on the mechanism of AVC helped us to modify the process and to grow crystal films over substrates. In our sonication-modified crystal growth technique, the walls of the crystallization dish were coated with hydrophobic SAM (OTS) and the substrate over which crystals needed to be grown were coated with hydrophilic SAM (APTMS). A short duration (1 s) ultrasound was used to disturb the AVC system to create the growth of $MAPbBr_3$ as well as $MAPbI_3$ crystals over any substrate. The process was termed as sonication modified AVC (S-AVC). Upon perturbation of the supersaturated precursor, the color of the precursor dispersion turned slightly from colorless to orange in $MAPbBr_3$ (from yellow to gray in $MAPbI_3$), indicating that the nucleation and growth of seed crystals were initiated in the dispersion. This showed that the normal AVC, where heterogeneous nucleation prevailed, was altered upon perturbation and resulted in homogeneous nucleation and crystal growth in the precursor dispersion. As the seed crystals started to grow in the precursor dispersion,

they got attached to the walls of crystallization dish and the substrate kept inside it to attain stability, as explained by the schematic in Figure 4.7.

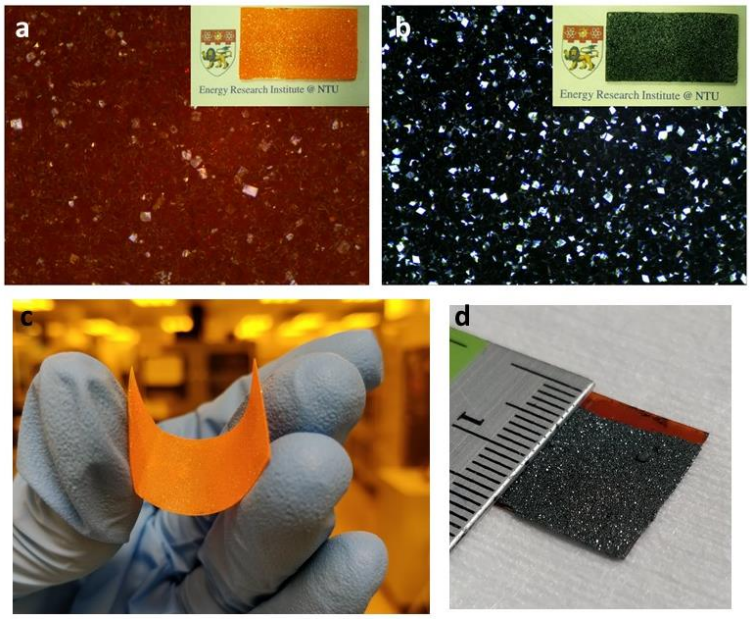

Figure 4.8: (a) and (c) $MAPbBr_3$ crystals grown on glass and flexible poly (ethylene terephthalate) substrates, (b) and (d) $MAPbI_3$ crystals grown on glass and Kapton substrates.

Further anti-solvent introduction to the precursor resulted in the growth of these seed crystals over the substrates. This led to the formation of densely packed, highly crystalline $MAPbBr_3$ and $MAPbI_3$ layers with an area of a few square centimeters over rigid as well as flexible substrates, as shown in Figure 4.8. S-AVC deposition can be used as a universal method to grow hybrid perovskite crystals over any substrates.

4.6 Crystallinity and Orientation Investigations of S-AVC grown perovskite film

The crystallinity and orientation of the crystal films were investigated using *X*-ray diffraction (XRD) (Figure 4.9), by employing a Bruker D8 Advance diffractometer in Bragg-Brentano configuration. As the crystal growth process spanned over a few hours in duration, the crystallinity of the films formed was found to be high.

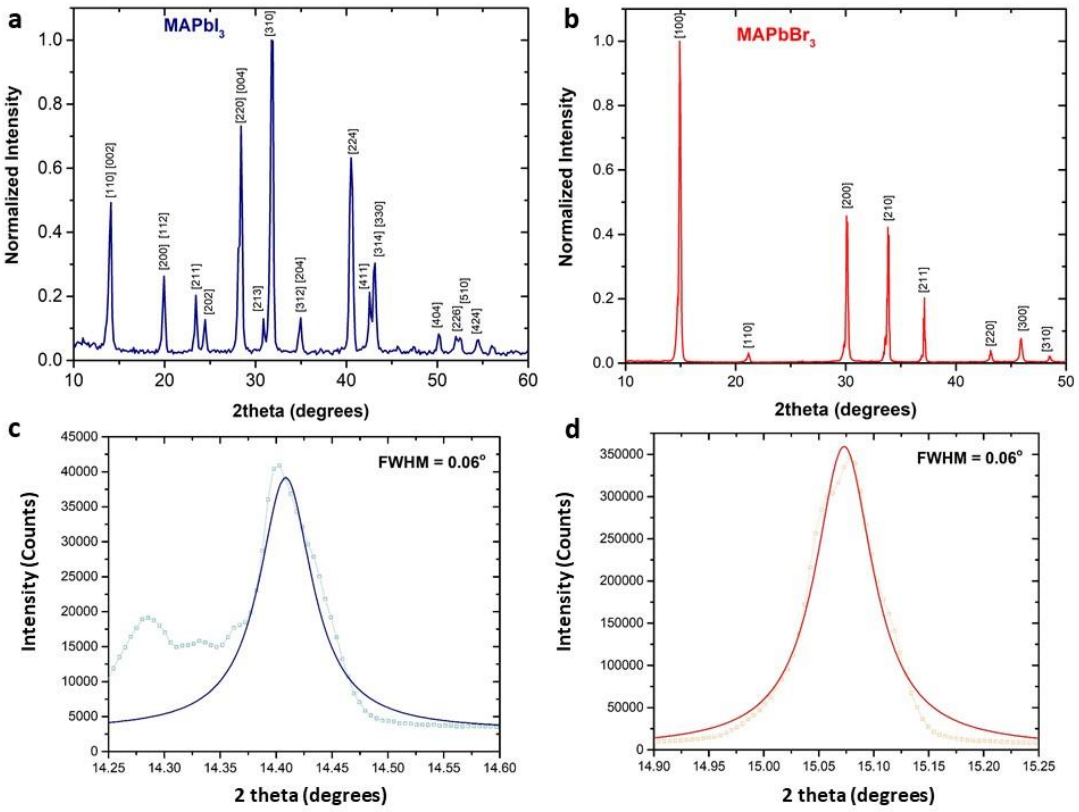

Figure 4.9: (a) and (b) XRD of $MAPbI_3$ and $MAPbBr_3$ crystal films, (c) and (d) full width half maxima of [110] plane of $MAPbI_3$ and [100] plane of $MAPbBr_3$, respectively.

$MAPbBr_3$ grown from the S-AVC method showed a slight preferential orientation along the [100] crystal plane, as given in Figure 4.9b. The full width at half maximum (FWHM) of the [100] peak was 0.06°, indicating good crystallinity of the material (Figure 4.9d). $MAPbI_3$ grown by S-AVC showed a preferred orientation marginally along [310]. The material showed good crystallinity as the measured FWHM of the [110] peak was 0.06° (Figure 4.9c). Optoelectronic devices employ a highly oriented layer of optoelectronic material for device fabrication. The S-AVC crystal films didn't show a high degree of crystalline orientation, sufficient for fabricating an efficacious monocrystalline device.

4.7 Morphology, Microstructure and Optical Characterizations

Scanning electron microscopy (SEM) was used as the major characterization tool for morphological investigations. The tightly packed pinhole-free $MAPbI_3$ film was composed of individual crystallites with an average dimension of 100 μm. The coverage, thickness and size of individual crystallite grain can be tuned by varying the crystal growth duration.

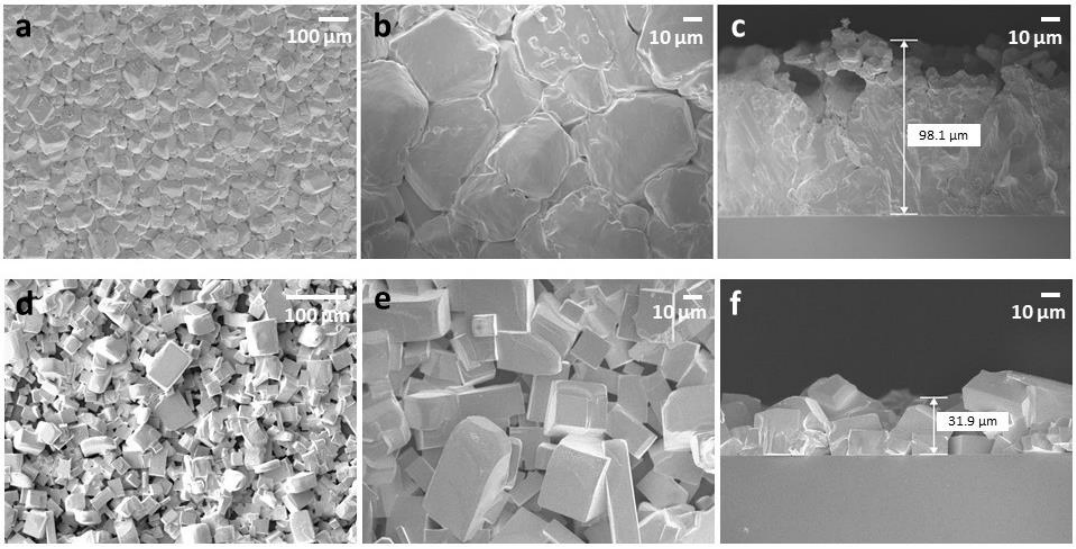

Figure 4.10: (a), (b), (c) $MAPbI_3$ crystal film grown over glass; (d), (e), (f) $MAPbBr_3$ crystals grown over glass by S-AVC method.

The typical thickness of the $MAPbI_3$ film was of the order of 100 μm after 3 h of growth and was pinhole free (Figure 4.10c). $MAPbBr_3$ films had a thickness around 50 μm after 3 hours of growth, which was required for a full coverage over substrates (Figure 4.10f). As the duration of crystal growth was increased, grain size as well as thickness were found to be increasing and after a particular interval new secondary nucleation takes place on existing crystals. This increases the number of crystal layers and it was found that such an increase in crystal thickness reduces the substrate adhesiveness. As the substrates were coated with $-NH_3$-terminated and hydrophilic (APTMS) SAM, it helped the crystals to attain a close packed growth over the substrates and gave a strong

adhesiveness between them. Since the nucleation and initial crystal growth took place in the precursor, the crystal growth was independent of substrate surfaces.

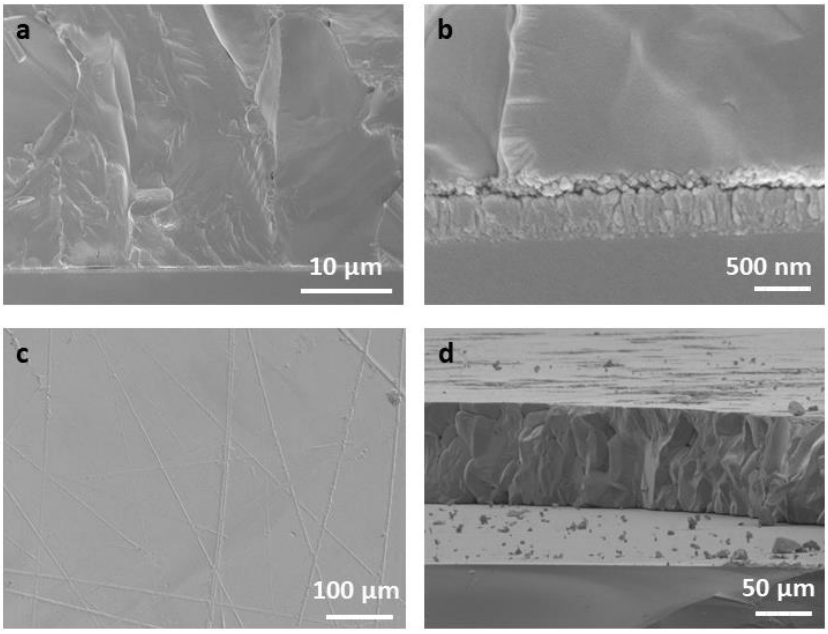

Figure 4.11: (a) and (b) $MAPbI_3$ crystals grown over FTO and mesoporous TiO_2 respectively, (c) and (d) $MAPbI_3$ crystals grown over glass and polished using optical sandpaper.

The surfaces of the grown film were found to be highly coarse since it was composed of numerous micrometer sized crystallites. The fabrication of optoelectronic devices atop was made impossible due to this coarse nature. The crystals were found to be growing over rough surfaces like FTO and meso-porous TiO_2 (Figure 4.11a, b). The crystal films were able to sustain high tensile forces, making it easy for processing and device fabrication (Appendix Figure A4). It was possible to mechanically polish the crystals grown over glass with optical sandpapers owing to their good substrate adhesiveness (Figures 4.11c, d). The $MAPbI_3$ films were black in color with UV-Visible spectrum absorption onset at 825 nm. The $MAPbBr_3$ films started absorbing the UV- Visible spectrum from 550 nm, (Appendix Figure A5) as the color being deep orange. The absorption onset for both these films were slightly redshifted (observed in single crystals of these materials) when compared to their thin films, probably because

of the high absorption cross section of the crystals when compared to their thin films. As the thickness of the films were of the order of hundred micrometers, the absorption spectra saturate right after the onset. The steady state photoluminescence spectra of both the bromide and iodide samples were also slightly redshifted from their thin film counterparts (Figure 4.12).

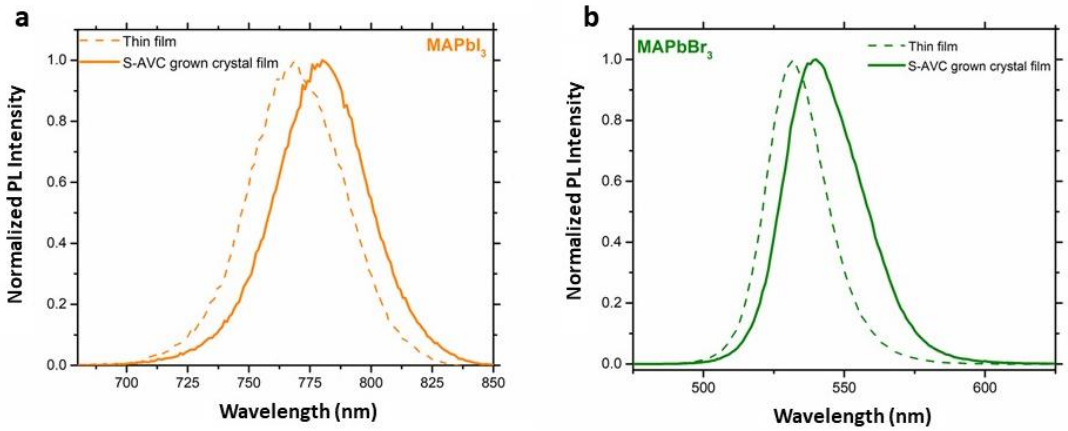

Figure 4.12: Steady state photoluminescence spectra of (a) $MAPbI_3$, (b) $MAPbBr_3$ crystals grown over glass and their comparison with normal spin coated polycrystalline films.

This redshift in photoluminescence of the crystals is attributed the process of predominant self-absorption of the photoluminescence. The photoluminescence peak of the material falls within its absorption regime and this reason is also responsible for the reduced PL intensities of highly crystalline films of hybrid perovskites, compared to their normal thin films[26,27]. These are typical characteristics of the single crystals of lead halide perovskites and from the above absorption as well as PL spectra, it was evident that the microcrystalline S-AVC film behaves more like single crystals when compared to their thin film counterparts.

4.8 Space Charge Limited Current (SCLC) Based Trap Density Measurements

To assess the quality of these crystal films, space charge limited current (SCLC) measurements were carried out, and their trap densities were calculated (Figure 4.13).

Crystals were grown over patterned fluorine-doped tin oxide (FTO) electrodes, which are relatively inert to lead halide perovskites, by the S-AVC method as described above. Due to the ionic nature of the material, a high interelectrode spacing of 100 μm was chosen to keep a minimal electric field. The current−voltage characteristics were measured across the electrodes. A $log_{10}V-log_{10}I$ curve was plotted to identify the trap filling voltage (V_{TFL}), characterized by a sudden increase in the current passing through the semiconductor.

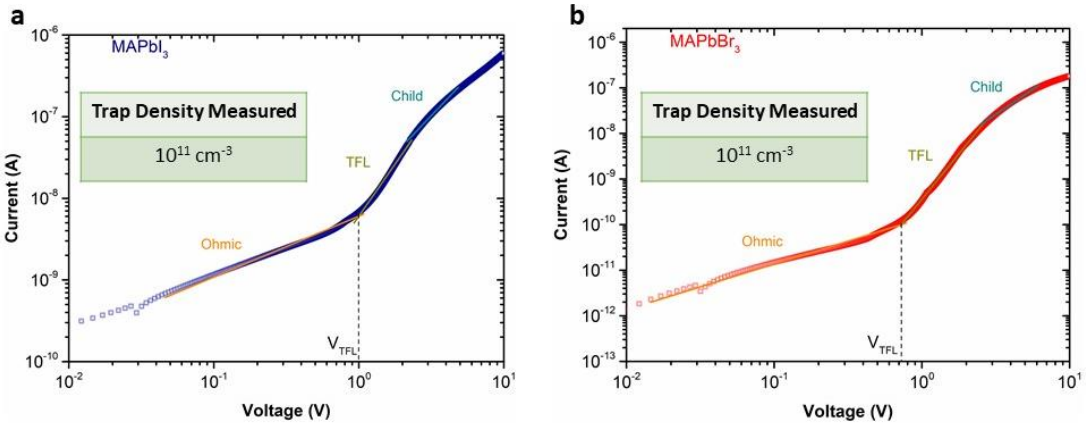

Figure 4.13: Trap densities measured electrically by SCLC method for (a) $MAPbI_3$ and (b) $MAPbBr_3$ crystals, grown over FTO electrodes.

The trap densities were calculated using the expression, $N_{traps} = \frac{2\varepsilon V_{TFL}}{qL^2}$, where ε is the dielectric constant of the material, L is the distance between the electrodes, and q is the electronic charge. The dielectric constants (ε_r) were taken as[28] 25.5 for $MAPbBr_3$ and 28.8 for $MAPbI_3$. The measured trap densities were very low, of the order of 10^{11} cm^{-3}, for both $MAPbBr_3$ and $MAPbI_3$. These values are comparable to the values reported previously for their single-crystal counterparts[3]. The results demonstrated that the crystals grown over substrates by S-AVC method are suitable for fabricating quality optoelectronic devices.

4.9 Ambient Stability Investigations of S-AVC Grown Films

Ambient stability issues have always hindered the commercialization of lead halide perovskite based optoelectronic devices, even though the devices showed stellar device characteristics. The single crystals of hybrid perovskites were always found to be more stable than their normal spin coated thin films.

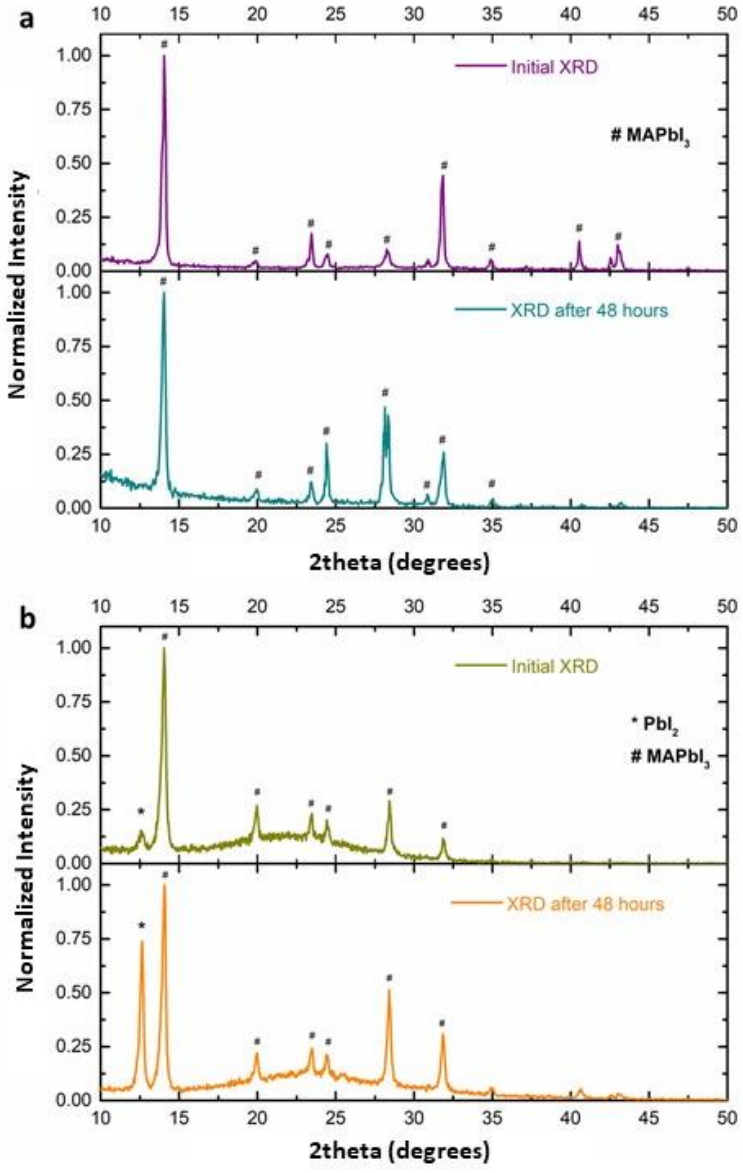

Figure 4.14: Ambient stability of microcrystal films over normal thin films of $MAPbI_3$ deposited over glass substrates.

The micrometer grain sized polycrystals of $MAPbI_3$ were found to be more environmentally stable than a solvent engineered spin coated thin film of the same material. The ambient stability of the materials was investigated using XRD. $MAPbI_3$ degrades to form PbI_2 and the observation of PbI_2 peaks in XRD indicates the completion of a long degradation reaction[29,30]. The XRD of the microcrystals did not show any degradation to the lead iodide phase even after 48 hours, whereas the solvent engineered thin films showed significant degradation to PbI_2 in 48 hours (Figure 4.14). Both the films were placed in room ambience (70 ± 5 % RH, 23 ± 2 ^oC). The increase in ambient stability of microcrystalline film can be attributed to the reduction in grain boundaries of the film. It was reported that the moisture attack initiates through the grain boundaries of perovskite films and reduction in grain boundaries can in turn improve the ambient stability[31]. A detailed explanation on the degradation process is provided in Chapter 5.

4.10 Conclusion

In summary, the role of solvents in the crystallization of lead halide perovskites by AVC was examined. It was found that GBL is the only solvent, that can be used to crystallize $MAPbI_3$ by anti-solvent diffusion. $MAPbBr_3$ was able to crystallize in DMF and DMSO based precursors. The scope of this work was limited to room temperature AVC with DCM as the common anti-solvent for all the crystallization processes. The mechanism of crystallization of lead halide perovskites by anti-solvent vapor diffusion to its precursors was examined for the first time. The investigations highlighted heterogeneous nature of crystallization with surfaces of the crystallization dishes providing the requisite energy to overcome the nucleation barrier. In normal AVC, heterogeneous nucleation and three-dimensional growth results in the formation of millimeter-sized perovskite crystals. The crystallization process was slow and took a few days to grow millimeter sized crystals. The system moved to predominant homogeneous nucleation when perturbed by ultrasonication (in S-AVC) and then the initial crystallization as well as growth take place in the precursor dispersion bulk. S-AVC deposition method can be utilized to grow crystals over any substrates, as the

initial nucleation and growth of the seed crystals were independent of substrate surfaces. The method was utilized to grow highly crystalline layers of $MAPbBr_3$ and $MAPbI_3$ on flexible and rigid substrates. The thickness and coverage of the crystals over the substrates were dependent. The thicknesses needed to be in tens of micrometers in dimension to ensure a pinhole free coverage. The grown crystals also had exemplary adhesiveness to the substrates and were even mechanically polishable using optical sandpapers. The S-AVC grown crystal films had much better room ambient stability when compared to polycrystalline thin films. The high thickness of the crystal layers hampered its application in thin film optoelectronic devices. However, the tightly packed and highly crystalline perovskite layers grown over substrates by S-AVC deposition method can be utilized to fabricate planar optoelectronic devices.

4.11 References

1. Tidhar, Y. *et al.* Crystallization of methyl ammonium lead halide perovskites: Implications for photovoltaic applications. *J. Am. Chem. Soc.* **136**, 13249–13256 (2014).

2. Saidaminov, M. I., Abdelhady, A. L., Maculan, G. & Bakr, O. M. Retrograde solubility of formamidinium and methylammonium lead halide perovskites enabling rapid single crystal growth. *Chem. Commun.* **51**, 17658–17661 (2015).

3. Saidaminov, M. I. *et al.* High-quality bulk hybrid perovskite single crystals within minutes by inverse temperature crystallization. *Nat. Commun.* **6**, 1–6 (2015).

4. Peng, W. *et al.* Solution-Grown Monocrystalline Hybrid Perovskite Films for Hole-Transporter-Free Solar Cells. *Adv. Mater.* **28**, 3383–3390 (2016).

5. Chen, Y. X. *et al.* General Space-Confined On-Substrate Fabrication of Thickness-Adjustable Hybrid Perovskite Single-Crystalline Thin Films. *J. Am. Chem. Soc.* **138**, 16196–16199 (2016).

6. Chen, Z. *et al.* Thin single crystal perovskite solar cells to harvest below-bandgap

light absorption. *Nat. Commun.* **8**, 1890 (2017).

7. Chen, Z. *et al.* Single-Crystal $MAPbI_3$ Perovskite Solar Cells Exceeding 21 % Power Conversion Efficiency. *ACS Energy Lett.* **4**, 1258–1259 (2019).

8. Alsalloum, A. Y. *et al.* Low-Temperature Crystallization Enables 21.9 % Efficient Single-Crystal $MAPbI_3$ Inverted Perovskite Solar Cells . *ACS Energy Lett.* **5**, 657–662 (2020).

9. Adhyaksa, G. W. P. *et al.* Understanding Detrimental and Beneficial Grain Boundary Effects in Halide Perovskites. *Adv. Mater.* **30**,1804792 (2018).

10. Yan, K. *et al.* Hybrid Halide Perovskite Solar Cell Precursors: Colloidal Chemistry and Coordination Engineering behind Device Processing for High Efficiency. *J. Am. Chem. Soc.* **137**, 4460–4468 (2015).

11. Hamill, J. C., Schwartz, J. & Loo, Y. L. Influence of Solvent Coordination on Hybrid Organic-Inorganic Perovskite Formation. *ACS Energy Lett.* **3**, 92–97 (2018).

12. Radicchi, E., Mosconi, E., Elisei, F., Nunzi, F. & De Angelis, F. Understanding the Solution Chemistry of Lead Halide Perovskites Precursors. *ACS Appl. Energy Mater.* **2**, 3400–3409 (2019).

13. Manser, J. S., Saidaminov, M. I., Christians, J. A., Bakr, O. M. & Kamat, P. V. Making and Breaking of Lead Halide Perovskites. *Acc. Chem. Res.* **49**, 330–338 (2016).

14. Nayak, P. K. *et al.* mechanism for rapid growth of organic inorganic halide perovskite crystals. *Nat. Commun.* **7**, 1–8 (2016).

15. Zhumekenov, A. A. *et al.* The Role of Surface Tension in the Crystallization of Metal Halide Perovskites. *ACS Energy Lett.* **2**, 1782–1788 (2017).

16. Cao, J. *et al.* Identifying the Molecular Structures of Intermediates for Optimizing the Fabrication of High-Quality Perovskite Films. *J. Am. Chem. Soc.* **138**, 9919–9926 (2016).

17. Rong, Y. *et al.* Solvent engineering towards controlled grain growth in perovskite planar heterojunction solar cells. *Nanoscale* **7**, 10595–10599 (2015).

18. Pratap, S., Keller, E. & Müller-Buschbaum, P. Emergence of lead halide perovskite colloidal dispersions through aggregation and fragmentation: Insights from the nanoscale to the mesoscale. *Nanoscale* **11**, 3495–3499 (2019).

19. Zijlema, T. G., Oosterhof, H., Witkamp, G. J. & Rosmalen, G. M. Van. Crystallization of Sodium Chloride with Amines as Antisolvents. *Seperation and Purification by Crystallization* Eds.: Botsaris, G. D. & Toyokura, K. 230–241 (1997).

20. Oosterhof, H., Witkamp, G.-J. & van Rosmalen, G. M. Antisolvent Crystallization of Anhydrous Sodium Carbonate at Atmospherical Conditions. **47**, 602-608 (2001).

21. Nowee, S. M., Abbas, A. & Romagnoli, J. A. Antisolventcrystallization Model identification, experimental validation and dynamic. *Chem. Engin. Sci*. **63**, 5457-5467 (2008)

22. Haller, I. Covalently attached organic monolayers on semiconductor surfaces. *J. Am. Chem. Soc.* **100**, 8050–8055 (1978).

23. Acres, R. G. *et al.* Molecular structure of 3-aminopropyltriethoxysilane layers formed on silanol-terminated silicon surfaces. *J. Phys. Chem. C* **116**, 6289–6297 (2012).

24. Zeng, X., Xu, G., Gao, Y. & An, Y. Surface wettability of (3-Aminopropyl)triethoxysilane self-assembled Monolayers. *J. Phys. Chem. B* **115**, 450–454 (2011).

25. Tillman, N., Ulman, A., Schildkraut, J. S. & Penner, T. L. Incorporation of Phenoxy Groups in Self-Assembled Monolayers of Trichlorosilane Derivatives: Effects on Film Thickness, Wettability, and Molecular Orientation. *J. Am. Chem. Soc.* **110**, 6136–6144 (1988).

26. Yamada, T., Yamada, Y., Nakaike, Y., Wakamiya, A. & Kanemitsu, Y. Photon

Emission and Reabsorption Processes in $CH_3NH_3PbBr_3$ Single Crystals Revealed by Time-Resolved Two-Photon-Excitation Photoluminescence Microscopy. *Phys. Rev. Appl.* **7**, 1–8 (2017).

27. Wu, B. *et al.* Discerning the Surface and Bulk Recombination Kinetics of Organic–Inorganic Halide Perovskite Single Crystals. *Adv. Energy Mater.* **6**, 1–9 (2016).

28. Poglitsch, A. & Weber, D. Dynamic disorder in methylammoniumtrihalogenoplumbates (II) observed by millimeter-wave spectroscopy. *J. Chem. Phys.* **87**, 6373–6378 (1987).

29. Aristidou, N. *et al.* The Role of Oxygen in the Degradation of Methylammonium Lead Trihalide Perovskite Photoactive Layers. *Angew. Chemie - Int. Ed.* **54**, 8208–8212 (2015).

30. Niu, G. *et al.* Study on the stability of CH3NH3PbI3 films and the effect of post-modification by aluminum oxide in all-solid-state hybrid solar cells. *J. Mater. Chem. A* **2**, 705–710 (2014).

31. Wang, Q. *et al.* Scaling behavior of moisture-induced grain degradation in polycrystalline hybrid perovskite thin films. *Energy Environ. Sci.* **10**, 516–522 (2017).

Chapter 5

Spherulitic Crystallization by Inducing Heterogeneous Nucleation and Growth on Substrate Surface.

Perovskite optoelectronic devices utilize their thin pinhole free films, of thicknesses typically lesser than 1 µm. The crystal growth technique developed in the previous chapter yielded films, a hundred times larger in thickness, thus making it non-viable to fabricate vertical optoelectronic devices. In this chapter the facile spin coating technique commonly used to deposit perovskite thin films was modified, to grow pinhole free spherulitic crystal films of $MAPbI_3$, with high degree of crystallinity and preferred orientation over the device substrates. Optoelectronic quality and ambient stability of the spherulitic crystal films are investigated and discussed. The thickness controllability of this technique makes it desirable to fabricate vertical devices.

Data and figures in this chapter are adapetd from: Riyas Ahmad, Pio John S. Buenconsejo, Ming Pin Alan Lim, P.C. Harikesh, Vipinraj Sugathan, Reinhard Haselsberger, Bening Titra Muhammad, Teck Ming Koh, Annalisa Bruno, Wei Lin Leong, Nripan Mathews, Maria-Elisabeth Michel-Beyerle, Subodh G. Mhaisalkar, Highly Crystalline and Oriented $MAPbI_3$ Spherulitic Films by Tailoring Crystal Growth Kinetics. (in publication).

5.1 Introduction: Shortcomings of Sonication Modified Anti-solvent Vapor Crystallization

The ultrasonication of supersaturated AVC system induced homogeneous nucleation in the precursor bulk and resulted in the growth of $MAPbI_3$ as well as $MAPbBr_3$ on substrates as explained in the previous chapter. The crystal films had an average grain size of around hundred micrometers. The grown crystals had good adhesiveness with the substrate surfaces making it favorable to fabricate optoelectronic devices.

However, the method had many shortcomings hampering its prudent utilization. The perovskite films crystallized had thicknesses around hundred micrometers. By virtue of its high absorption coefficient, perovskite photovoltaic cells employ an absorber layer typically less than 1 μm in thickness. As explained in the previous chapter, the thickness and surface coverage were dependent and a reduction in thickness was found to reduce the surface coverage. For photovoltaic devices, the photo-active layer needs to be pinhole free and thus the S-AVC films were unable to be utilized for photovoltaic cells. Moreover, the surface of the films was extremely rough to fabricate devices on top. The XRD revealed that the crystals are randomly oriented on the substrate. Most of the optoelectronic devices require semiconductor materials with specific crystallographic orientation. Moreover, the S-AVC technique was difficult to control, as the nucleation and growth processes were initiated by ultrasonication. The S-AVC was a slow process spanning 2-3 days for cessation. Due to this long duration, the process was incompatible with metallic substrates and electrodes. The metal electrodes were found to be chemically reacting with the perovskite precursor. Since the initial nucleation and growth took place in the precursor, the films also had poor substrate film electronic interfaces, retarding the charge transport across the interfaces.

The drawbacks of the S-AVC process arose primarily by the far flung nucleation sites from the substrate surface. Since the initial nucleation and growth was not on the substrate surface, the crystallization was random and non-oriented. In order to achieve an oriented and controllable crystal growth on substrates, the nucleation has to be initiated on the substrate surface. One of the important advantages of lead halide perovskites over inorganic semiconductors is their facile thin film deposition process.

The thickness of the formed polycrystalline films is easy to control in thin film deposition processes like spin coating. In normal polycrystalline thin film deposition of lead halide perovskites, anti-solvents are dropped on the spinning substrate to increase the number of nucleation centers and substrate coverage[1]. The work in this chapter modifies the spin coating process of lead halide perovskites, in order to confine the nucleation sites only to the substrate surfaces. The nucleation and grain growth are optimized to form a highly crystalline, thickness controlled perovskite layer with grain sizes above 100 μm, suitable for the fabrication of photovoltaic cells.

5.2 Theory of Nucleation and Grain Growth of Perovskite Thin Films

In a normal spin coating deposition of perovskite film, anti-solvent is dropped on the spinning substrate with precursor as shown in Figure 5.1. The system will have three types of nucleation centers: (a) homogeneous nucleation in the precursor due to supersaturation, (b) heterogeneous nucleation on the substrate-precursor interface, aided by the substrate surface energy and (c) heterogeneous nucleation on solid impurities in the system[2]. The nucleation on solid impurities is neglected and the homogeneous and heterogeneous nucleation processes are discussed in the following section.

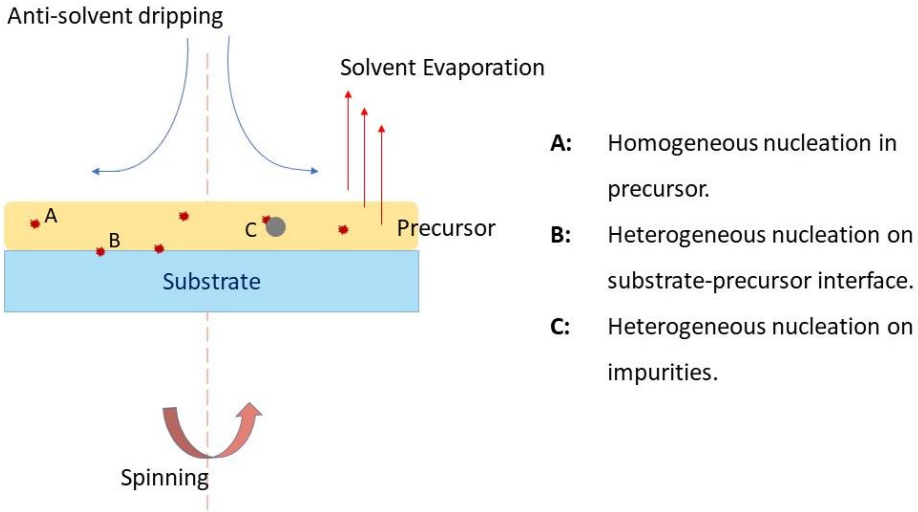

Figure 5.1: The nucleation processes in spin coating process with anti-solvent dripping of perovskites.

5.2.1 Homogeneous and Heterogeneous Nucleation

The spinning and anti-solvent dripping leads to the evaporation and driving off of excess solvents from the precursor, creating supersaturation as shown in Figure 5.1. Reduction in Gibbs free energy of the system drives the nucleation process in saturated perovskite precursors. Saturated precursors have high Gibbs free energy and the system tries to reduce it by segregation.

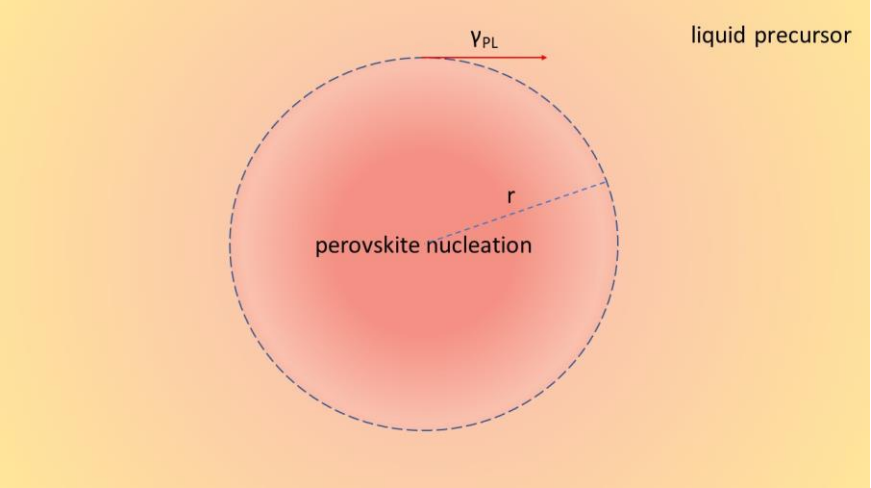

Figure 5.2: Homogeneous nucleation in perovskite precursor by supersaturation.

Assume that the liquid perovskite nucleates as shown in Figure 5.2 to form a solid nucleus and the nucleation is perfectly homogeneous. The total free energy change in the process can be expressed as:

$$\Delta G(r)_{homo} = \Delta\mu_v + \Delta\mu_s$$

where r is the radius of the nucleus formed, $\Delta\mu_v$ is the free energy change for the nucleation and $\Delta\mu_s$ is the increase in liquid-solid interface surface energy resulting from the nucleation. Hence,

$$\Delta G(r)_{homo} = \frac{4}{3}\pi r^3 \Delta G_v + 4\pi r^2 \gamma_{PL}$$

where ΔG_v is the change of Gibbs free energy per unit volume of the solid phase and γ_{PL} is the relative surface energy of the solid perovskite – liquid precursor interface.

ΔG_v can be expressed as $\Delta G_v = -\frac{kT}{V} ln \frac{C}{C_0}$, where V is the molecular volume of the nucleus, C is the concentration of the precursor and C_0 is its solubility limit. It must be noted that, $C > C_0$ for ΔG_v to be negative and for nucleation to take place. Therefore,

$$\Delta G(r)_{homo} = -\frac{4}{3}\pi r^3 \frac{kT}{V} ln \frac{C}{c_0} + 4\pi r^2 \gamma_{PL}$$

The formed homogeneous nucleus is stable in the precursor only if its radius exceeds a critical size, else it would dissolve back into the precursor. At the critical radius r = r^*,

$$\frac{d\Delta G_{homo}}{dr}_{r*} = 0$$

Therefore, the critical radius can be expressed as:

$$r^* = -2\frac{\gamma_{PL}}{\Delta G_v}$$

The homogeneous nucleation barrier can be expressed as:

$$\Delta G^*_{homo} = \frac{16\pi\gamma^3_{PL}}{3\Delta G^2_v}$$

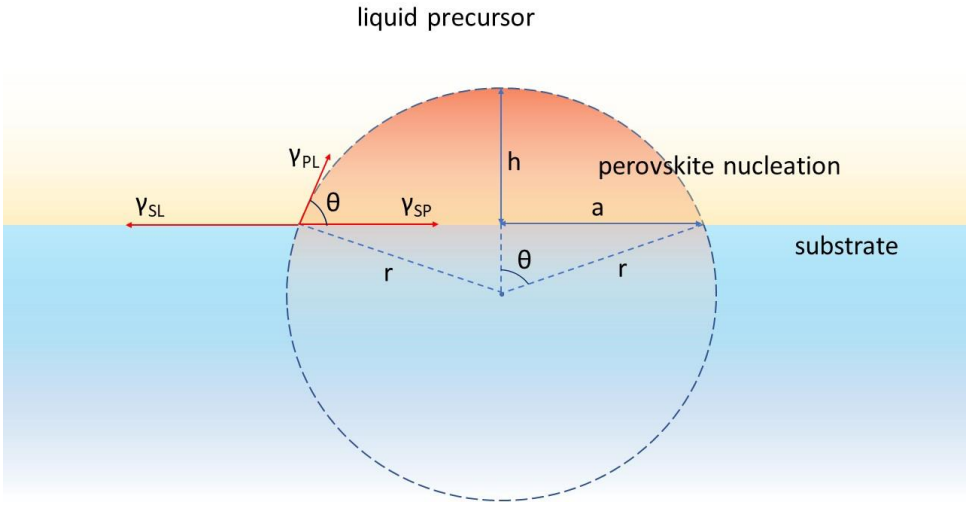

Figure 5.3: Heterogeneous nucleation at the substrate-precursor interface.

Since the substrate acts as a high energy surface, a considerable number of nucleation take place at the substrate-precursor interface as shown in Figure 5.3. Assume that the nucleus forms a spherical cap of height h over the substrate surface. γ_{SL} , γ_{PL}, γ_{SP} are the surface energies of substrate – liquid precursor, perovskite – liquid precursor and substrate – perovskite interfaces. The total free energy change in the heterogeneous nucleation process can be expressed as:

$\Delta G(r)_{het}$ = cap volume of the nucleus x $\Delta\mu_v$ + curved surface area of the cap x γ_{PL} + base area of the cap x γ_{SP} – base area of cap x γ_{SL}.

Cap volume of the nucleus,

$$V_c = \frac{1}{3}\pi h^2(3r - h) = \frac{1}{3}\pi r^3(2 + \cos\theta)(1 - \cos\theta)^2$$

Curved surface area of the cap,

$$S_c = 2\pi rh = 2\pi r^2(1 - \cos\theta)$$

Base area of the cap,

$$B_c = \pi a^2 = \pi r^2(\sin\theta)^2$$

Therefore, total Gibbs free energy change can be expressed as:

$$\Delta G(r)_{het} = k_v r^3 \Delta\mu_v + k_{s1} r^2 \gamma_{PL} + k_{s2} r^2 \gamma_{SP} - k_{s2} r^2 \gamma_{SL}$$

Where,

$$k_v = \frac{1}{3}\pi(2 + \cos\theta)(1 - \cos\theta)^2$$

$$k_{s1} = 2\pi(1 - \cos\theta)$$

$$k_{s2} = \pi\sin^2\theta$$

The formed heterogeneous nucleus is stable only if its radius exceeds a critical size, else it would dissolve back into the precursor. At the critical radius $r = r^*$,

$$\left.\frac{d\Delta G_{het}}{dr}\right|_{r*} = 0$$

Therefore, the critical radius can be expressed as:

$$r^* = \frac{-2(k_{s1}\gamma_{PL} + k_{s2}\gamma_{SP} - k_{s2}\gamma_{SL})}{3k_v\Delta\mu_v}$$

Applying the Young's equation, $\gamma_{SL} = \gamma_{SP} + \gamma_{PL}\cos\theta$ and substituting for k_{s1}, k_{s2}, k_v and $\Delta\mu_v$ heterogeneous nucleation barrier can be obtained as:

$$\Delta G^*_{het} = \frac{16\pi\gamma^3_{PL}}{3\Delta G^2_v}\left\{\frac{(2+cos\,\theta)(1-cos\,\theta)^2}{4}\right\}$$

i.e.

$$\Delta G^*_{het} = \Delta G^*_{homo}[f(\theta)]$$

For the wetting angles, $0^0 < \theta < 180^0$, $f(\theta) < 1$

$$\Delta G^*_{het} < \Delta G^*_{homo}$$

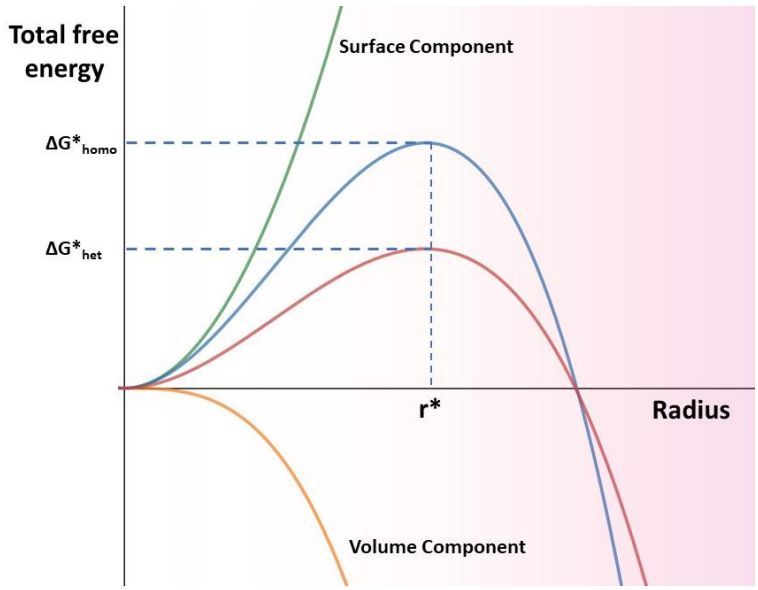

Figure 5.4: The free energy barrier for homogeneous and heterogeneous nucleation centers of lead halide perovskites.

It has to be noted that, while spin coating of perovskite precursors, heterogenous nucleation barrier is always lower than homogeneous barrier. Homogeneous nucleation prevails unless there are high energy surfaces in the crystallization system. In presence of high energy surfaces like solid segregations in the precursor or the substrate surfaces used for spin coating, the system gets additional low barrier paths for heterogeneous nucleation. Hence during spin coating of perovskites, the probability of formation of heterogeneous nuclei significantly exceeds the chances of homogeneous nucleation. In normal perovskite spin coating technique, a bad solvent (anti-solvent) is dripped over the spinning perovskite precursor on the substrate. The bad solvent drives away the excess solvent from the precursor and creates supersaturation, thereby inducing homogeneous nucleation. Upon elimination of the anti-solvent dripping step the nucleation can be consolidated on the substrate surface. The supersaturation as the result of solvent evaporation can be reduced by using solvents with high boiling point and higher coordination capability. The boiling points of the commonly used solvents varies in the order, GBL > DMSO > DMF > ACN[3] .

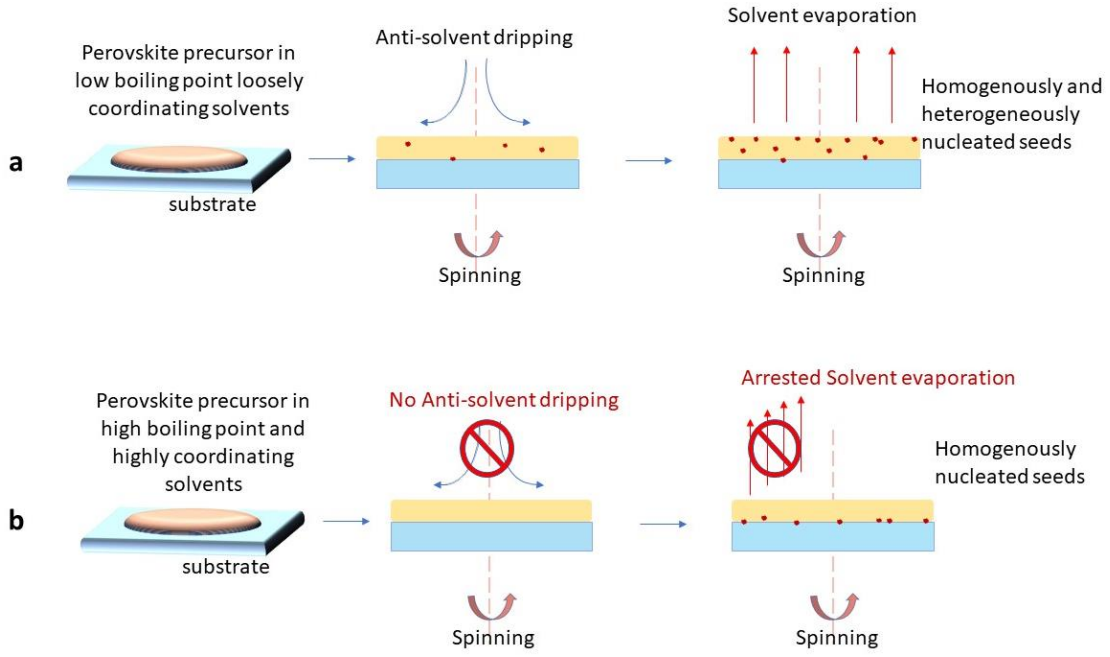

Figure 5.5: (a) Nucleation in normal spin coating with anti-solvent dripping, (b) Nucleation in modified spin coating process.

5.2.2 Grain Growth and Thin Film Formation

Once the critical radius is attained the nuclei grow into perovskite crystals. The nuclei with radii lesser than the critical radius will be dissolved back to the precursor. The nucleus grows both in plane as well as out of plane from the substrate. The ratio of in plane dimension (d_i) to out of plane dimension (d_p) of a grain can be called as its aspect ratio ($A = d_i/d_p$). Like normal inorganic semiconductors, in normal perovskite thin films, the lateral dimension of a grain almost equals it's out of plane dimensions (thickness)[4]. For increasing the aspect ratio, the grains must grow in an asymmetric manner.

Consider a nucleus (lead halide perovskite region in a sea of precursors) of radius a, formed over substrate as given in the figure. For maximizing the aspect ratio, the diffusion radius δ, the area from where precursors can diffuse to the nucleus to propagate its growth, should be maximized.

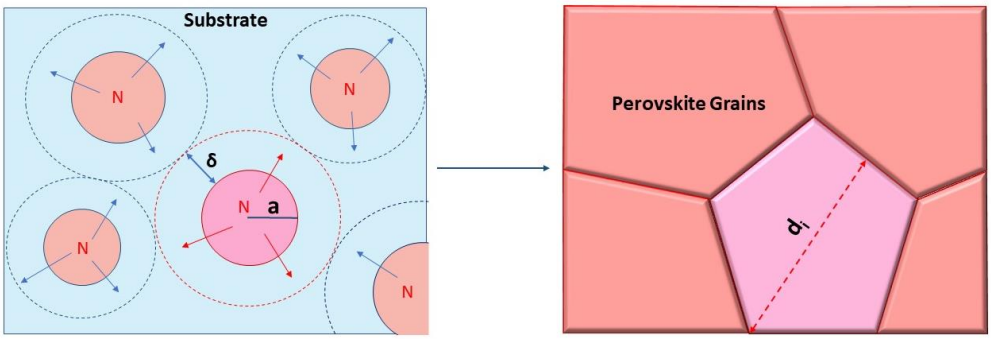

Figure 5.6: The process of grain growth over a substrate. The precursors diffuse from a distance δ to the nuclei to maintain the gain growth.

Since hydrophilic substrates (substrates are UV-ozone cleaned before spin coating the perovskite layer) were used here, the absolute value of activation energy for surface diffusion (ΔG_m) of precursors will be high (making the precursor diffusion difficult)[5] and in such cases δ increases with increasing temperatures[6,7]. The restricted surface diffusion capability can be overcome by using highly supersaturated solution as it can provide easy and surplus supply of precursors for maintaining continuous grain growth.

When diffusion width δ completely cover the substrate surface a saturation in the number of nuclei per unit area on the substrate surface (N_{max}) is reached. A large δ limits the number of nucleation sites and allows the growth of large well packed μm sized crystal grains. The nucleus grows outward in plane and impinges with adjacent nuclei. The lateral grain size at impingement can be given as

$$d_i = 1.351\,\delta + 1.203\left(\frac{G_0}{I}\right)^{\frac{1}{3}}$$

where G_0 is proportional to deposition rate, which is very high in the case of spin coating as ad-atoms are in the immediate vicinity of the substrate surface. d_i can be further increased by reducing the rate of nucleation, I. The rate of nucleation can be reduced by (a) using solvents with high boiling points and coordinating capabilities (b) using a low temperature and slow annealing processes. But it has to be noted that a low temperature grain growth reduces δ and can reduce the crystal aspect ratio. Therefore, there should be a tradeoff between rate of nucleation and diffusion radius.

5.3 Selection of Solvents for Inducing Heterogeneous Nucleation and Growth

As discussed in the previous chapter DMF, DMSO, GBL and ACN are the most commonly used solvents for perovskite deposition. In this work, the solvents with low solubilities were ruled out.

1 M precursors were made in DMF, DMSO and GBL for $MAPbI_3$. GBL was not used for $MAPbBr_3$ due to its poor solubility and the precursors were spin coated on glass substrates without anti-solvent dripping, so as to reduce the homogeneous nucleation centers as explained in the previous section. DMF having the lowest boiling point in the lot formed perovskite phase before annealing. The excess solvents were driven off as a result of spinning causing supersaturation, nucleation and growth. It was surprising that (as shown in Figure 5.7) GBL also showed significant perovskite phase upon spinning despite having the highest boiling point. However, DMSO having an intermediate boiling point, did not form any $MAPbI_3$ phase while spinning. This can be attributed to the strong precursor-solvent complex forming capability of DMSO,

which prevented it from crystallizing out the perovskite ($MAPbI_3$) phase. It has to be noted that DMSO, which was a bad solvent for crystallization of $MAPbI_3$ through AVC due to its strong coordinating capability, is a handy solvent for keeping the nucleation sites low and slowing down the nucleation rates.

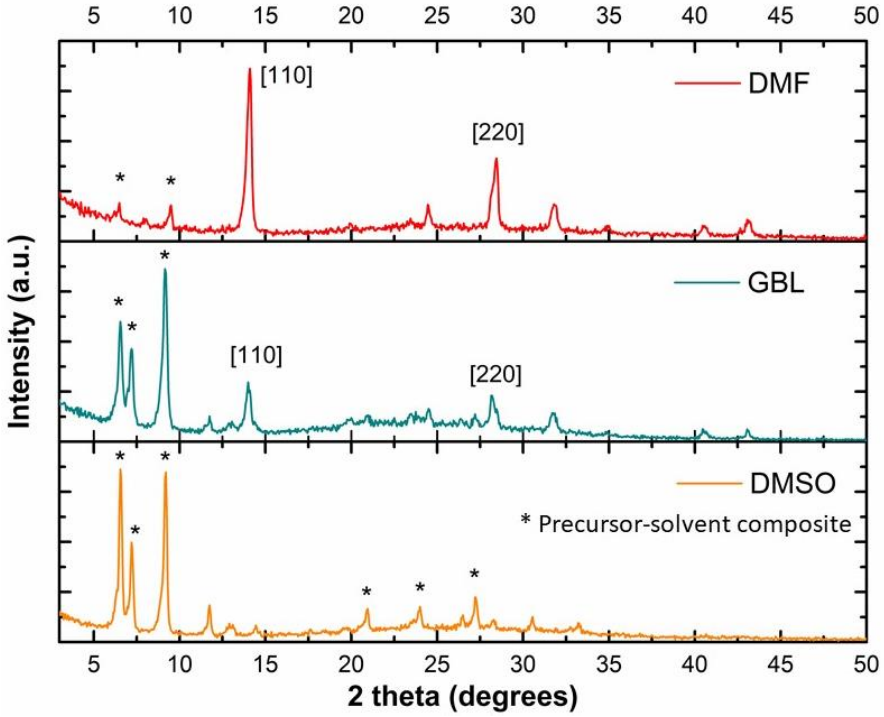

Figure 5.7: XRD of precursors after spinning prior to annealing.

XRD revealed that the precursor is $MA_2Pb_3I_8{\cdot}2DMSO$, the same composite crystallized when AVC in DMSO for $MAPbI_3$ was performed. In the case of $MAPbBr_3$, perovskite phases were crystallized in DMF as well as in more coordinating DMSO up on spinning (Appendix Figure A6).

5.4 Spherulitic Crystallization of $MAPbI_3$ Crystals

Since the annealing temperature affects the diffusion length (δ) of the precursors and the rate of nucleation (I), the crystallization is expected to significantly vary with temperature. The spin coated precursors were annealed at temperatures varying from 100 ^oC to 165 ^oC. For $MAPbI_3$, GBL based precursors did not show any change in

crystallization or crystalline orientation with annealing temperatures as shown in Figure 5.8. The films were discontinuous over the substrates with a 'dendritic' morphology.

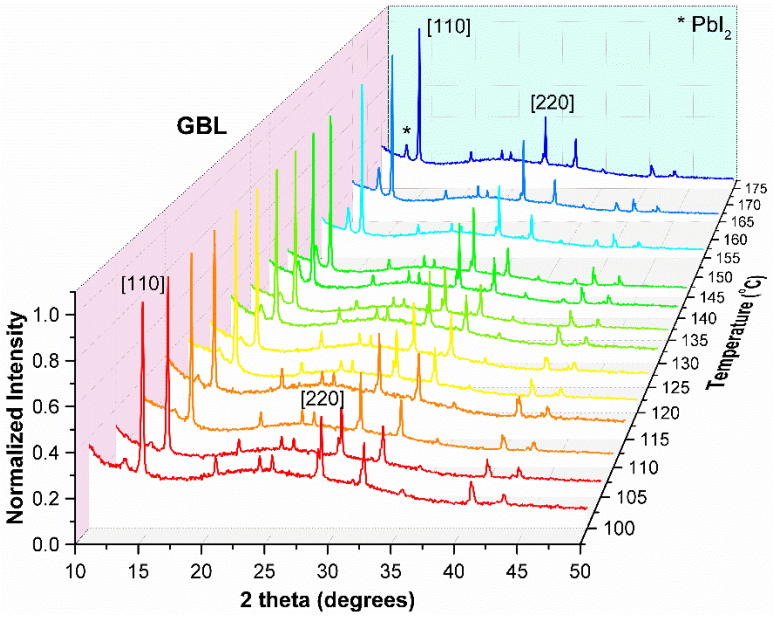

Figure 5.8: XRD for GBL based $MAPbI_3$ films with different annealing temperatures.

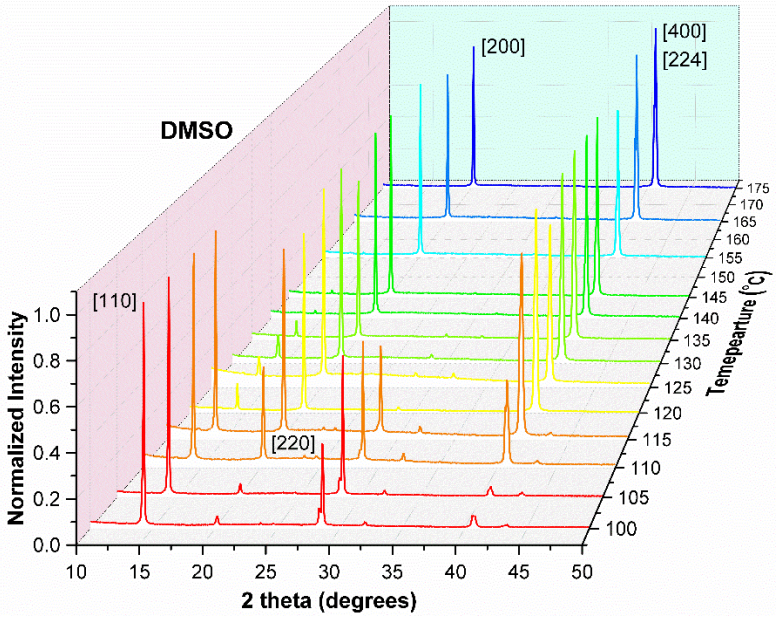

Figure 5.9: XRD for DMSO based $MAPbI_3$ films with different annealing temperatures.

The case of DMF based films were similar with a similar morphology to that of GBL based films. However, the crystalline orientation was found to be improving at temperatures around 165 ^{o}C (Appendix Figure A7). However, the morphology and orientation of DMSO based films showed an interesting trend. Though the films were dendritic for 100 ^{o}C annealing, the crystallites were highly oriented along [110] plane. As the temperature was increased from 100 ^{o}C, the preferred orientation of the crystals started changing to [200],[224] (Figure 5.9).

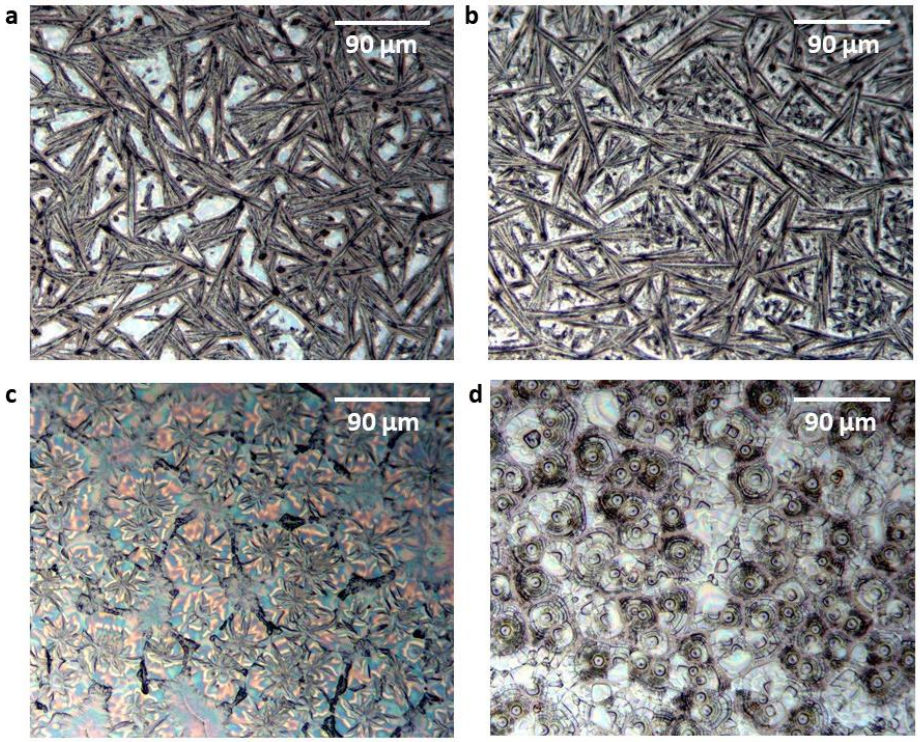

Figure 5.10: (a), (b) and (c) Morphology of $MAPbI_3$ film on ITO/SnO_2 substrate at 100 ^{o}C, 130 ^{o}C and 165 ^{o}C annealing, respectively. (d) Morphology of $MAPbBr_3$ on ITO/SnO_2 at 165 ^{o}C annealing (all of them grown with 1 M precursor).

The morphology of the films showed a drastic change at annealing temperatures above 165 ^{o}C. The morphology was no more dendritic, but spherulitic,[8–10] typical to many inorganic and organic materials as shown in Figure 5.10. The crystals were found to be growing radially outwards from a few well defined nucleation centers. The crystallinity as well as orientation of the films were highly improved at temperatures beyond 165

^{o}C, which are explained in the following sections. It was observed that the crystallinity and aspect ratio of the spherulitic crystals increased with high annealing temperatures and increased precursor concentrations. High co-ordination capability of DMSO allowed the preparation of highly concentrated precursors thereby increasing the deposition rate (G_o). The stable co-ordination complexes and high boiling point of DMSO also restricted the homogeneous nucleation, thus assisting in both heterogeneous nucleation and in plane crystal growth. In the case of $MAPbBr_3$ the orientation and morphology were found to be similar at all annealing temperatures, irrespective of solvents (Appendix Figure A8). The surface coverage of $MAPbBr_3$ films were poor leaving several areas of substrates exposed. In the previous chapter it was found that the colloidal chemistry of $MAPbBr_3$ precursors are similar irrespective of solvents, unlike $MAPbI_3$. $MAPbBr_3$ was also found to be crystallizing while spinning (before annealing) even with DMSO based precursors (Appendix Figure A6). It can be suspected that the nature of crystallization could be linked to the chemical nature of the precursors. A more detailed investigation on the chemistry of precursors is beyond the scope of this work.

Concluding the observations, it was found that DMSO can be used as the solvent to suppress the nucleation of perovskite phase while spinning of $MAPbI_3$ and to confine the nucleation on the substrate surfaces. The high coordination capability of DMSO reduced the rate of nucleation and also enabled the preparation of highly concentrated precursors, which improved the diffusion of 'adatoms' to the nucleation sites. The improved diffusion coupled with high temperature annealing enabled the growth of spherulitic crystals of $MAPbI_3$ with large aspect ratios. From here onwards, our focus of investigation and characterization is based on DMSO based spherulitic crystals.

5.5 Crystallinity and Orientation Investigations of Spherulitic Crystals

XRD was used as the primary technique to analyze the crystallinity and orientation of the deposited films. The *X*-ray diffractometer is operated in Bragg-Brentano geometry to study the out of plane growth of the crystals from the substrate surface. The

investigation employed spherulitic crystal films of $MAPbI_3$ and $MAPbBr_3$, from DMSO based precursors annealed above 165 ^oC.

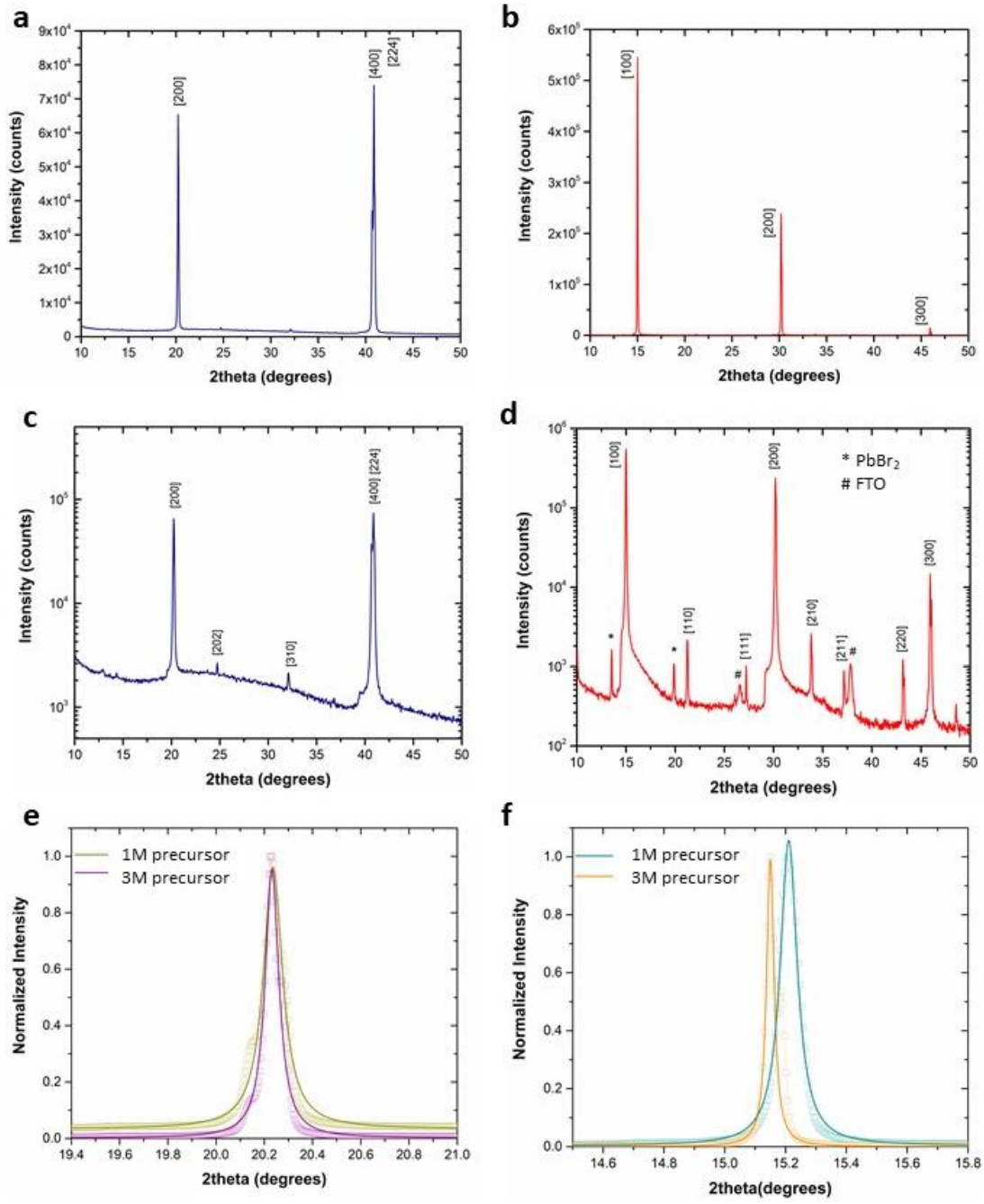

Figure 5.11: XRD of (a) $MAPbI_3$ and (b) $MAPBBr_3$ films deposited over FTO/SnO_2 by spin coating, (c) and (d) XRD intensities of $MAPbI_3$ and $MAPbBr_3$ in logarithmic scale, (e) FWHM of [200] peak of $MAPbI_3$ with increase in precursor concentration, (f) FWHM of [100] peak of $MAPbBr_3$.

$MAPbI_3$ films were extremely oriented along [200] and [224] planes out the substrate surface as shown in Figure 5.11a, c. All other diffraction peaks were highly suppressed. $MAPbBr_3$ films were preferentially oriented along [100] and [200] planes. In logarithmic scale, the XRD showed significant diffraction intensities of [110], [210] and [220] planes as shown in figure 5.11b, d. The XRD also had significant diffraction intensities from the substrates and unreacted $PbBr_2$ indicating improper coverage of $MAPbBr_3$ films. This makes $MAPbBr_3$ films unsuitable to fabricate vertical devices like photovoltaic cells.

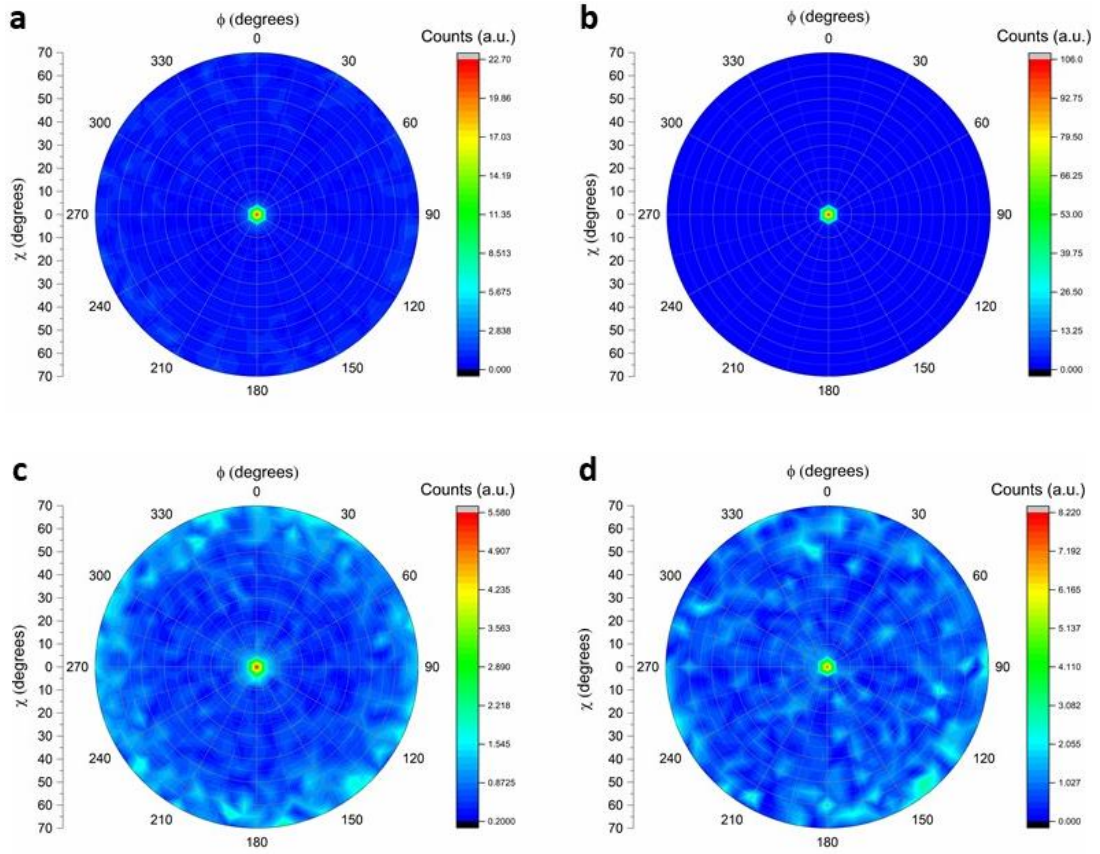

Figure 5.12: Out of plane *X*-ray pole figures of (a) [200] plane of $MAPbI_3$, (b) [224] plane of $MAPbI_3$, (c) [100] plane of $MAPbBr_3$, (d) [200] plane of $MAPbBr_3$ measured by rotating the samples from 0^o to 360^o at tilt angles ranging from 0^o to 70^o.

The degree of crystallinity of the samples were also examined from the full width half maximum (FWHM) of XRD in 'powder measurement' configuration. For $MAPbI_3$

films the FWHM was reduced from 0.1° to 0.08° upon increment in precursor concentration from 1 M to 3 M (Figure 5.11e). The increase in precursor concentration helped to enhance the grain size of films and thereby improving the surface coverage, thus making them suitable for optoelectronic device fabrication. As the concentration of precursors were increased for $MAPbBr_3$, the crystals were found to significantly grow laterally and out of the substrate surface as 3D crystals. It can reduce the lattice strains and will improve the FWHM of *X*-ray diffraction peaks. This was evident from the FWHM of XRD for $MAPbBr_3$ films, where the peak width was remarkably reduced from 0.08° to 0.03° on increasing the concentration from 1 M to 3 M (Figure 5.11f).

The texture analysis of the films was carried out using *X*-ray pole figure analysis (Figure 5.12). The out of plane crystal orientations of spin coated films were investigated. In this measurement, 2θ values were fixed for different diffraction peaks (2θ = 20.03°, 31.80°, 40.70° for $MAPbI_3$ corresponding to [200],[310], [224] planes and 2θ = 15.10°, 21.23°, 30.15° for $MAPbBr_3$ corresponding to [100], [110], [200] planes) and the samples were rotated from 0° to 360° at different tilt angles ranging from 0° to 70°. The pole figure plots yielded distinct spots on the stereographic projection circle. This shows that the films are composed of highly oriented crystals with respect to the substrate. For $MAPbI_3$, [200] and [224] poles are found at the center of the projection circle, indicating that these planes grow vertically out from the substrate surface. The extremely low intensity of X-rays detected at other areas of projection circle demonstrates the high degree of crystalline orientation. The out of plane intensities of other peaks (Appendix Figure A9) were significantly lower showing the preferred out of plane growth of [200] and [224].

For $MAPbBr_3$ the films were oriented along [100] and [200] planes, out of the substrate surface as shown in Figure 5.12c, d. However, $MAPbBr_3$ had an inferior texture when compared to $MAPbI_3$, since it had significant intensities at other angles apart from the center of the pole figure circle. It was observed earlier that $MAPbBr_3$ also had an inferior surface coverage on substrates. Thus, it was confirmed that $MAPbI_3$ films had superior texture and coverage over substrates when compared to $MAPbBr_3$, making it appropriate to fabricate optoelectronic devices. Since [224] and [400] diffraction peaks

of $MAPbI_3$ are extremely close to each other, it was unable to differentiate them using *X*-ray pole figure analysis.

5.6 Electron Backscatter Diffraction (EBSD) Measurements

It was observed that the spherulitic films of $MAPbI_3$ had a high degree of orientation along [200], [224] planes. In order to confirm the results obtained from *X*-ray diffraction, pole figures were constructed from electron backscatter diffraction for the deposited film.

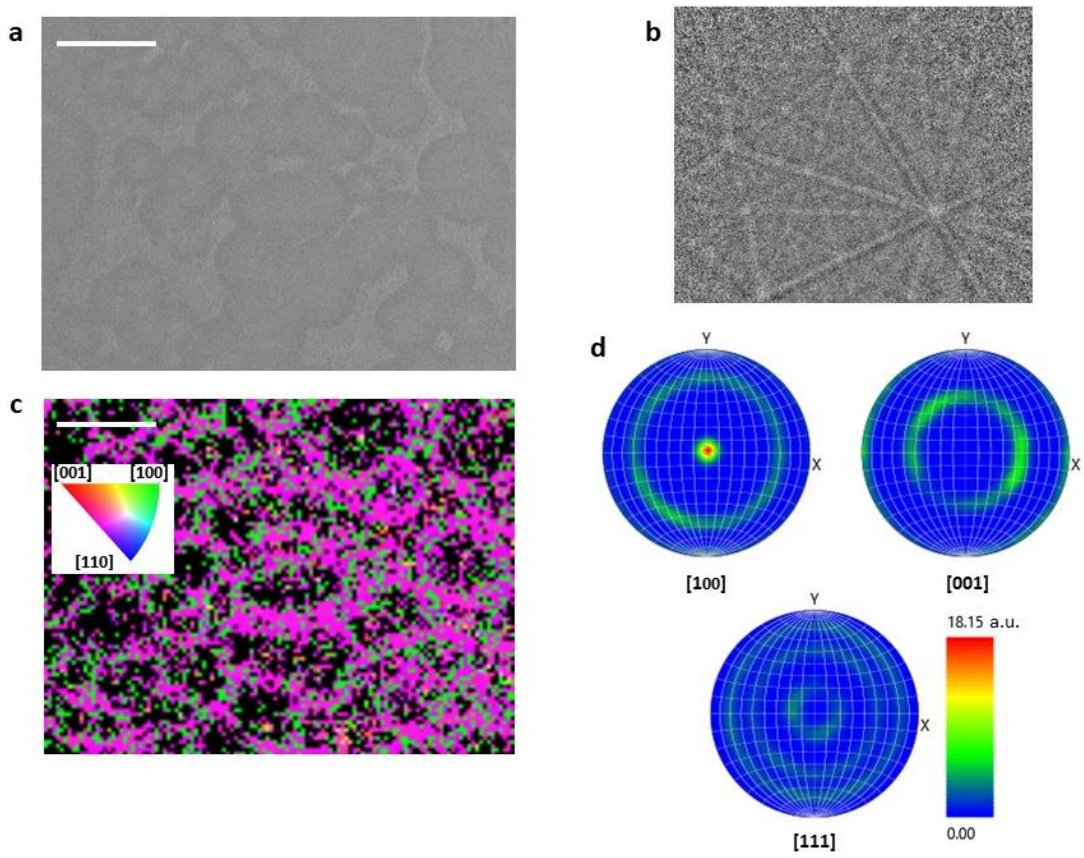

Figure 5.13: (a) SEM image of the film area where EBSD was carried out, (b) Kikuchi pattern obtained on the photographic plate for an indexed area on the film, (c) The IPF Z image for the scanned area (Scale bar: 250 μm for a and c) and (d) Calculated pole figures from the EBSD data using AZtec from Oxford Instruments.

Electron diffraction will also help to differentiate the [400] and [224] planes which are very close to be observed by *X*-ray diffraction angles. The EBSD set up was operated in beam defocusing mode, with an accelerating voltage of 15 kV and a probe current of 1 nA. A spot size of 2 μm was employed to scan the sample. The EBSD data was analyzed AZtec software from Oxford Instruments. The sample was found to be highly beam sensitive, with the electron beam damaging the sample upon repeated scanning. The inverse pole figure along Z direction (IPF Z) revealed an out of plane orientation along [200], [224] planes as shown in Figure 5.13c. The pole figures constructed from the data revealed a strong out of plane fiber texture for the $MAPbI_3$ film along these crystal planes (Figure 5.13d).

5.6 Morphology and Microstructure Investigations

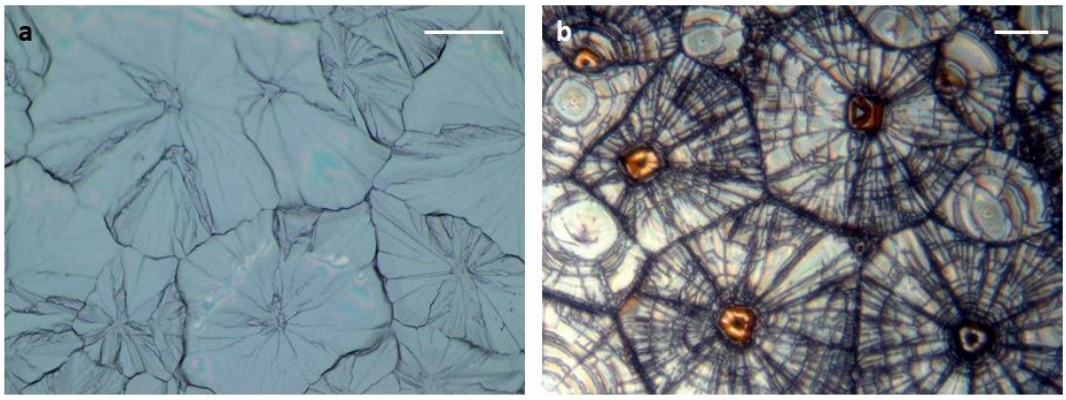

Figure 5.14: Optical microscopic images of (a) $MAPbI_3$ (scale 40 μm) and $MAPbBr_3$ (scale 90 μm) crystals spin coated from 3M DMSO based precursors and annealed at 165 ^oC.

The morphology of the crystal films was investigated using optical and electron microscopic techniques. A 3 M DMSO precursor based film had grain sizes typically ranging from 100 μm to 200 μm. These films were highly compact and pinhole free. But $MAPbBr_3$ films were discontinuous over substrate surfaces. The morphology of the films showed that the crystals grew radially outward from distinct nucleation sites as shown in Figure 5.14. Since the films were deposited by the process of spin coating,

thicknesses of the films were easily varied by varying the spin coating speeds. The thicknesses of the films were not uniform, with some grains being thicker than the rest of the film. Individual crystals also had thickness variations radially as well, with the thicknesses tapering towards the edges. The thicknesses of the films were investigated by cross-sectional SEM imaging. In this crystal growth technique, as explained in the previous sections the nucleation and growth of crystals happens exclusively on the surface of substrates. Since photovoltaic cells use transparent conductors like FTO and ITO, the roughness of their surfaces plays a crucial role on the growth of films.

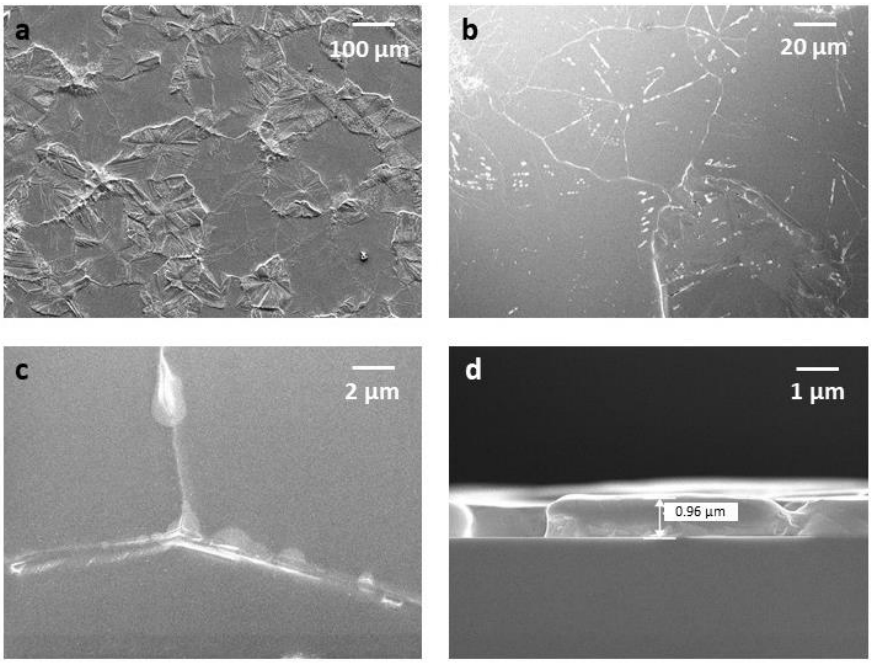

Figure 5.15: (a), (b) Surface morphology of $MAPbI_3$ crystal film spin coated over glass, (c) A triple junction grain boundary in the film, (d) Cross-section of $MAPbI_3$ film spin coated over glass.

FTO surfaces were found to be rougher than ITO upon surface examination (FTO: 10 nm rms, ITO 3 nm rms) (Appendix Figure A10). The crystals grown over FTO were discontinuous, possibly due to the higher surface roughness. However, the $MAPbI_3$ films were pinhole free and continuous over FTO/SnO_2 (20nm) and ITO/SnO_2 (20nm), probably because the SnO_2 layer assisted to reduce the surface roughness of these

transparent conductors (Figure 5.15). The $MAPbI_3$ films were continuous and well packed over glass substrates.

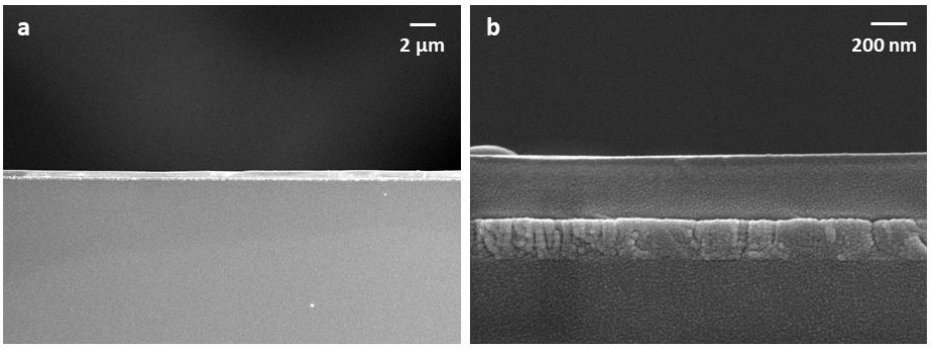

Figure 5.16: (a) $MAPbI_3$ crystal film grown on FTO/SnO_2, (b) $MAPbI_3$ films grown on ITO, by spin coating.

5.7 Trap Density Investigations

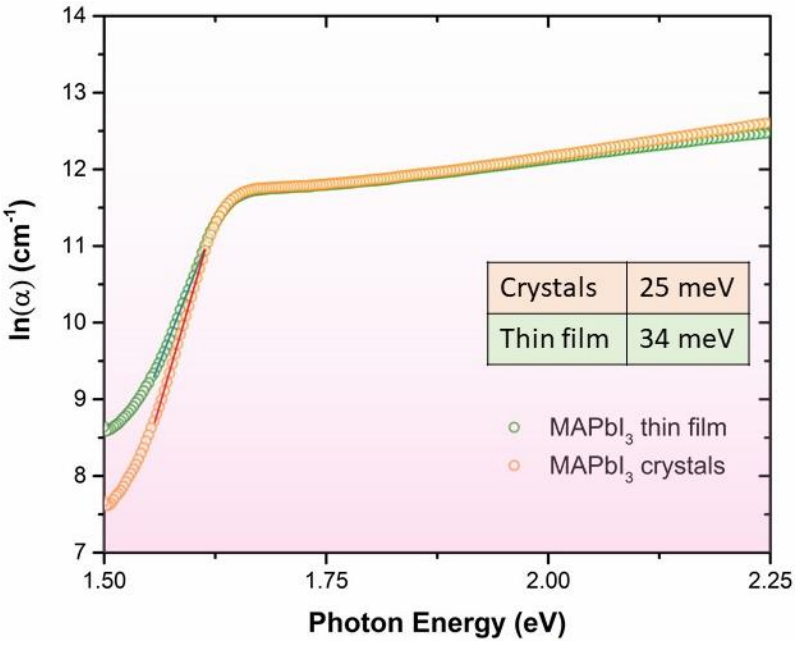

Figure 5.17: Comparison of Urbach tail of optical absorption onset for $MAPbI_3$ crystal film and normal thin film.

The optoelectronic quality of the deposited crystal films was analyzed using trap density measurements. The Urbach energy tail for the materials were calculated to analyze the sub-bandgap absorption from shallow defect states. The absorption coefficient (α) was calculated from the UV-Vis absorption spectra of the films. A ln(α) – photon energy curve was plotted as shown in Figure 5.17. The $MAPbI_3$ crystal films showed a much sharper absorption onset when compared to normal spin coated thin films, indicating its lower shallow defect densities. The calculated Urbach energy from the slopes of the absorption onsets were 25 meV for crystal films and 34 meV for normal thin films. However, Urbach energy tails obtained for $MAPbBr_3$ crystals and normal thin films were almost similar as shown in Appendix Figure A11.

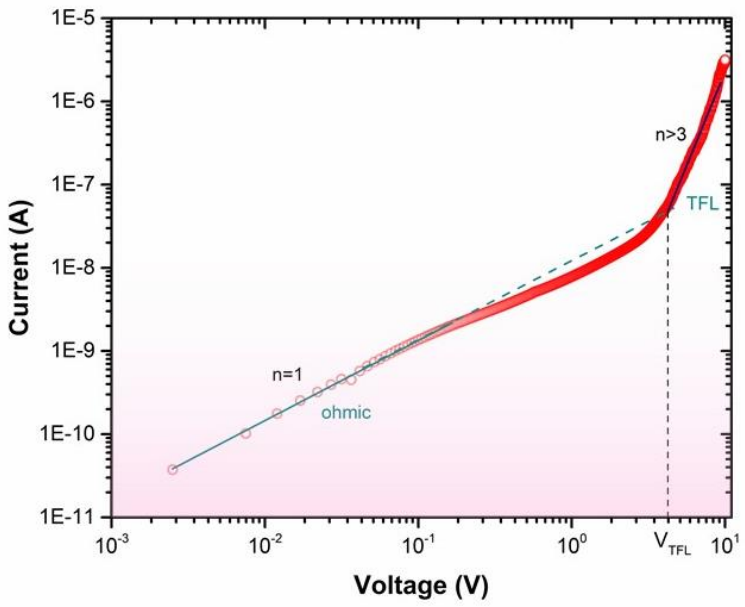

Figure 5.18: Defect density calculated from SCLC for $MAPbI_3$ crystal films.

The defect density in the material was calculated from space charge limited current values. As explained in the previous chapter the trap filling regime in semiconductors are associated with a steep rise in the current flowing through the material. Interdigitated FTO electrodes were used to inject current through the material. The current (*I*) – voltage (*V*) characteristics were measured and recorded. A *log (I) – log (V)* was plotted as shown in Figure 5.18. The trap density calculated from the trap filling

regime (V_{TFL}) was of the order of 10^{12} cm^{-3}, an order of magnitude higher than the values reported for $MAPbI_3$ single crystals[11]. Thus, it was revealed that the $MAPbI_3$ crystal films had better optoelectronic qualities when compared to its normal thin film counterpart. The photovoltaic and photodetector characteristics of these crystal films are provided in the following chapter.

5.8 Ambient Stability of Spherulitic Crystals

One of the major shortcomings faced by hybrid lead halide perovskites is its inherent instability towards ambient moisture and oxygen. In presence of humidity, $MAPbI_3$ forms monohydrate and dihydrate phases based on the extend of exposure[12,13]. The formation of dihydrate phase is accompanied by the formation of PbI_2, which indicates the irreversible degradation of $MAPbI_3$. The presence of O_2 accelerates the degradation process in the presence of humidity[14]. In presence of humidity and oxygen (at room ambience) the overall degradation process can be explained by the reaction,

$$CH_3NH_3PbI_3\ (s) + \frac{1}{4}O_2 \xrightarrow{H_2O} PbI_2\ (s) + CH_3NH_2 \uparrow + \frac{1}{2}I_2 + \frac{1}{2}H_2O$$

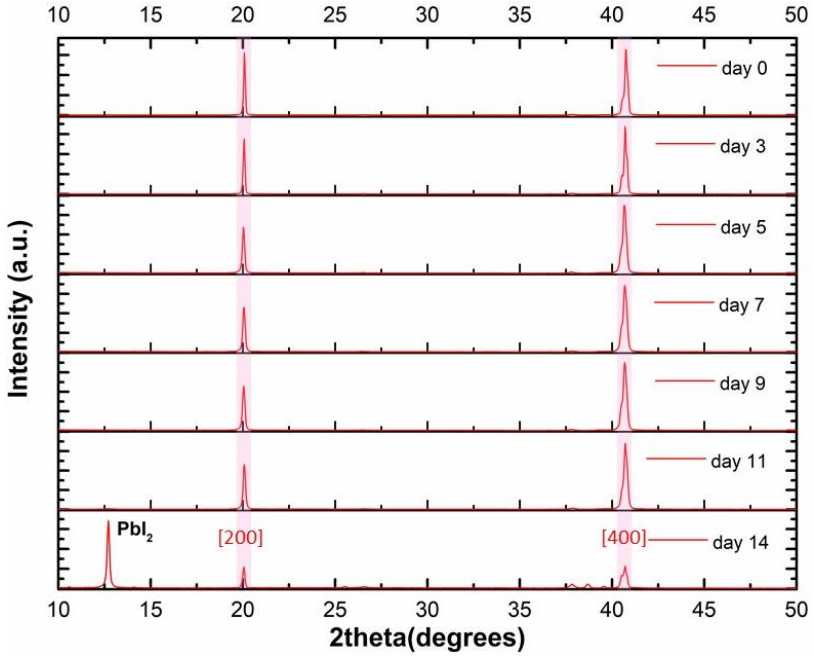

Figure 5.19: Ambient stability of spherulitic crystal films of $MAPbI_3$ deposited over glass substrates.

Hence the appearance of PbI_2 peak in the XRD of the samples can be used to identify the degradation process. In the previous chapter it was observed that, normal spin coated thin films of $CH_3NH_3PbI_3$ degrade significantly to PbI_2 (intensity of PbI_2 / intensity of [100] peak of $MAPbI_3$ = 0.75) in 48 hours of exposure to 70 ± 5% RH in presence of O_2 at 23 ± 2 ^oC (samples stored in dark).

However, in the case of $MAPbI_3$ spherulitic crystal film, the films did not show any PbI_2 peak even after 10 days of similar humidity and oxygen exposures, as shown in Figure 5.19. It was previously claimed that grain boundaries act as the channel for moisture ingress into the film and films with larger number of grain boundaries tend to degrade faster[15]. Our results reinforce the previous reports on the mechanism of degradation and the effect of grain boundaries on ambient stability of the material. Hence, it can be concluded that, improving the crystallinity of lead halide perovskite films is one of the strategies to enhance the ambient stability of the material, thereby placing it a step forward towards their device commercialization.

5.9 Conclusion

Concluding the chapter, the mechanism of nucleation and growth of perovskite crystals over substrate surfaces by spin coating was studied. It was identified that the nucleation process can be made completely heterogeneous by using a high coordinating and high boiling point solvent, DMSO. Spin coating without anti-solvent dripping and a quick annealing at elevated temperatures above 165 ^oC yielded spherulitic $MAPbI_3$ crystals of high aspect ratios. The surface coverage of the crystal films was adequate and pinhole free to fabricate vertical optoelectronic devices. However, $MAPbBr_3$ films had poor coverage and optoelectronic qualities for a fruitful device application. $MAPbI_3$ films had high crystallinity and were highly oriented along [200] and [224] planes out of the substrate surface, as analyzed by *X*-ray pole figure texture analysis. $MAPbI_3$ films had a low trap density of 10^{12} cm^{-3}. Since the films were formed by spin coating process, the thicknesses of the films were easy to vary by optimizing the spin coating parameters. In short, a method to grow highly crystalline layer of $MAPbI_3$ over device substrates was developed, that can be used to fabricate photodetectors and photovoltaic

cells. The optoelectronic devices fabricated by employing these films are explained in the following chapter.

5.10 References

1. Jeon, N. J. *et al.* Solvent engineering for high-performance inorganic–organic hybrid perovskite solar cells. *Nat. Mater.* **13**, 897–903 (2014).

2. Zhou, Y., Game, O. S., Pang, S. & Padture, N. P. Microstructures of Organometal Trihalide Perovskites for Solar Cells: Their Evolution from Solutions and Characterization. *J. Phys. Chem. Lett.* **6**, 4827–4839 (2015).

3. Hamill, J. C., Schwartz, J. & Loo, Y. L. Influence of Solvent Coordination on Hybrid Organic-Inorganic Perovskite Formation. *ACS Energy Lett.* **3**, 92–97 (2018).

4. Palmer, J. E., Thompson, C. V. & Smith, H. I. Grain growth and grain size distributions in thin germanium films. *J. Appl. Phys.* **62**, 2492–2497 (1987).

5. Chen, Z. *et al.* Thin single crystal perovskite solar cells to harvest below-bandgap light absorption. *Nat. Commun.* **8**, 1890 (2017).

6. Thompson, C. V. Grain growth in thin films. *Annu. Rev. Mater. Sci.* **20**, 245–268 (1990).

7. Thompson, C. V. Structure Evolution During Processing of Polycrystalline Films. *Mater. Sci.* **30**, 159-190 (2000).

8. Shtukenberg, A. G., Punin, Y. O., Gunn, E. & Kahr, B. Spherulites. *Chem. Rev.* **112** 1805–1838 (2012).

9. Ryschenkow, G. & Faivre, G. Bulk crystallization of liquid selenium Primary nucleation, growth kinetics and modes of crystallization. *J. Cryst. Growth* **87**, 221–235 (1988).

10. Wang, X., Liu, R., Wu, M., Wang, Z. & Huang, Y. Effect of chain disentanglement on melt crystallization behavior of isotactic polypropylene.

Polymer (Guildf). **50**, 5824–5827 (2009).

11. Saidaminov, M. I. *et al.* High-quality bulk hybrid perovskite single crystals within minutes by inverse temperature crystallization. *Nat. Commun.* **6**, 7586 (2015).

12. Leguy, A. M. A. *et al.* Reversible hydration of CH3NH3PbI3 in films, single crystals, and solar cells. *Chem. Mater.* **27**, 3397–3407 (2015).

13. Christians, J. A., Miranda Herrera, P. A. & Kamat, P. V. Transformation of the excited state and photovoltaic efficiency of CH3NH3PbI3 perovskite upon controlled exposure to humidified air. *J. Am. Chem. Soc.* **137**, 1530–1538 (2015).

14. Ahn, N. *et al.* Trapped charge-driven degradation of perovskite solar cells. *Nat. Commun.* **7**, 1–9 (2016).

15. Wang, Q. *et al.* Scaling behavior of moisture-induced grain degradation in polycrystalline hybrid perovskite thin films. *Energy Environ. Sci.* **10**, 516–522 (2017).

Chapter 6

Crystal Based Optoelectronic Devices and Characteristics

The role of crystallinity of perovskite layers in optoelectronic devices is not commonly investigated and compared. In this chapter the crystal films produced in the preceding chapters were utilized to fabricate photodetectors and photovoltaic cells. The device characteristics and their room ambient stability are examined and contrasted. This chapter also investigates the role of grain boundaries on ionic migration through the film by galvanostatic and impedance spectroscopy measurements.

Data and figures in this chapter are adapetd from: 1. Riyas Ahmad, Abhijith Surendran, P. C. Harikesh, Reinhard Haselsberger, Nur Fadilah Jamaludin, Rohit Abraham John, Teck Ming Koh, Annalisa Bruno, Wei Lin Leong, Nripan Mathews, Maria-Elisabeth Michel-Beyerle, Subodh G. Mhaisalkar, Perturbation-Induced Seeding and Crystallization of Hybrid Perovskites over Surface-Modified Substrates for Optoelectronic Devices, *ACS Applied Materials and Interfaces*, 31, 27727–27734 (2019).

2. Riyas Ahmad, Pio John S. Buenconsejo, Ming Pin Alan Lim, P.C. Harikesh, Vipinraj Sugathan, Reinhard Haselsberger, Bening Titra Muhammad, Teck Ming Koh, Annalisa Bruno, Wei Lin Leong, Nripan Mathews, Maria-Elisabeth Michel-Beyerle, Subodh G. Mhaisalkar, Highly Crystalline and Oriented $MAPbI_3$ Spherulitic Films by Tailoring Crystal Growth Kinetics. (in publication).

6.1 Introduction

Methylammonium lead halide perovskites have optoelectronic properties comparable to the best in class inorganic semiconductors along with facile thin film deposition processes, comparable to organic semiconductors, thus making it the best of both worlds. Most of the perovskite optoelectronic devices employ films which are polycrystalline with high density of grain boundaries which limit their intrinsic material properties. In the case of silicon photovoltaics, monocrystalline cells render higher device efficiency and ambient stability[1]. Similarly, perovskite photovoltaic cells are expected to have enhanced device performances upon improving the crystallinity of the light absorber layer[2].

In the previous two chapters, techniques were developed to grow highly crystalline layers of methylammonium lead iodide and bromide on substrate surfaces. The crystals grown by sonication modified AVC (S-AVC) were of high thickness and surface roughness, making them unable to fabricate vertical devices. Hence planar photoconductors were fabricated by growing perovskite crystals over patterned FTO electrodes. As the coverage of $MAPbBr_3$ were poor when compared to $MAPbI_3$, optoelectronic devices were fabricated using iodide perovskites. The quest to confine the nucleation and crystal growth on the substrate surfaces ended up with spherulitic crystallization. Spherulitic crystal growth technique enabled us to grow thin methylammonium based iodide and bromide lead perovskite crystals over substrates. This technique enabled us to grow smoother and thinner crystals, which helped us to fabricate vertical optoelectronic devices.

In this chapter, the characteristics of photodetectors and photovoltaic cells employing these crystals films are compared. Here, the optoelectronic device characteristics of lead halide perovskites are correlated to their levels of film crystallinity. The ionic conductance through the materials were investigated and compared using galvanostatic as well as impedance spectroscopy measurements, so as to correlate the effect of crystallinity on ionic migration.

6.2 Solvent Modified AVC (S-AVC) Crystal Based Photodetectors

The closely packed and pinhole-free $MAPbI_3$ crystals grown over the substrates were effectively used to fabricate planar optoelectronic devices. The growth of $MAPbI_3$ crystals were induced by S-AVC over laser-etched and prepatterned interdigitated FTO substrates to create planar photodetectors. The channel length between the electrodes was 100 μm, and the device had an active area of 3.17×10^{-6} m^2. The photodetectors thus formed were bottom illuminated from the glass side with a wavelength of 450 nm and were kept in a vacuum of 10^{-3} bar during all the measurements. Assuming the material to be intrinsic the photogenerated electrons and holes get swept across the semiconductor when an external bias is applied.

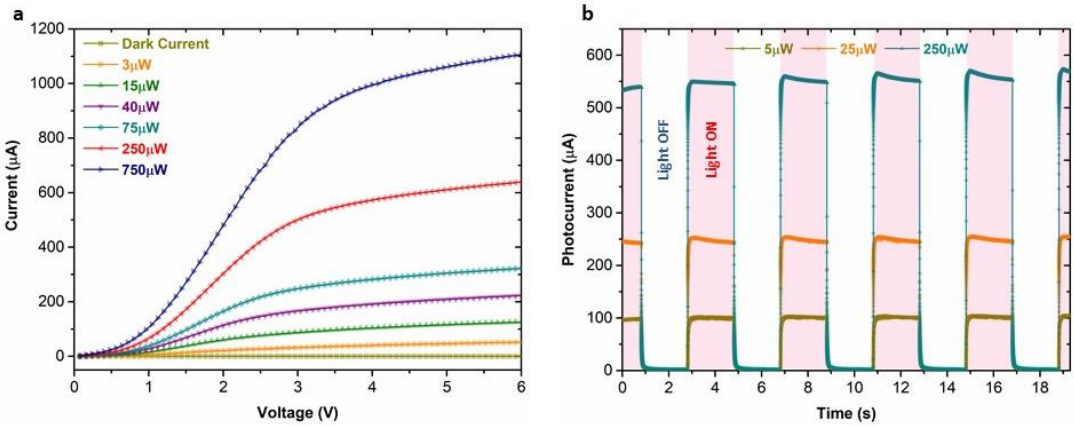

Figure 6.1: (a) S-AVC photodetector I-V characteristics for various illumination powers, (b) Pulsed light characteristics for the S-AVC based photodetector, for a biasing voltage of 8 V.

The current−voltage characteristics were measured for various illumination intensities as shown in Figure 6.1a. Owing to the superior crystallinity and large thickness of the grown perovskite crystals, the device generated very high photocurrents even for low power illumination (about 60 μA for 3 μW illumination).

Two key parameters, responsivity and detectivity, are commonly used to determine the sensitivity of a photodetector. The responsivity (*R*) of the photodetector can be calculated as

$$R = \frac{J_{ph}}{\phi} = \frac{I_{ph}}{\phi s}$$

where J_{ph} is the photocurrent density, ϕ is the incident light intensity, and s is the active area of the photodetector. The measured responsivity of the photodetector was 20 AW^{-1}.

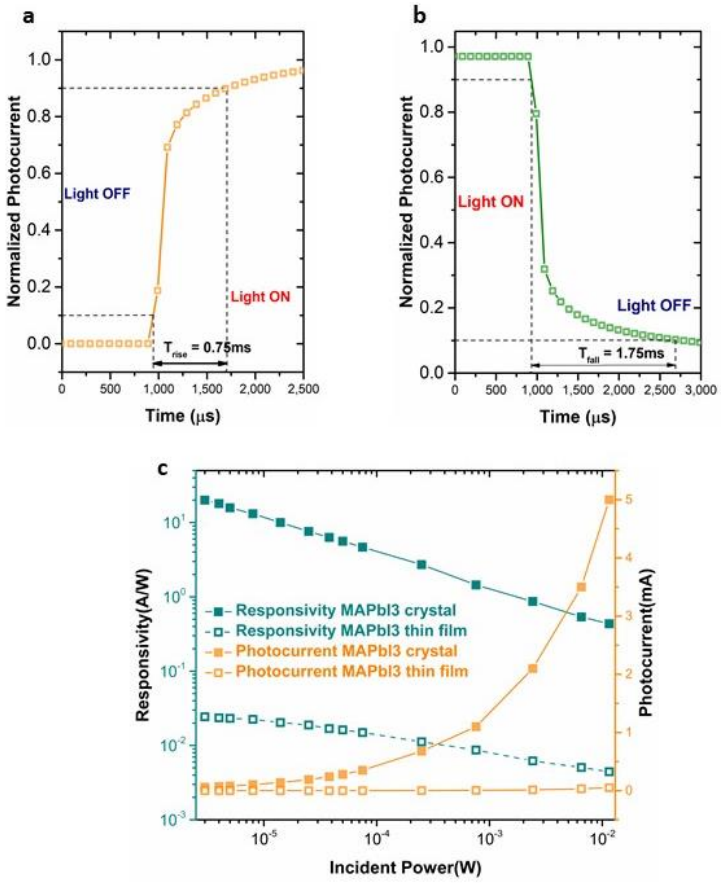

Figure 6.2: (a) Rise and fall time measurements for the S-AVC device when illuminated with a pulsed light source of power 2.4 mW and biased at 8 V, (b) Responsivity and photocurrent variation with varying incident light intensity.

Another figure of merit of the device, the detectivity (D^*), can be calculated from the responsivity as (by considering that the shot noise of the photodetector is significantly larger than the flicker and Johnson noise)

$$D^* = \frac{R}{\sqrt{2qJ_{dark}}} = R\sqrt{\frac{s}{2qI_{dark}}}$$

where J_{dark} is the dark current density of the device, I_{dark} is the corresponding dark current, and q is the electronic charge. The calculated detectivity was 1.48×10^{13} Jones, a very high detectivity reported for a $MAPbI_3$ photoconductor. Both detectivity and responsivity were measured for an illumination power of 3 μW. The low dark current due to a larger interelectrode spacing and a high responsivity owing to its superior crystallinity and absorption cross section resulted in this impressive detectivity.

Since crystal $MAPbI_3$ absorbs light in the entire visible spectrum and has a very high detectivity value (100 times larger than that of commercial Si photodetector), it can be considered as a promising candidate for low light imaging sensors. This indicates the nearly single-crystal-like quality of the crystals grown over the substrates. Since the photodetectors need to operate on continuously varying signals and must show excellent repeatability, the device was subjected to pulsed illuminations of wavelength 450 nm with different intensities (Figure 6.1b). The device yielded a decent on−off ratio of 1.4×10^3 for an incident power of 2.4 mW. The rise time and fall time of the device were calculated as 0.75 and 1.75 ms, respectively, as given in Figure 6.2a. The usage of an inert conducting oxide (FTO) as an electrode, a low electric field across the material, and a highly crystalline perovskite as a semiconductor yielded a highly stable and high sensitivity photoconductor photodetector (Figure 6.2c).

6.3 Spherulitic Crystals Based Photodetectors

On the same interdigitated FTO substrate, spherulitic crystals were grown from DMSO, as described in the previous chapter. In spherulitic crystal growth, the initial nucleation and crystal growth take place on the surface of substrates. The substrate surface provides the energy to overcome the nucleation barrier as explained before. Since these electrodes were laser etched, the substrate surfaces were highly rough. The corrugated nature of substrate surfaces due to interdigitated FTO electrodes and the high surface

roughness due to laser etching resulted in discontinuous growth of spherulitic crystals as shown in Appendix Figure A12.

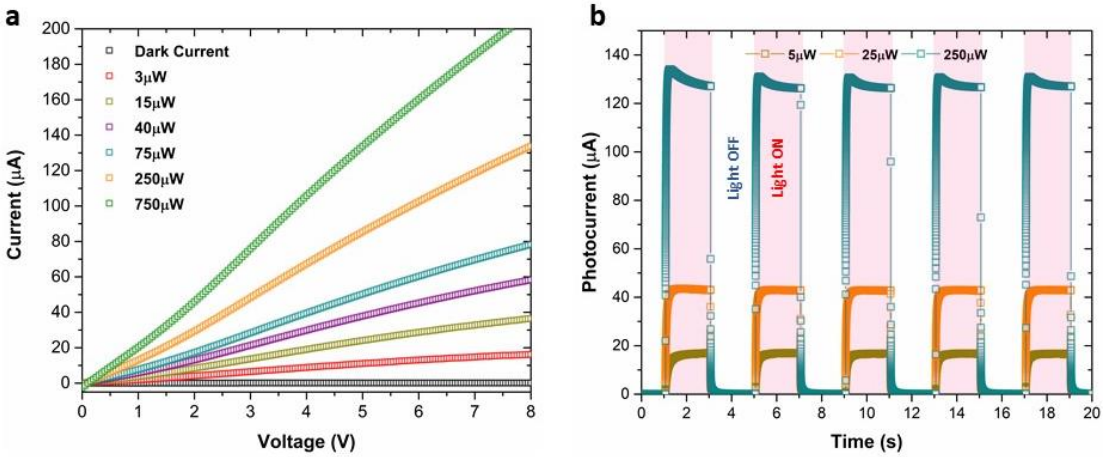

Figure 6.3: (a) I-V characteristics for various illumination powers, (b) Pulsed light characteristics for the spherulitic crystal based photodetector, for a biasing voltage of 8 V.

The current – voltage characteristics were measured for various illumination intensities as shown in Figure 6.3. The photocurrents were considerably lower than S-AVC based photoconductors. It has to be noted that the crystallinity of S-AVC crystals were significantly higher than the spherulitic crystals, which could probably be the reason for this higher photocurrent. The higher trap density measured in spherulitic crystals will also have an effect on the photocurrent generated. The responsivity for the devices were calculated as 5.6 AW^{-1}. The devices also showed a detectivity of 5.7×10^{12} Jones and an on-off ratio of 6.9×10^{2}.

6.4 The Role of Crystallinity and Morphology on Photodetector Characteristics

The photodetectors were fabricated employing S-AVC crystal films, spherulitic crystal films, dendritic films and standard thin films with anti-solvent dripping. The characteristics of these photodetectors were measured and the role of crystallinity as well as morphology were correlated to their device performances. The dark currents

were measured as shown in Figure 6.4. The measured dark current at a biasing voltage of 5 V are tabulated in Table 6.1.

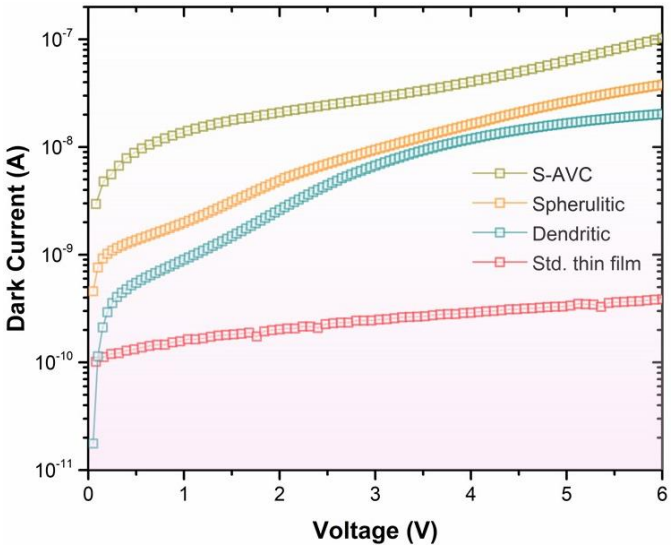

Figure 6.4: The photoconductor dark currents measured across the electrodes for different $MAPbI_3$ films.

Table 6.1: The device characteristics for the fabricated photoconductors.

	S-AVC film	**Spherulitic film**	**Dendritic film**	**Std. thin film**
Dark Current, 5V (nA)	60	27	17	0.34
Photocurrent, 750 µW, 5 V (µA)	1065	134	28	4
Responsivity (AW^{-1})	20	5.6	0.9	0.02
Detectivity (Jones)	1.48×10^{13}	5.7×10^{12}	1.9×10^{12}	3×10^{10}

S-AVC based devices had the highest dark current, whereas the standard thin film based devices were the ones with the lowest dark currents. Both these films had full coverage over the interdigitated electrode substrates. However, the thicknesses of S-AVC films were orders of magnitude higher than that of standard thin films. The

thicknesses of the films were of the order S-AVC film (100 µm) > spherulitic film (~1 µm) ≥ dendritic film (~1 µm) > standard thin films (400 nm). The difference in dark current could be possibly be due to the difference in thicknesses and the resultant reduction in resistance; or due to the increased number of grain boundaries which electrons may have to traverse between the electrodes. But the spherulitic and dendritic films (of thicknesses around 1 µm) also had dark currents at the same order of magnitude of that of S-AVC films, despite having an improper coverage over substrates. The slightly lower dark currents in spherulitic films could arise from the lack of proper coverage of these films due to their discontinuous growth, as explained in the previous section. This confirms that the increased number of grain boundaries resulted in lower dark currents in standard $MAPbI_3$ thin films and not from its lower thicknesses.

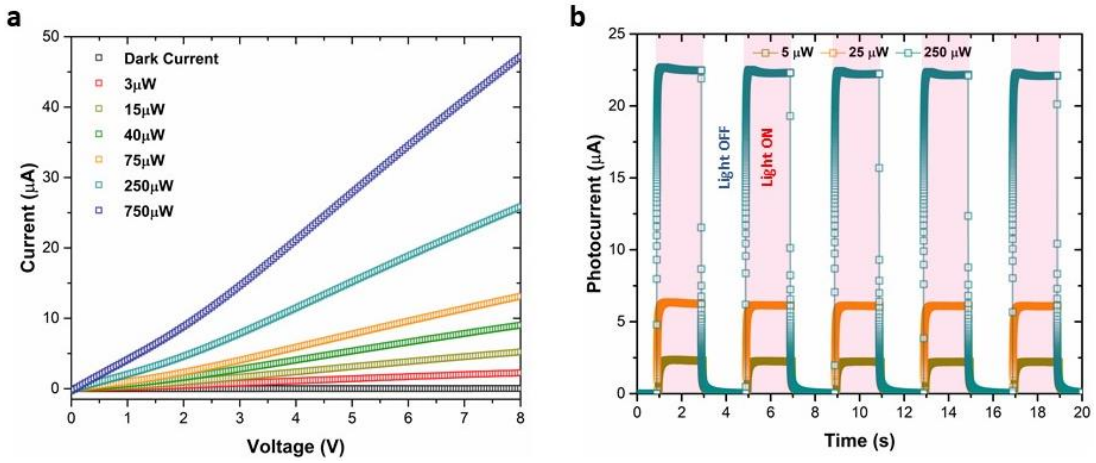

Figure 6.5: (a) I-V characteristics of dendritic photodetector for various illumination powers, (b) Pulsed light characteristics for dendritic film photodetectors, for a biasing voltage of 8 V.

A light source of wavelength 450 nm was used to illuminate the devices. The device characteristics for the dendritic and standard thin films are provided in Figure 6.5 and Figure 6.6, respectively. $MAPbI_3$ has a large absorption cross section for photons having energies beyond 1.6 eV. The calculated penetration depth is around 50 nm for an illumination of wavelength 450 nm (2.8 eV)[3]. Due to small penetration depth of light

at a wavelength of 450 nm, excess energy hot electron hole pairs close to the surface of perovskite layers are excited. The photocurrent is favored by the escape of charge carriers generated at the surface to the corresponding electrodes upon applying a biasing voltage.

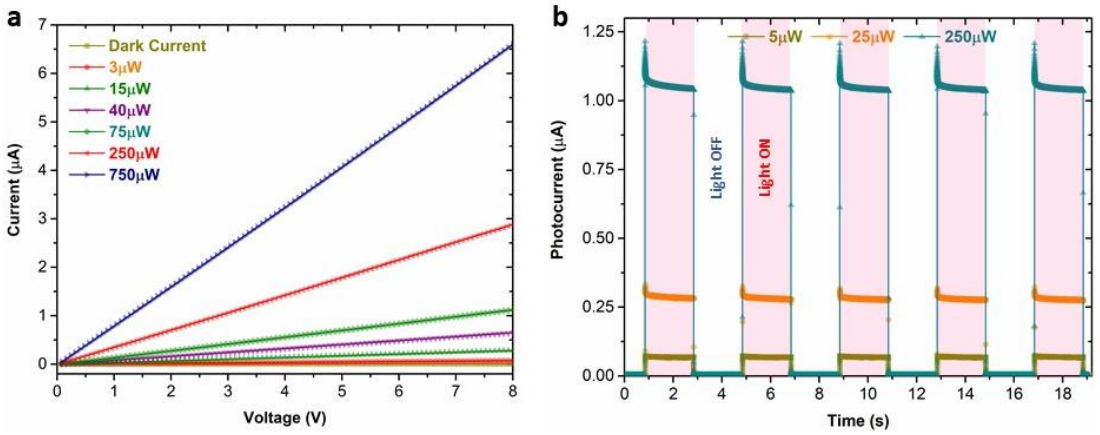

Figure 6.6: (a) I-V characteristics for a standard thin film photodetector for various illumination powers, (b) Pulsed light characteristics for standard $MAPbI_3$ thin film photodetectors, for a biasing voltage of 8 V.

Since the entire illuminated light gets fully absorbed in all these perovskites films, they should theoretically produce the same photocurrent. But the photocurrents were orders of magnitude different, when a S-AVC device was compared with a standard thin film one. The higher photocurrent in S-AVC can be attributed either to lower carrier recombination in the material or to a better charge transport between the electrodes, created by the reduction in grain boundary carrier scatterings, or to a combination of both. However, the ratio of photocurrents (at 750 μW illumination) to the dark currents for the devices biased at 5 V were significantly higher for S-AVC based devices, indicating a lower carrier recombination in the photo-absorber and its better crystallinity and optoelectronic quality. Since the crystal growth rate was significantly slower and the crystal grains had a symmetrical growth with lower lattice strains, the optoelectronic quality of S-AVC crystals should be superior when compared to other films.

6.5 Spherulitic Crystal based Photovoltaic Cells

As explained in the previous chapter S-AVC crystals were unsuitable for fabricating photovoltaic cells owing to their high thickness and surface roughness. Photovoltaic cells were fabricated using spherulitic crystals grown over electron transport layers. In the previous chapter it was found that spherulitic films were highly oriented along [200], [224] planes over FTO/SnO_2 and ITO/SnO_2 substrates. Since ITO substrates had smoother morphology as it was observed in the previous chapter, a device configuration of ITO/SnO_2/$MAPbI_3$/Spiro-OMeTAD/Au was used.

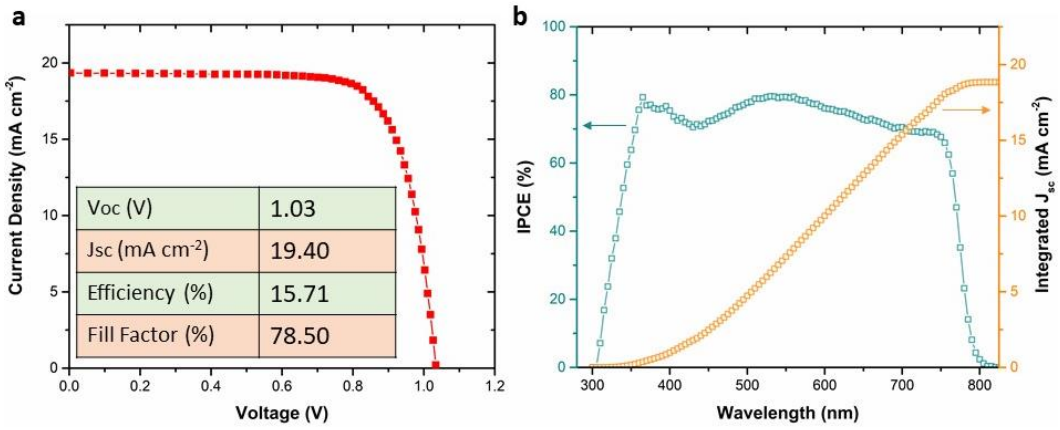

Figure 6.7: (a) Spherulitic crystal based champion cell characteristic (b) Internal power conversion efficiency and calculated integrated short circuit current for the device.

Table 6.2: Average photovoltaic cell characteristics of 10 spherulitic film based devices.

V_{oc} (V)	1.00 ± 0.03
J_{sc} (mAcm^{-2})	19.79 ± 0.40
Fill Factor (%)	76.53 ± 2.67
Efficiency (%)	15.15 ± 0.56

The devices yielded an open circuit voltage around 1 V and short circuit current densities above 19 mAcm^{-2} as shown in Figure 6.7. The champion cell in the lot

exhibited a photoconversion efficiency of 15.7 %. A batch of 10 devices had an average efficiency of 15.15 % with the device characteristics as shown in Table 6.2.

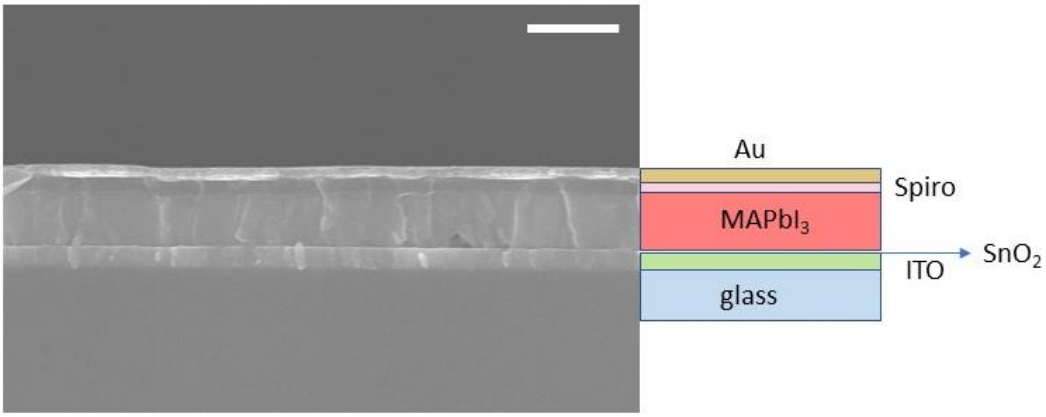

Figure 6.8: The device cross section of spherulitic crystal based photovoltaic cell (scale bar: 1 μm).

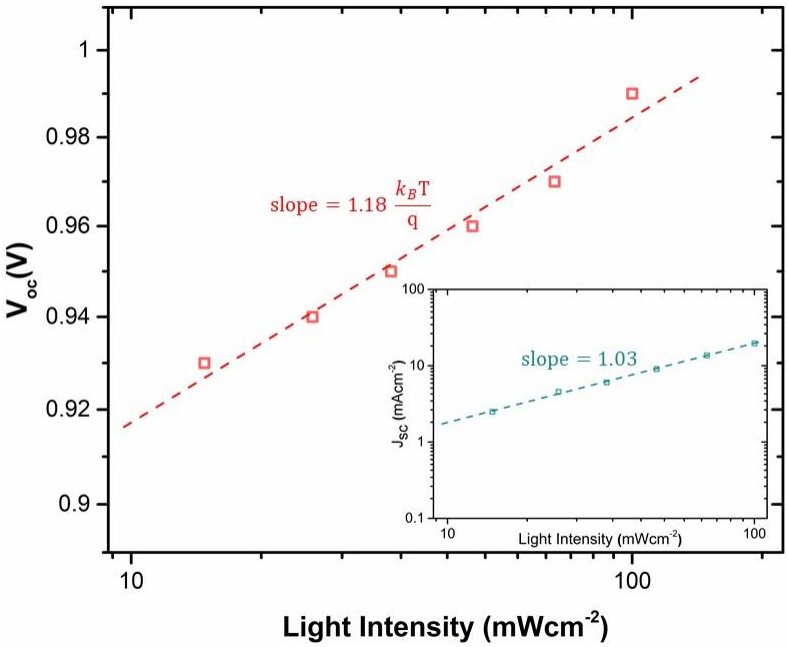

Figure 6.9: Light intensity – open circuit voltage plot of the solar cells and calculation of ideality factor. Light intensity - short circuit current density of the same device (inset)

The device cross section of the device was examined by SEM imaging. The images showed that the perovskite layer had an average thickness of around 700 nm. The perovskite layers had no horizontal grain boundaries for hampering the charge carrier transport as shown in Figure 6.8. The *V-I* characteristics of perovskite solar cells follow the diode equation. Ideality factor (*n*) measures how closely the photovoltaic cells follow the ideal diode equation. The slope of light intensity versus open circuit voltage (V_{oc}) plot can be used to extract the ideality factors, which provide information about the recombination mechanism present in the solar cells. An ideal diode has an ideality factor of 1, where just band to band radiative recombination prevails. As *n* approaches 2, trap assisted Shockley-Read-Hall (SRH) recombination dominates[4,5]. Hence ideality factor gives an information about the optoelectronic quality of the light absorber. The ideality factor measured for spherulitic cells was 1.18, indicating a superior optoelectronic quality of the material. The devices showed fill factors above 76 % and the V_{oc} of the devices were significantly lower than the band gap of the material. This indicates that there are recombination pathways present in the system other than the light absorber. As shown in the appendix Figure A13, the interface between SnO_2 – perovskite and perovskite – spiro were abysmal. As mentioned in the previous chapter, the thicknesses of the crystals were non uniform leading to poor device interfaces, thus contributing to the roll off in V_{oc} and fill factor. It is assumed that, improving interfaces between the layers is critical for enhancing the photovoltaic efficiencies of perovskite solar cells. Suitable interface optimizations for the spherulitic crystal films could probably enhance the device photoconversion efficiencies.

6.6 Ambient Stability of Spherulitic Crystal Based Devices

The ambient stability of S-AVC and spherulitic crystal films were investigated in previous chapters. Alike their films, S-AVC based photodetectors will have the same superior room ambient stability. But spherulitic film based photovoltaic cells are expected to show superior ambient stability as they have multiple device layers stacked above the perovskite films, which protect them from moisture exposure. As explained in the previous chapter, the simultaneous presence of O_2 and moisture accelerates the

degradation of $MAPbI_3$[6]. For perovskite solar cells it was found that the gold deposited as electrodes diffuses in through the hole transporter material and reacts with the perovskite thus degrading the device[7]. In presence of moisture, above 50 % RH, unencapsulated $MAPbI_3$ solar cells were observed to completely degrade within a few hundred hours of exposure[8]. The devices under investigation were unencapsulated and stored at 70 ± 3 % RH and 23 ± 2 ^oC. The devices were stored under dark conditions when they were not measured.

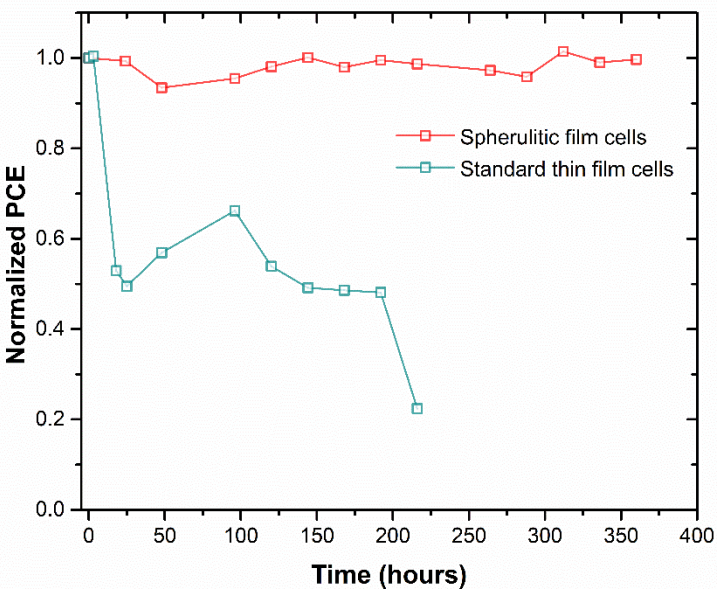

Figure 6.10: The normalized photoconversion efficiency variation of photovoltaic cells with time.

A batch of control standard thin film devices were fabricated along with the spherulitic film based devices for comparison. The spherulitic devices hardly show any drop in efficiencies even after 360 hours of storage in our extremely humid room ambience. However, the photoconversion efficiencies of control thin film devices were found to plummet to 50% of their initial values within 150 hours of fabrication as shown in Figure 6.10. In order to deeply understand the statistics of degradation, the device characteristics were plotted with respect to time as shown in Figure 6.11. After an initial drop in efficiency, the devices efficiencies were found to be improving slightly,

probably due to the doping of spiro in presence of O_2. The J_{sc} and fill factor were found to be improving, which indicates an enhancement in charge conduction through the devices. The V_{oc} of the devices were found to drop continuously, reflecting a slight degradation of perovskite absorber layer.

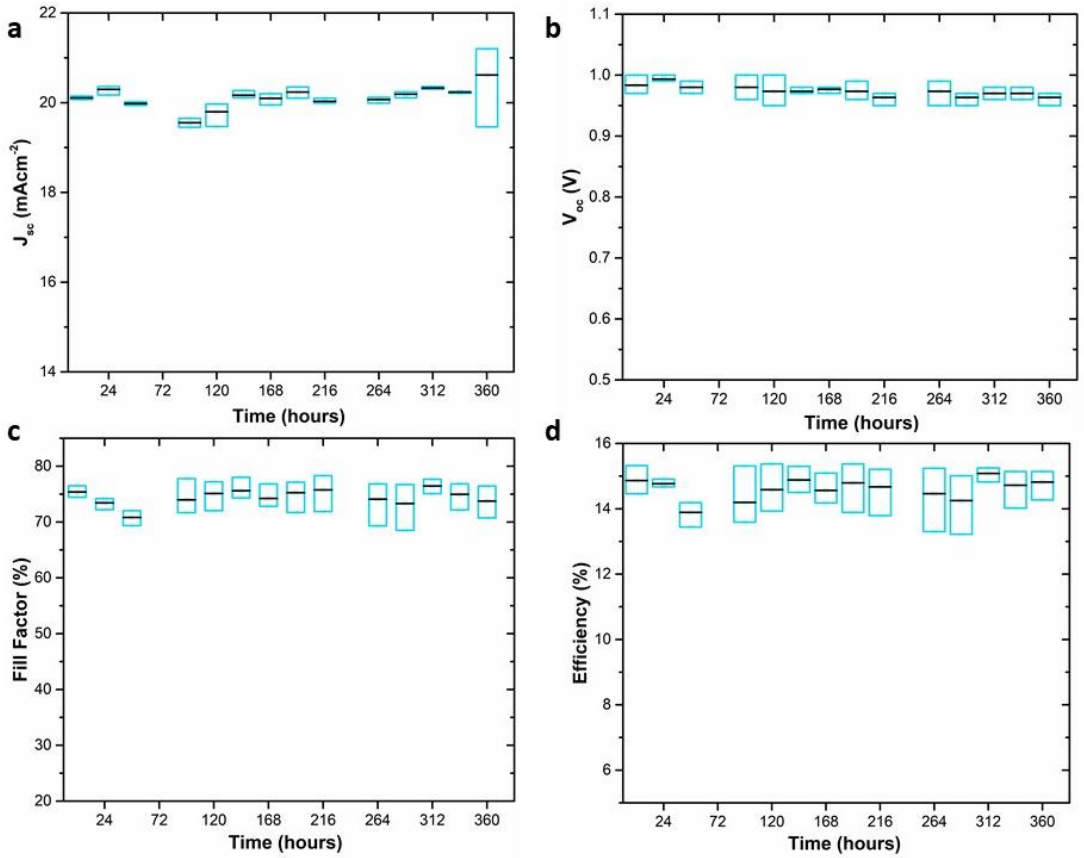

Figure 6.11: The variation of (a) short circuit current density, (b) open circuit voltage, (c) fill factor and (d) efficiency of spherulitic film based devices with time.

In short, it was evident that spherulitic crystal based devices showed a much superior ambient stability when compared to standard thin film devices.

6.7 The Role of Grain Boundaries in Ionic Conductance through $MAPbI_3$ Films

Oxide based perovskites are well known ionic conductors, where ionic transport is mediated by oxide ion vacancies, finding their application in fuel cells as solid electrolytes[9]. Later on, lead halide perovskites were found to belong to the class of

mixed ionic - electronic conductor owing to its high electronic and ionic conductivity[10,11]. Ionic migration through $MAPbI_3$ is often blamed as the reason behind hysteresis in photovoltaic *I-V* characteristics. It was claimed that a highly crystalline perovskite layer is found to produce reduced hysteresis in photovoltaic cells, thus providing an indirect claim over reduction in ionic migration[12]. However, the effect of grain boundaries on ionic transport through the material is still an unanswered question. Here, S-AVC, spherulitic and standard thin films were utilized for investigating the effect of crystallinity/grain boundaries over ionic transport through the material. The ionic conductance through the films were calculated using galvanostatic and impedance spectroscopy measurements.

6.7.1 Galvanostatic Measurements

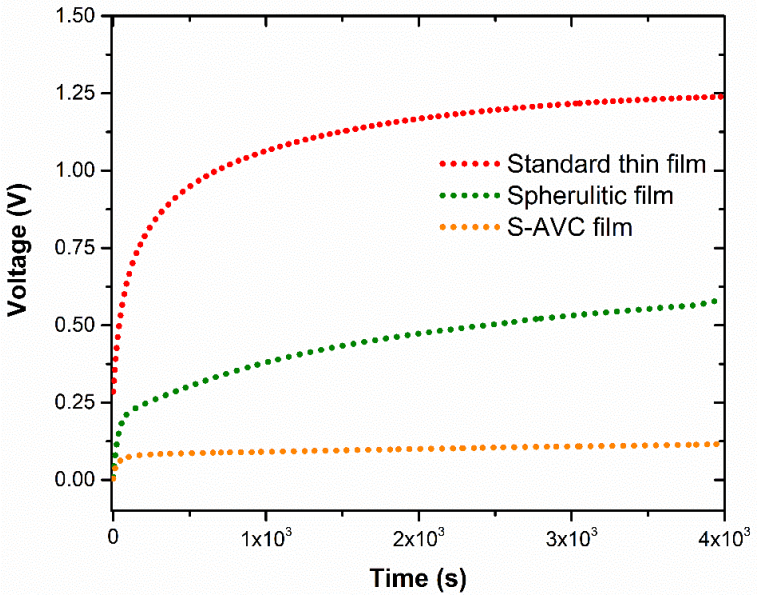

Figure 6.12: Galvanostatic measurements carried out by applying a constant current of 1 nA across different films.

Galvanostatic measurements used ion blocking ITO electrodes for applying a constant current of 1 nA through the different materials. As explained for the dark currents of photodetectors, the conductance through the materials are assumed to be only between electrodes, with negligible effects on the increased S-AVC film thicknesses. The initial

conductance is contributed by both ionic and electronic components ($\sigma_{initial} = \sigma_{ionic} + \sigma_{electronic}$). But as time elapses, the ions get accumulated at the blocking electrode - material interfaces and the conduction tends to be purely electronic ($\sigma_{final} = \sigma_{electronic}$). The voltages required to maintain the current through the material are measured to calculate the conductance as shown in Table 6.3.

Table 6.3: The calculated electronic and ionic conductivity of the three films form galvanostatic measurements.

	σ_{total} (S cm^{-1})	$\sigma_{electronic}$ (S cm^{-1})	σ_{ionic} (S cm^{-1})
Standard thin film	2.76 x 10^{-7}	6.31 x 10^{-8}	2.13 x 10^{-7}
Spherulitic film	4.83 x 10^{-6}	1.38 x 10^{-7}	4.69 x 10^{-6}
S-AVC film	1.95 x 10^{-5}	6.57 x 10^{-7}	1.88 x 10^{-5}

It was found that the S-AVC films with the least amount of grain boundaries offer the lowest ionic resistance for ionic conduction with $\sigma_{ionic} = 1.88 \times 10^{-5}\ S\ cm^{-1}$. The ionic conductivity of spherulitic films were an order higher at $4.69 \times 10^{-6}\ S\ cm^{-1}$. For the standard thin film, the ionic conductivity was one more order lower at $2.13 \times 10^{-7}\ S\ cm^{-1}$. These results show that $MAPbI_3$ is a good ionic conductor by itself and the grain boundaries have the ability to block the ionic motion through the film. It was also found that S-AVC films have higher electronic conductance owing to the lower carrier scattering at the inter-grain interfaces. It has to be noted that the electronic conductance of spherulitic films were an order of magnitude higher than standard thin films, even though they were of similar thicknesses, confirming our claim that the conductance improvement is due to the reduction in grain boundaries and not due to an increase in conduction cross section.

6.7.2 Impedance Spectroscopy Analysis

Impedance measurements were carried out using a potentiostat in two electrode configuration. The ions get blocked at the metal/electrode interfaces and form a parallel

plate capacitor combining the effects of both electrodes (C_i). The grain boundaries offer a resistance to the ionic motion, associated by a resistance R_{gb} and a capacitance C_{gb}, formed by the local ionic accumulation at the grain boundaries. Together with the two electrodes and the dielectric constant of the material, the circuit forms a capacitor C_{geom} in parallel to all the components. The material also offers a resistance R_e to the electron current through the material as shown in Figure 6.13d.

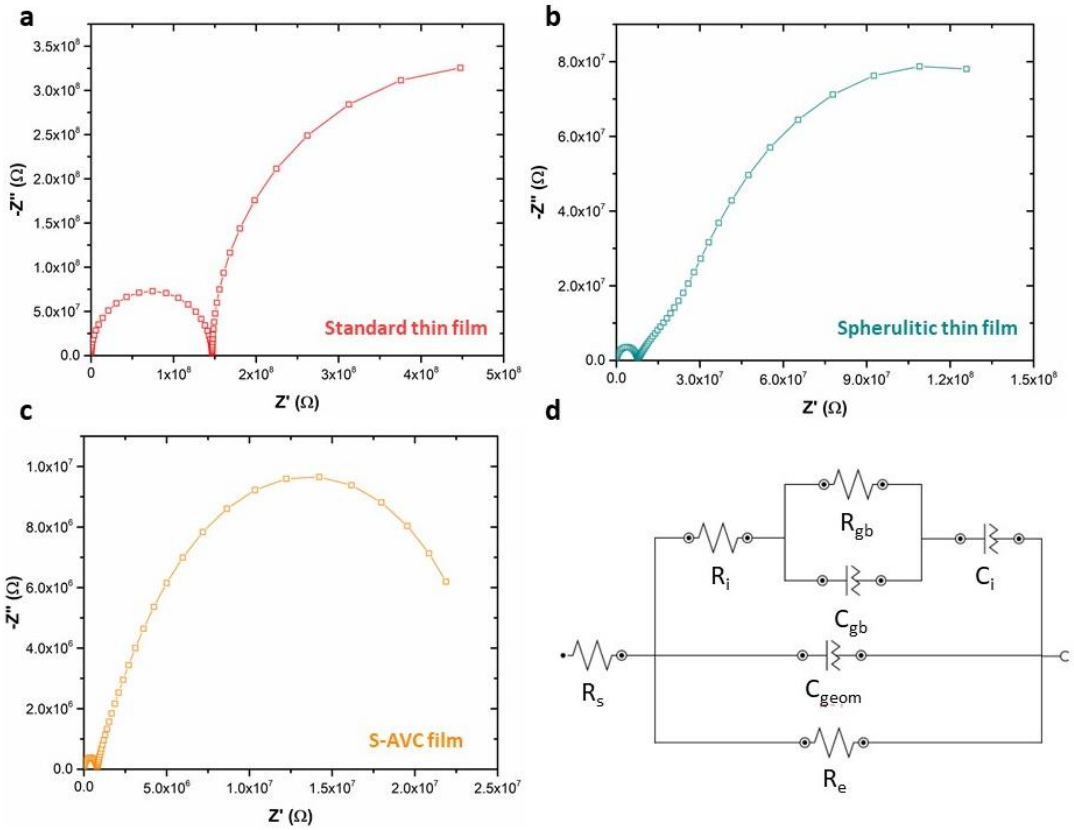

Figure 6.13: Nyquist plot for the lateral device composed of (a) standard thin films, (b) spherulitic thin film, (c) S-AVC film and (d) the corresponding equivalent circuit.

The combined ionic resistance ($R_i + R_{gb}$) was calculated from the Nyquist plot obtained from impedance measurements. the calculated ionic conductivity measured from the impedance spectroscopy is provided in Table 6.4. It was found that the ionic conductivity were of the same order as those obtained from galvanostatic measurements.

Table 6.4: The calculated ionic conductivity from the Nyquist plot.

	$R_i + R_{gb}$ (MΩ)	σ_{ionic} (S cm^{-1})
Standard thin film	180	4.38×10^{-7}
Spherulitic film	37.74	2.09×10^{-6}
S-AVC film	2.9	2.72×10^{-5}

Combining both these results, it was evident that S-AVC film shows the highest ionic and electronic conductance. The ionic conductance in $MAPbI_3$ were found to be resulting predominantly due to the motion of I^- ions and partially due to the movement of MA^+ cations. The mobile ions make use of vacancies created by the Frenkel defects for their movement[13,14]. As per the measurements here, the standard thin films where the probability of surface defects are higher showed the lowest ionic conductances. It gives us an evidence that the halide ion migrations can also take place through the interstitials due to their smaller dimensions and grain boundaries can hinder the motion of ions across the parallel electrodes.

6.8 Conclusion

Summing up, photoconductors using S-AVC, spherulitic and standard thin films were fabricated to study the effects of crystallinity on the photo-response of $MAPbI_3$. The higher photocurrent observed for S-AVC based devices arise from the combined effect of improved crystallinity and enhanced carrier conductance. The lower growth rate of S-AVC based crystals may have helped in the growth of superior quality crystal films. It was unable to fabricate vertical photovoltaic cells using S-AVC films owing to their high surface roughness and thickness. Photovoltaic cells were fabricated using spherulitic cells in vertical configuration. These photovoltaic cells had ideality factors closer to 1, thus elucidating the better optoelectronic quality of spherulitic $MAPbI_3$ films. The open circuit voltages of the devices were lower, probably due to poor device interfaces between the perovskite and charge extraction layers. The spherulitic film based devices had enhanced room ambient stability (at 70 ± 3 % RH and 23 ± 2 ^oC)

when compared to standard thin film devices. Hence improving the crystallinity of $MAPbI_3$ layer can be used as an alternate strategy to enhance the ambient stability of these photovoltaic cells. These films with various levels of crystallinity were used to examine the role of grain boundaries on the ionic conductance through the material. It was found that the highly crystalline S-AVC and spherulitic films had higher ionic and electronic conductance. This indicates that grain boundaries act as barriers for ionic and electronic conduction. It was recently reported that interfaces of devices get altered by space charge zones created due to ionic migration and accumulation[15]. These results demonstrate that, for thin film based photovoltaic technologies like lead halide perovskites, the device interfaces play a vital role in photoconversion efficiencies and device characteristics.

6.9 References

1. Taşçioğlu, A., Taşkin, O. & Vardar, A. A Power Case Study for Monocrystalline and Polycrystalline Solar Panels in Bursa City, Turkey. *Int. J. Photoenergy* **2016**, 7324138 (2016).

2. Cheng, X., Yang, S., Cao, B., Tao, X. & Chen, Z. Single Crystal Perovskite Solar Cells: Development and Perspectives. *Adv. Funct. Mater.* **30**, 1–20 (2020).

3. Yang, Y. *et al.* Top and bottom surfaces limit carrier lifetime in lead iodide perovskite films. *Nat. Energy* **2**, 16207 (2017).

4. Sherkar, T. S. *et al.* Recombination in Perovskite Solar Cells: Significance of Grain Boundaries, Interface Traps, and Defect Ions. *ACS Energy Lett.* **2**, 1214–1222 (2017).

5. Zhu, C. *et al.* Strain engineering in perovskite solar cells and its impacts on carrier dynamics. *Nat. Commun.* **10**, 815 (2019).

6. Ahn, N. *et al.* Trapped charge-driven degradation of perovskite solar cells. *Nat. Commun.* **7**, 1–9 (2016).

7. Domanski, K. *et al.* Not All That Glitters Is Gold: Metal-Migration-Induced

Degradation in Perovskite Solar Cells. *ACS Nano* **10**, 6306–6314 (2016).

8. Yang, J., Siempelkamp, B. D., Liu, D. & Kelly, T. L. Investigation of $CH_3NH_3PbI_3$ degradation rates and mechanisms in controlled humidity environments using in situ techniques. *ACS Nano* **9**, 1955–1963 (2015).

9. Takahashi, T. & Iwahara, H. Ionic conduction in perovskite-type oxide solid solution and its application to the solid electrolyte fuel cell. *Energy Convers.* **11**, 105–111 (1971).

10. Mizusaki, J., Arai, K. & Fueki, K. Ionic conduction of the perovskite-type halides. *Solid State Ionics* **11**, 203–211 (1983).

11. Tress, W. Metal Halide Perovskites as Mixed Electronic-Ionic Conductors: Challenges and Opportunities - From Hysteresis to Memristivity. *J. Phys. Chem. Lett.* **8**, 3106–3114 (2017).

12. Lee, J. W., Kim, S. G., Yang, J. M., Yang, Y. & Park, N. G. Verification and mitigation of ion migration in perovskite solar cells. *APL Mater.* **7**, 041111 (2019).

13. Eames, C. *et al.* Ionic transport in hybrid lead iodide perovskite solar cells. *Nat. Commun.* **6**, 2–9 (2015).

14. Futscher, M. H. *et al.* Quantification of ion migration in $CH_3NH_3PbI_3$ perovskite solar cells by transient capacitance measurements. *Mater. Horizons* **6**, 1497–1503 (2019).

15. Kim, G. Y., Senocrate, A., Moia, D. & Maier, J. Ionically Generated Built-In Equilibrium Space Charge Zones—a Paradigm Change for Lead Halide Perovskite Interfaces. *Adv. Funct. Mater.* **30**, 1–9 (2020).

Chapter 7

Conclusion and Future Work

This chapter gives a general conclusion for the thesis elucidating the research contributions in a nutshell. The results obtained are correlated with the thesis objectives discussed in chapter 1. This chapter also introduces the possible future works that can be carried out based on this thesis.

7.1 Summary and Discussion

In this thesis, techniques were developed to grow highly crystalline layers of lead halide perovskites over device substrates. As lead halide perovskites are crystallized directly from their precursors, our work was instigated by the investigation of the nature of precursors. Our meticulous study on the nature of crystallization as well as precursors helped us to develop two techniques to grow highly crystalline layers of $MAPbBr_3$ and $MAPbI_3$. Our project on the crystallization of lead halide perovskites lead us to the following exciting perceptions.

Perovskite precursors and selection of solvents for crystallization: The investigations on the nature of precursors in Chapter 4 and 5 revealed their chemical and colloidal characteristics. The colloidal dimensions were of the order of micrometers (at 0.05 M), comparable to the previous reports[1]. The chemical nature of $MAPbI_3$ precursors was found to be different in DMSO, with the precursors forming $[PbI]^+$ plumbates. In GBL, DMF and ACN the precursors existed as a combination of $[PbI]^+$, $[PbI_2]$ and $[PbI_3]^-$ which could have significant effects on the crystallization processes. It was found that GBL is the best solvent for crystallization of $MAPbI_3$ by anti-solvent vapor crystallization (AVC) due to its lower co-ordination ability and significant dissolution capability of precursors. For $MAPbBr_3$ DMF and DMSO can work as efficient solvents with dichloromethane used as the anti-solvent in both cases. In highly co-ordinating solvents like DMF and DMSO, $MAPbI_3$ crystallizes as solvent composites on anti-solvent percolation. The crystallization mechanism of $MAPbBr_3$ and $MAPbI_3$ by anti-solvent vapor diffusion to the precursors was investigated for the first time. It was observed that the surfaces of crystallization dishes aid to overcome the nucleation barrier by providing sites for heterogenous nucleation. It was vindicated that the crystallization and crystal growth can be altered by varying the surface energies of crystallization dishes.

Sonication modified anti-solvent vapor crystallization (S-AVC): Ultrasonication can be used to induce homogenously nucleated seed crystals in the precursor at supersaturation, after anti-solvent percolation in AVC. The homogeneously nucleated seed crystals grow on the device substrates dipped in the precursor in the crystallization

dish. The crystallization was slow (similar to AVC) and took almost 3 days for completion. The films grown were highly crystalline and showed very sharp diffraction peaks, comparable to monocrystalline XRD peaks reported previously[2]. The trap densities measured for the S-AVC grown crystals were of the order of 10^{11} cm^{-3}, just an order of magnitude higher than the previously reported values for their high quality monocrystals[3]. The films also showed redshifted absorption onsets and photoluminescence peak, a typical characteristic of lead halide perovskite monocrystals[4,5]. The films had an average grain size of a few hundred micrometers and were well packed over substrates. Even though the films were of good material quality some of their characteristics hampered their efficient optoelectronic device applications. The thickness of the $MAPbI_3$ films deposited were above 100 µm, for full coverage over substrates, which was too high for photovoltaic applications. The film surfaces were highly rough and irregular thus impeding the atop fabrication of devices. In S-AVC the initial nucleation and growth of crystals take place in the precursor bulk, away from substrates kept in the crystallization dish. The nucleated seed crystals get deposited on the substrate surfaces and as more anti-solvents percolate inside, the seed crystals grow over these surfaces. Since the growth over the substrates were symmetric along all dimensions, the films had poor thickness-coverage controllability.

Spherulitic crystallization by confining nucleation and growth on substrate surfaces: One of the most attractive attributes of lead halide perovskites is their facile solution processability. Perovskite films of good crystallinity can be deposited by thin film deposition processes like spin coating. Spin coating process was modified to grow highly crystalline films of spherulitic grains on device substrates. Confining the nucleation sites on substrate surfaces while spin coating gave rise to improved surface coverage. The heterogeneous nucleation and growth on substrate surfaces resulted in the growth of large aspect ratio grains. The highly coordinating solvent DMSO was found to work as an efficient solvent to reduce homogeneous nucleation while spinning of precursors. The Urbach energy and trap densities measured for $MAPbI_3$ spherulitic crystal films were significantly lower than normal thin films, indicating their superior optoelectronic quality. The spherulitic films showed a high degree of orientation on the substrate surface, with [200], [224] plane growing vertically out of the substrate

surfaces. The orientation of the films was justified by *X*-ray pole figure and electron backscatter diffraction (EBSD) analysis. EBSD revealed that the films had a fiber like texture centered along [200], [224] planes. Since highly oriented crystal growth was obtained by facile spin coating process and thin crystalline films of good coverage were grown, vertical optoelectronic devices like photovoltaic cells were fabricated employing them. Since the initial nucleation and crystal growth were exclusively on substrate surfaces, it was found that the surface of substrates plays a vital role on the morphology and coverage of spherulitic thin films.

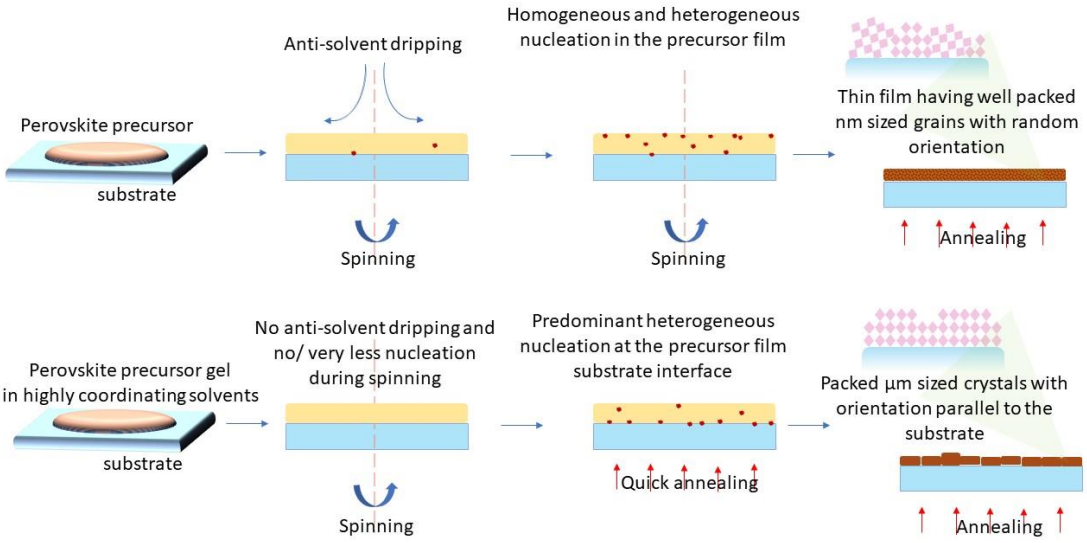

Figure 7.1: Schematic showing the growth of spherulitic thin film of $MAPbI_3$ by modifying spin coating process.

Optoelectronic device fabrication employing the crystal films: $MAPbI_3$ crystal films were used to fabricate optoelectronic devices like photodetectors and photovoltaic cells. Since the thickness of S-AVC films were high, planar photodetectors were fabricated by growing $MAPbI_3$ crystals over pre-patterned FTO interdigitated electrodes over glass. The photodetectors were bottom illuminated by a 450 nm source, the devices yielded a high responsivity of 20 AW^{-1} and a detectivity of 1.48 x 10^{13} Jones. The responsivity and detectivity of the crystal based devices were orders of magnitude higher than that of a standard thin film device, indicating the role of

crystallinity and grain boundaries on photodetector performances. Since the thickness of S-AVC films were higher than 100 µm, the films cannot be used for fabricating photovoltaic cells. Photoconductors fabricated using spherulitic $MAPbI_3$ films exhibited inferior optoelectronic characteristics when compared to S-AVC based devices, due to inferior material properties and improper film coverage over the prepatterned interdigitated electrode substrates. Since spherulitic $MAPbI_3$ film were thickness controllable, vertical photovoltaic cells with n-i-p architecture were fabricated. The photovoltaic cells had ITO/SnO_2/$MAPbI_3$/Spiro/Au configuration. The spherulitic films grown over SnO_2 layers were well packed and oriented along [200], [224] planes. The photovoltaic cells fabricated had an average photoconversion efficiency above 15 %. The devices had ideality factors closer to 1, indicating the superior optoelectronic quality of the films but had a significant roll off in open circuit voltages. This indicates the critical role of interfaces in thin film photovoltaic technologies like lead halide perovskites.

Relationship between crystallinity, ambient stability and ionic conductance: Since the films grown were of varying crystallinity, they were used to study the role of grain boundaries on ambient stability and ionic conductance of the material. Potentiostatic as well as impedance measurements were carried out to study the ionic conductivity through the crystal films and are compared to that of standard spin coated thin films. It was found that ionic and electronic conductance of perovskite films increase with enhancement in crystallinity and they are good mixed ionic electronic conductors. The role of grain boundaries on the ambient stability of the material were also investigated using S-AVC and spherulitic crystal films. The S-AVC and spherulitic films showed superior stability at 23 ± 2 ^oC and 70 ± 3 % relative humidity. This confirms the previous research results that grain boundaries act as pathways for moisture intercalation and ambient instability of the material[6]. It was found that spherulitic crystal based photovoltaic cells had excellent room ambient stability when compared to normal thin film devices. Hence improving the crystallinity of perovskite films can be implemented as an effective strategy to enhance the ambient stability of their optoelectronic devices, thereby taking it another step forward towards its commercialization.

Table 7.1: Comparison of the key attributes for the two crystal film deposition methods

S-AVC crystal growth	Spherulitic crystal growth
Modified AVC	Modified spin coating process
Substrate surface independent nucleation and growth	Crystallization process is highly dependent on substrate surfaces
Crystallization process takes 2-3 days for completion	Crystallization take place in a few seconds
$MAPbI_3$ and $MAPbBr_3$ films require a thickness above 100 μm for full substrate coverage	Possible to make $MAPbI_3$ films with thicknesses lesser than 1 μm with full substrate coverage. $MAPbBr_3$ did not form a pinhole free film.
Unable to fabricate vertical optoelectronic devices like photovoltaic cells.	Vertical as well as planar devices were fabricated.
Trap density of the order of 10^{11} cm^{-3}	Trap density of the order of 10^{12} cm^{-3}
Superior for photodetectors	Better for fabricating photovoltaic cells

Concluding the work in a nutshell, two crystallization techniques were developed to grow perovskite crystalline films over substrates. S-AVC method was developed by modifying anti-solvent vapor crystallization by employing a short ultrasound pulse to induce nucleation at deep supersaturation. The initial nucleation and crystal growth take place in the precursor bulk, away from the substrate surface. $MAPbI_3$ and $MAPbBr_3$ films grown by S-AVC technique had thicknesses above 100 μm for full substrate coverage. Spherulitic crystallization was developed as a modification of spin coating process, where the solvent co-ordination and crystallization kinetics are tuned

to induce heterogeneous nucleation on the substrate surface. $MAPbI_3$ films grown by spherulitic crystallization can be thickness tuned, with possible thicknesses even lesser than 1 μm with full substrate coverage. However, $MAPbBr_3$ films grown by spherulitic crystallization were unable to form pinhole free films. It was unable to fabricate vertical optoelectronic devices employing S-AVC films due to their excessive thickness and surface roughness. At the same time, spherulitic films were utilized to fabricate vertical photovoltaic cells. The planar photodetectors fabricated using S-AVC crystal film showed better performances when compared to spherulitic films owing to their superior optoelectronic quality and coverage over prepatterned substrates. The crystal films fabricated were used to measure the ionic conductance thereby revealing the effect of grain boundaries on ionic transport. It was found that ionic transport through the perovskite film are impeded by the presence of grain boundaries. A brief comparison on the key characteristics of S-AVC and spherulitic crystal film are provided in Table 7.1.

7.2 Future Work

The thesis on inducing crystal growth on substrates opens up the following avenues for future research.

7.2.1 Epitaxial Growth of Lead Halide Perovskites

Conventional electronic and optoelectronic devices use a highly crystalline and crystallographically oriented thin film of semiconducting materials as constituent layers. These layers of semiconductors are grown on lattice matched substrates and are termed as epitaxial films. During the course of this work, a few works on epitaxial growth of lead halide perovskites were reported. $MAPbI_3$ crystals grown over KCl [001] single crystals by spin coating showed a preferred out of plane orientation along [110] direction[7]. Later on, other hetero-epitaxial layers of $CsPbBr_3$ were grown on strontium titanate (STO) [100] substrates by vapor phase epitaxy and simple spin coating processes[8,9]. Vapor phase epitaxy was used to achieve orthorhombic $CsPbBr_3$ epitaxial growth over ZnSe [100][10].

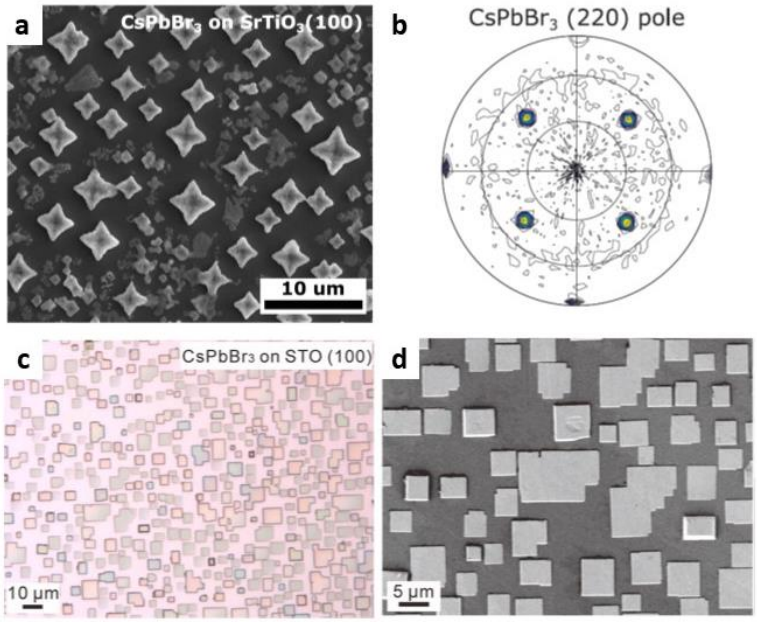

Figure 7.2: (a) $CsPbBr_3$ epitaxial crystals grown on STO [100] substrate by spin coating process and its (b) in-plane pole figure of [220] plane, (c) and (d) $CsPbBr_3$ epitaxial crystals grown on STO [100] substrate by chemical vapor deposition[8,9]

However, all these films were discontinuous and were formed as discreet crystal islands of sizes typically around hundred microns. The discontinuity of these films makes it inappropriate to fabricate scaled up optoelectronic devices. Employing highly crystalline and continuous epitaxial layers of lead halide perovskites in optoelectronic devices is expected to significantly improve the device characteristics. However, for devices like photovoltaic cells, the underlying electron and hole transporting layers (which act as substrates during crystallization) are amorphous (or less crystalline). Using liquid phase epitaxy, it was demonstrated that single crystals of metals like gold can be grown on amorphous silicon by varying the crystallization kinetics[11]. Semiconductors like CdTe were grown over amorphous SiO_2/Si [100] substrates by employing graphene sheets as intermediate layers[12]. Oxide semiconductors like TiO_2 were grown over glass substrates by using $Ca_2Nb_3O_{10}$ nanosheets as seed crystals[13]. All these works demonstrate that an 'epitaxial like' growth of lead halide perovskites over amorphous electron or hole injection layers are possible by carefully manipulating the crystallization process. Suitable interfacial layers and seed crystals can be utilized to

induce epitaxial growth of lead halide perovskites as it was executed in the above-mentioned works. A pinhole free, epitaxial layer of perovskites can be utilized for fabricating various optoelectronic devices from phototransistors to photovoltaic cells.

7.2.2 Exploration of Fundamental Optoelectronic Properties

The optoelectronic properties and optical characteristics of lead halide perovskites are highly dependent on material processing and measurement techniques involved. For instance, the reported charge carrier mobility of $MAPbI_3$ varies from 1.1 $cm^2V^{-1}s^{-1}$ when measured by PL quenching methods to 600 $cm^2V^{-1}s^{-1}$ when measured using optical pump – THz probe photoconductivity measurements[14]. As lead halide perovskite technologies grow mature, it is high time now to reach a consensus on the material's fundamental optical and electronic characteristics.

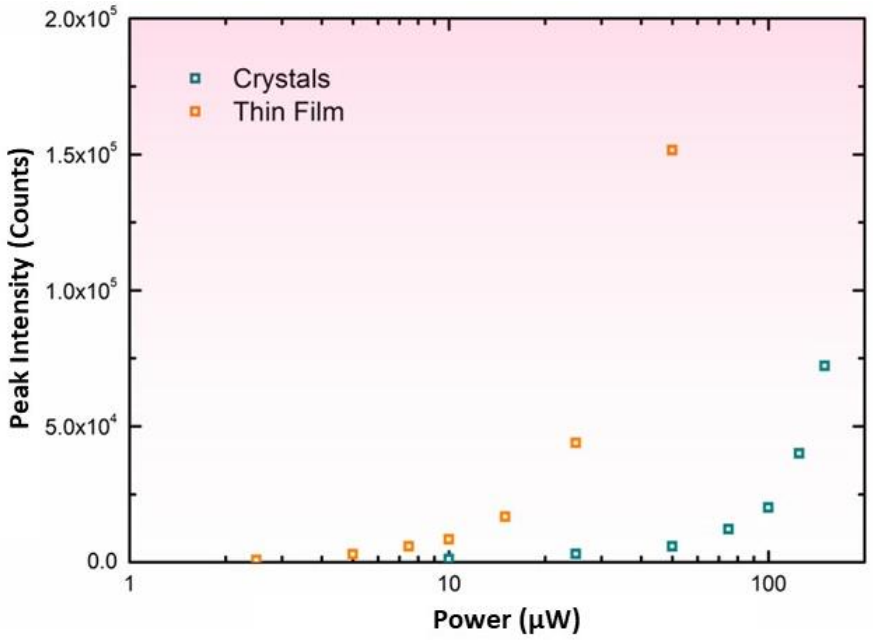

Figure 7.3: Dependence of the photoluminescence peak intensity on excitation power (λ_{exc} = 450 nm).

During this project it was noticed that single crystals of lead halide perovskites show significantly lower photoluminescence intensities when compared to their thin film

counterparts as shown in Figure 7.3. There are contradictory reports regarding the photoluminescence of lead halide perovskite crystals and thin films. In single crystals it was demonstrated that the photoluminescence arises from the crystal surfaces and photoluminescence quenching takes place by diffusion of photogenerated electrons and holes to the crystal bulk. The electron hole pairs undergo repeated recycling between photons and electron hole pairs through multiple absorption-diffusion-emission processes. In highly crystalline perovskites the diffusion and reabsorption processes are more efficient and will show lower photoluminescence[15,16]. However, it is counterintuitive to the fact that a good light absorber material will have an illustrious photoluminescence, and in many works, higher photoluminescence intensities are projected to show the optoelectronic quality of the perovskite layers. An intensive research on the mechanism of light absorption-emission and excited state dynamics will be intriguing to examine the photo-assisted processes in the material. The high absorption cross section in thick single crystals of these materials limits the conventional transmission based optical measurements[17]. Spherulitic crystals grown in this work can be utilized to study optical processes in these materials in transmission domain. S-AVC and spherulitic crystals have optoelectronic qualities that are comparable to single crystals and are substrate integrated, which makes the optical and electrical measurements amiable.

7.2.3 S-AVC Based High Energy Radiation Detectors

Lead based halide perovskites can work efficiently as *X*-ray and γ-ray detectors due to their high radiation stopping power, large mobility-lifetime (μT) product, their defect tolerant nature and facile single crystal growth techniques. Conventional semiconductor *X*-ray detectors use materials like amorphous Si, amorphous Se, HgI_2 and $Cd_{1-x}Zn_xTe$ ($x < 0.2$). Recent reports show that lead halide perovskites like $MAPbI_3$ and $MAPbBr_3$ can be utilized to fabricate highly sensitive *X*-ray detectors[18–20]. The environmental instability of lead halide perovskites will not hinder their application in *X*-ray detectors as they will be tightly contained with suitable encapsulants.

Table 7.2: Comparison of characteristics of lead halide perovskites to conventional *X*-ray detector materials.

	Band-gap (eV)	**Atomic number**	**μT (cm^2V^{-1})**	**Sensitivity ($\mu C Gy_{air}^{-1} cm^{-2}$)**
a-Si	1.2	14	>1	8
a-Se	1.85	34	10^{-7}	20
HgI_2	2.13	80, 53	10^{-4}	1600
$Cd_{1-x}Zn_xTe$	1.4 – 2.2	48, 52	0.01	318
$MAPbBr_3$	2.33	82, 35	0.012	2.1×10^4
$MAPbI_3$	1.57	82, 53	0.010	1.1×10^4

The thickness of perovskite absorbers required for *X*-ray detection is significantly larger than the ones that can be attained by standard thin film deposition processes. Hence perovskite single crystals are normally used for *X*-ray detection. However, the attainable lateral dimensions of the perovskite single crystals are of the order of a few centimeters, that makes it inappropriate to be used in large scale imaging applications. The S-AVC crystals demonstrated in this work can be grown over large areas and on flexible as well as rigid substrates. The thicknesses of S-AVC films can be larger than 100 μm, thus providing enough stopping distance and can be utilized to fabricate *X*-ray detectors. Since the S-AVC films are composed of individual crystallites, the films will have higher electrical resistance than their corresponding monocrystals. Thus S-AVC crystals grown over substrates have the potential to be forged into potent *X*-ray detectors.

7.2.4 Role of Perovskite Crystallinity and Orientation on Photovoltaic Cell Characteristics

Lead halide perovskite are known for their inherent defect tolerance as explained in Chapter 2. Improving the crystallinity of perovskite absorbers is expected to enhance the photovoltaic performances. However, monocrystalline perovskite solar cells

reported so far in the literatures lag behind polycrystalline cells in terms of efficiencies[21]. Monocrystalline cells fabricated so far had a maximum active area of 2 mm^2 and are unable to scale up to an area of 9 mm^2, commonly utilized to report the standard cell efficiencies. In perovskite solar cells it was found that the top and bottom surfaces of the perovskite layer were found to be the sources of recombination[17]. Hence the interfaces and surfaces of the layers are expected to play a crucial role in determining the device efficiencies. It was also elucidated that grain size and crystal orientation don't determine the optoelectronic properties of $MAPbI_3$ perovskite[22]. All these works were carried out on perovskite films and not on complete photovoltaic cells. Spherulitic films demonstrated in this work are of high crystallinity and orientation and can be utilized with different interfaces to determine the effects of interfaces on device performances. Crystallographically oriented spherulitic films with grain sizes a thousand times larger than conventional spin coated thin films can be used to answer the following two long standing queries of the perovskite photovoltaics community: (a) Do monocrystalline perovskite films help to push the device efficiencies towards the thermodynamic limit? (b) How crystallinity and crystalline orientation affect the photovoltaic cell characteristics?

7.3 References

1. Yan, K. *et al.* Hybrid Halide Perovskite Solar Cell Precursors: Colloidal Chemistry and Coordination Engineering behind Device Processing for High Efficiency. *J. Am. Chem. Soc.* **137**, 4460–4468 (2015).

2. Peng, W. *et al.* Solution-Grown Monocrystalline Hybrid Perovskite Films for Hole-Transporter-Free Solar Cells. *Adv. Mater.* **28**, 3383–3390 (2016).

3. Shi, D. *et al.* Low trap-state density and long carrier diffusion in organolead trihalide perovskite single crystals. *Science.* **347**, 519–522 (2015).

4. Yamada, T., Yamada, Y., Nakaike, Y., Wakamiya, A. & Kanemitsu, Y. Photon Emission and Reabsorption Processes in $CH_3NH_3PbBr_3$ Single Crystals Revealed by Time-Resolved Two-Photon-Excitation Photoluminescence Microscopy.

Phys. Rev. Appl. **7**, 1–8 (2017).

5. Wu, B. *et al.* Discerning the Surface and Bulk Recombination Kinetics of Organic–Inorganic Halide Perovskite Single Crystals. *Adv. Energy Mater.* **6**, 1–9 (2016).

6. Wang, Q. *et al.* Scaling behavior of moisture-induced grain degradation in polycrystalline hybrid perovskite thin films. *Energy Environ. Sci.* **10**, 516–522 (2017).

7. Ji, L., Hsu, H. Y., Lee, J. C., Bard, A. J. & Yu, E. T. High-Performance Photodetectors Based on Solution-Processed Epitaxial Grown Hybrid Halide Perovskites. *Nano Lett.* **18**, 994–1000 (2018).

8. Chang, J. Spin Coating Epitaxial Films. *Cailiao Daobao/Materials Reports* **33**, 1919–1920 (2019).

9. Chen, J. *et al.* Single-Crystal Thin Films of Cesium Lead Bromide Perovskite Epitaxially Grown on Metal Oxide Perovskite (SrTiO3). *J. Am. Chem. Soc.* **139**, 13525–13532 (2017).

10. Wang, Y. *et al.* Epitaxial Growth of Large-Scale Orthorhombic $CsPbBr_3$ Perovskite Thin Films with Anisotropic Photoresponse Property. *Adv. Funct. Mater.* **29**, 1–9 (2019).

11. Zhang, K. *et al.* Single-crystal metal growth on amorphous insulating substrates. *Proc. Natl. Acad. Sci. U. S. A.* **115**, 685–689 (2018).

12. Mohanty, D. *et al.* Growth of epitaxial CdTe thin films on amorphous substrates using single crystal graphene buffer. *Carbon N. Y.* **144**, 519–524 (2019).

13. Taira, K. *et al.* Lateral solid-phase epitaxy of oxide thin films on glass substrate seeded with oxide nanosheets. *ACS Nano* **8**, 6145–6150 (2014).

14. Herz, L. M. Charge-Carrier Mobilities in Metal Halide Perovskites: Fundamental Mechanisms and Limits. *ACS Energy Lett.* **2**, 1539–1548 (2017).

15. Alsari, M. *et al.* Photon recycling in lead iodide perovskite solar cells. *Science.*

351, 1430–1433 (2016).

16. Yamada, Y. *et al.* Dynamic Optical Properties of $CH_3NH_3PbI_3$ Single Crystals As Revealed by One- and Two-Photon Excited Photoluminescence Measurements. *J. Am. Chem. Soc.* **137**, 10456–10459 (2015).

17. Yang, Y. *et al.* Top and bottom surfaces limit carrier lifetime in lead iodide perovskite films. *Nat. Energy* **2**, 16207 (2017).

18. Wei, H. *et al.* Sensitive X-ray detectors made of methylammonium lead tribromide perovskite single crystals. *Nat. Photonics* **10**, 333–339 (2016).

19. Wei, W. *et al.* Monolithic integration of hybrid perovskite single crystals with heterogenous substrate for highly sensitive X-ray imaging. *Nat. Photonics* **11**, 315–321 (2017).

20. Kim, Y. C. *et al.* Printable organometallic perovskite enables large-area, low-dose X-ray imaging. *Nature* **550**, 87–91 (2017).

21. Alsalloum, A. Y. *et al.* Low-Temperature Crystallization Enables 21.9 % Efficient Single-Crystal $MAPbI_3$ Inverted Perovskite Solar Cells . *ACS Energy Lett.* **5**, 657–662 (2020).

22. Muscarella, L. A. *et al.* Crystal Orientation and Grain Size: Do They Determine Optoelectronic Properties of $MAPbI_3$ Perovskite? *J. Phys. Chem. Lett.* **10**, 6010–6018 (2019).

Appendix

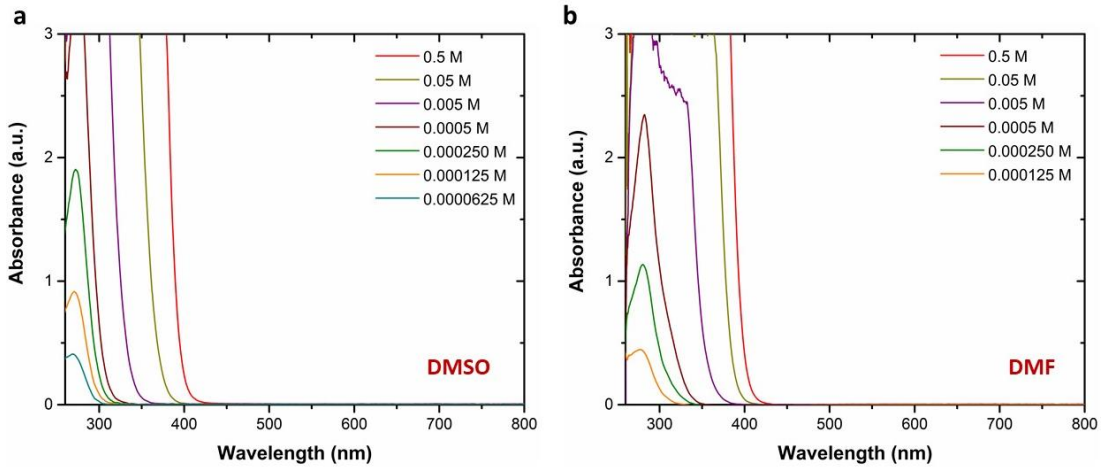

Figure A1: The UV-Vis absorption characteristics of $MAPbBr_3$ precursors employing (a) DMSO, (b) DMF. The precursor exists only in $[PbBrXn]^+$ form in both solvents.

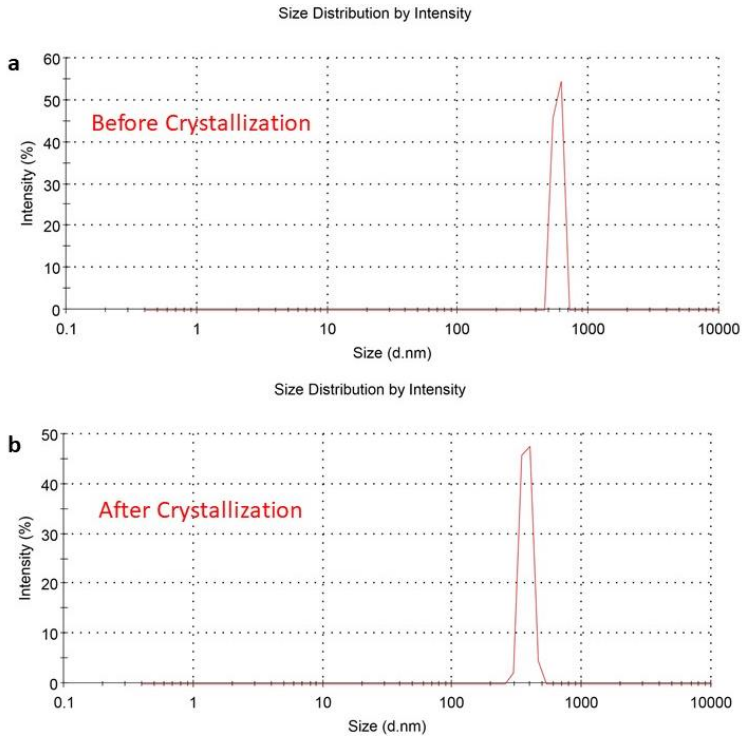

Figure A2: The DLS data for $MAPbBr_3$ precursor in DMF before (colloidal size: 450 nm – 750 nm) and after crystallization. The colloidal sizes reduce (to 250 nm – 450 nm) after crystallization (after 60 hours of anti-solvent introduction).

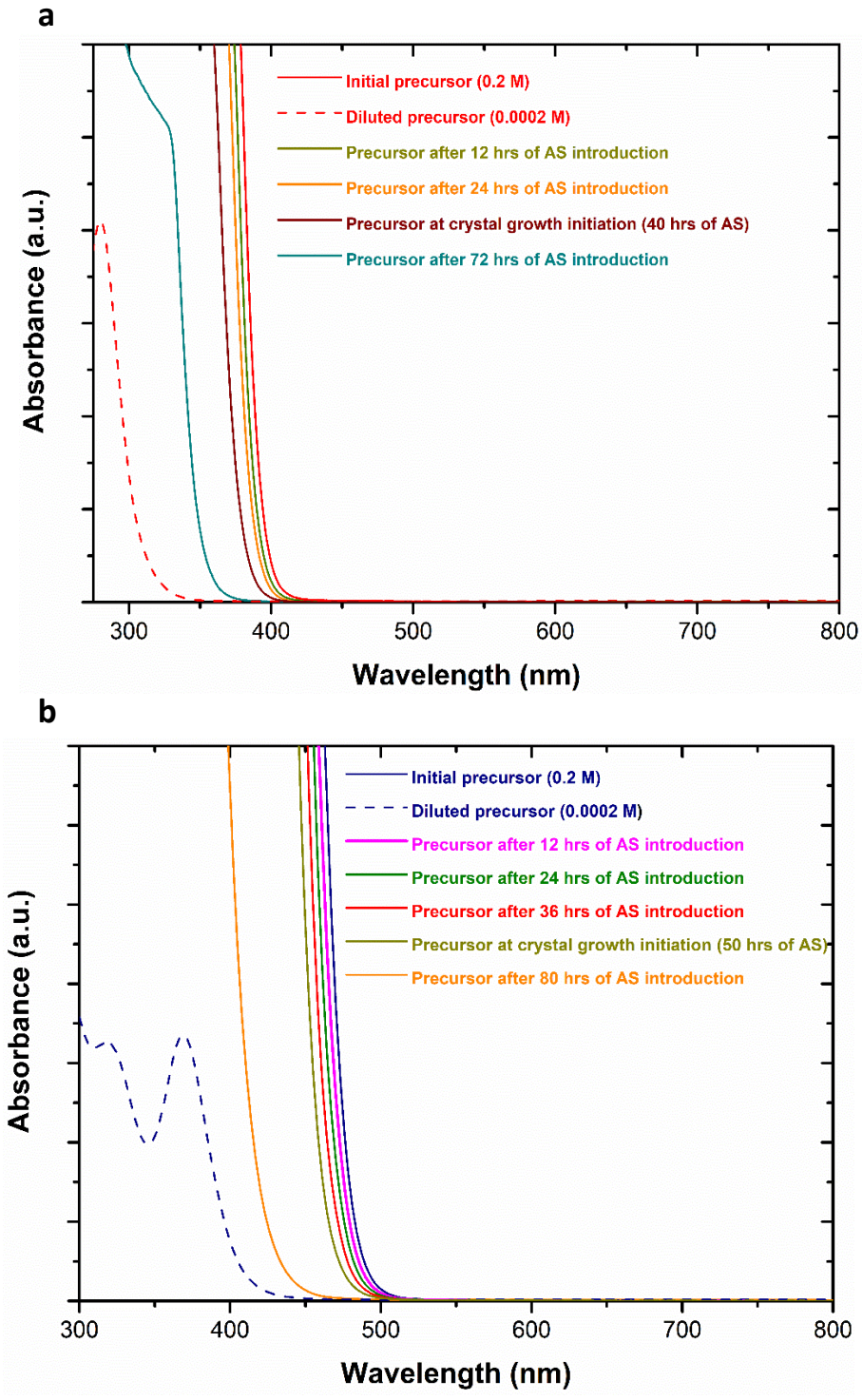

Figure A3: UV- Visible absorption spectra of (a) $MAPbBr_3$ and (b) $MAPbI_3$ precursors before, during and after crystallization.

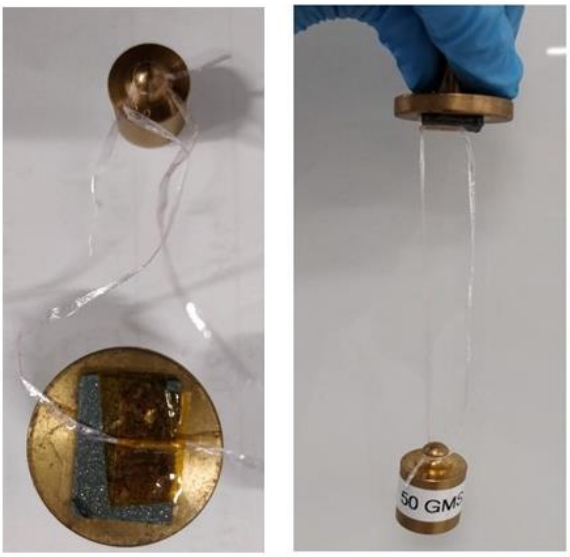

Figure A4: Tensile force applied by using a 50 g standard weight on $MAPbI_3$ crystals grown over FTO substrates. The crystals are able to sustain high tensile forces indicating a good adhesiveness with the substrate.

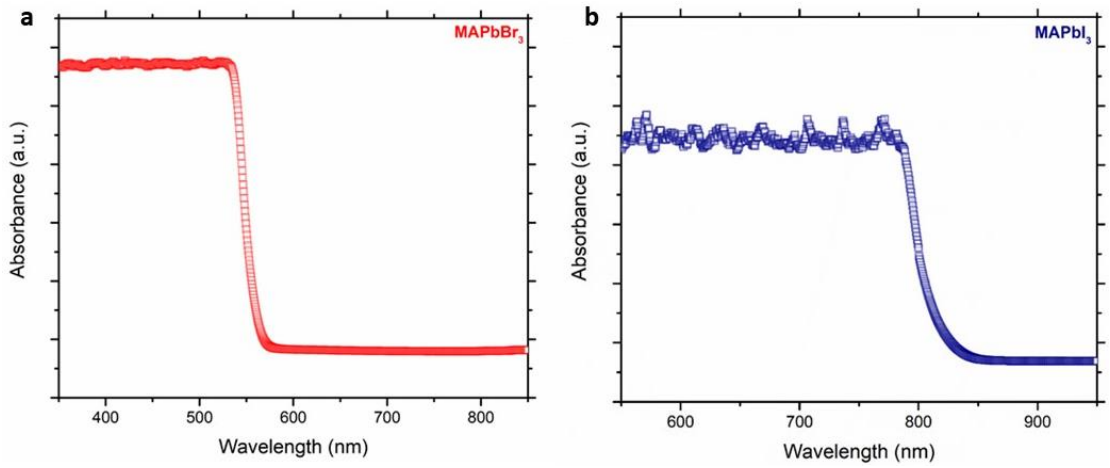

Figure A5: UV-Visible absorption spectra for (a) $MAPbBr_3$ and (b) $MAPbI_3$ crystals grown by S-AVC.

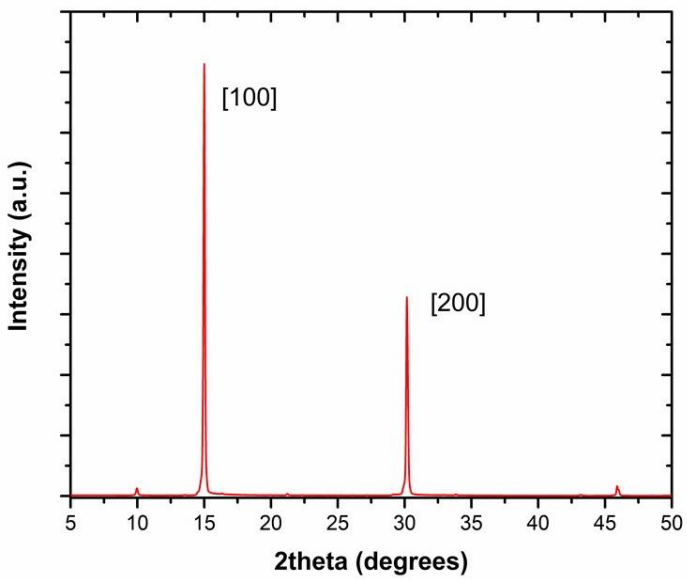

Figure A6: XRD of $MAPbBr_3$ precursor in DMSO after spinning, before annealing. The XRD reveals that the precursor is converted to perovskite phase even before annealing.

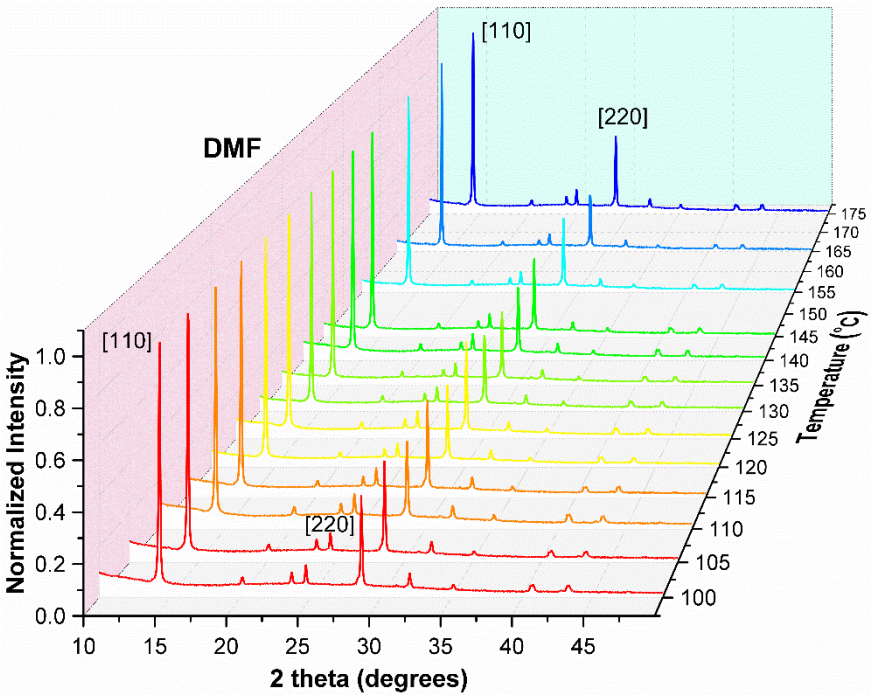

Figure A7: XRD of $MAPbI_3$ film grown from DMF at various annealing temperatures.

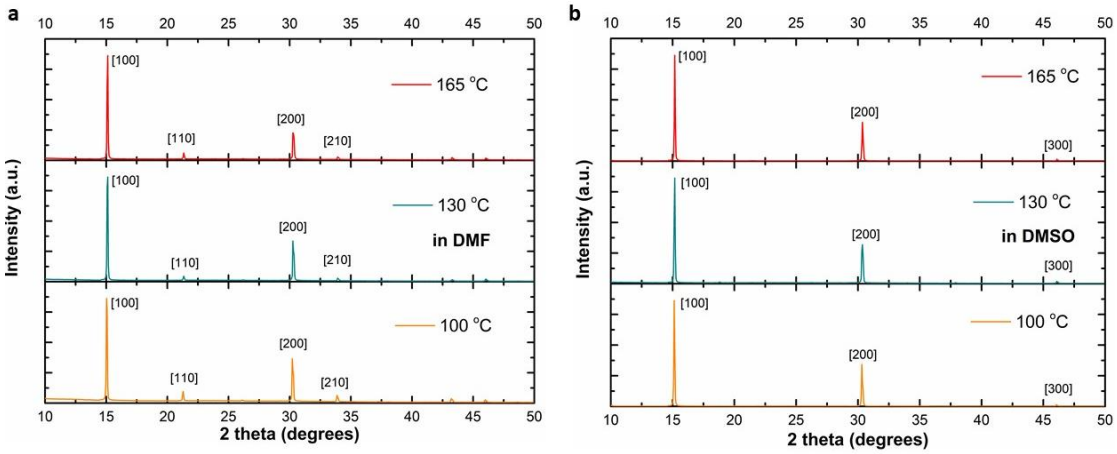

Figure A8: $MAPbBr_3$ films grown at various annealing temperatures in (a) DMF, (b) DMSO based precursors.

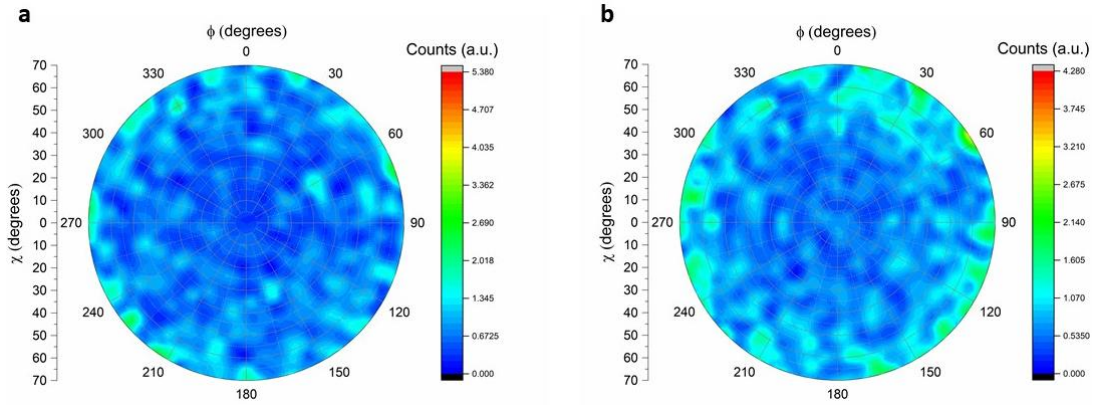

Figure A9: Out of plane pole figures of X-rays diffracted from (a) [202] and (b) [310] planes of $MAPbI_3$.

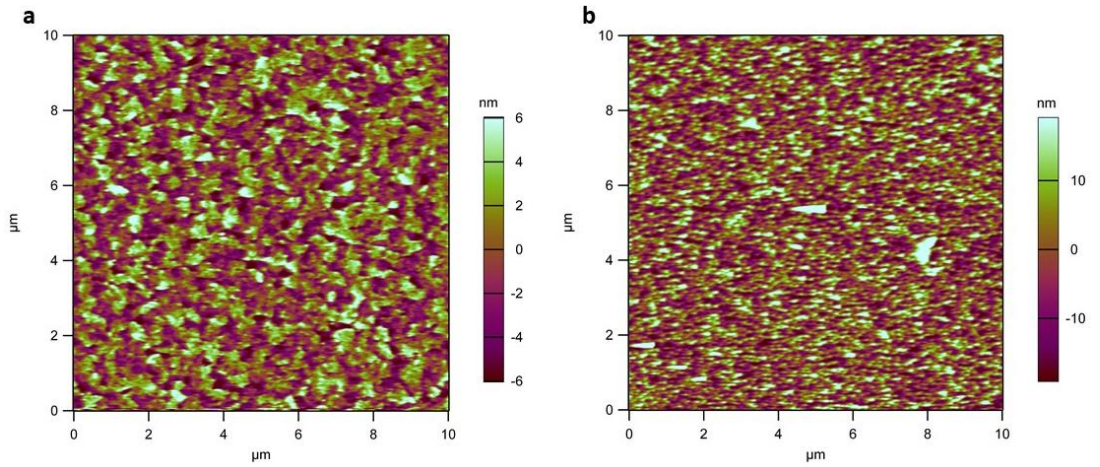

Figure A10: Surface roughness of (a) ITO and (b) FTO substrates measured by AFM.

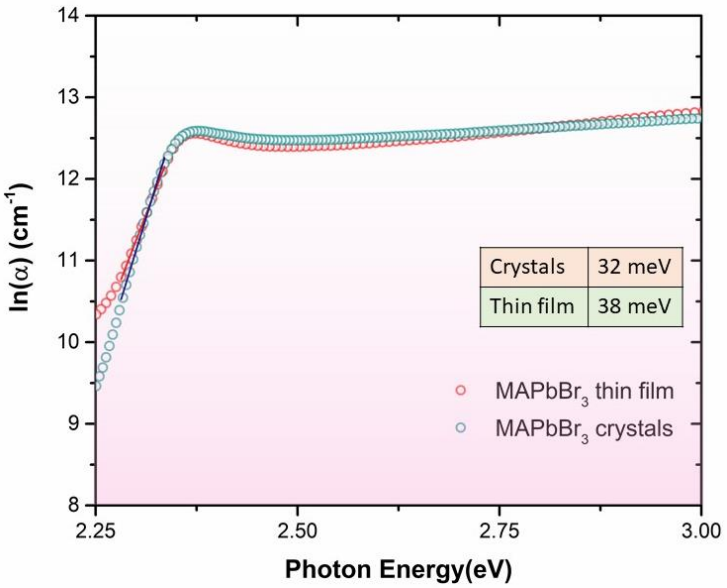

Figure A11: Urbach energy tails obtained for $MAPbBr_3$ crystals and normal thin films.

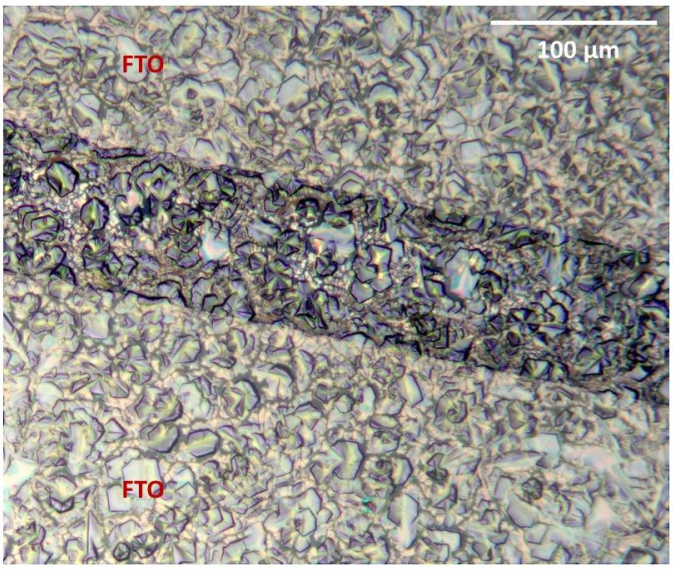

Figure A12: Discontinuous growth of spherulitic $MAPbI_3$ crystals over prepatterned FTO substrates.

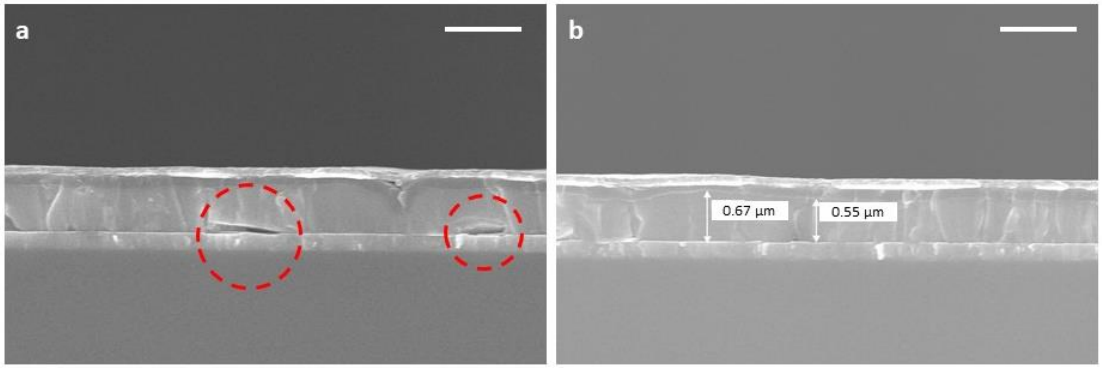

Figure A13: (a) Poor SnO_2-$MAPbI_3$ interfaces in spherulitic crystal based solar cells, (b) Inferior MAPbI3-spiro interfaces originating from thickness differences of crystal films.

List of Publications

1. Chathuranga Hettiarachchi, Muhammad Danang Birowosuto, Tien Hoa Nguyen, Riyas Ahmad, Kantisara Pita, Nripan Mathews and Cuong Dang, Solution grown double heterostructure on a large hybrid halide perovskite crystal. *CrystEngComm*, 20, 6653-6661 (2018). DOI: 10.1039/c8ce01298a.

2. Sjoerd A. Veldhuis, Yan Fong Ng, Riyas Ahmad, Annalisa Bruno, Nur Fadilah Jamaludin, Bahulayan Damodaran, Nripan Mathews and Subodh G. Mhaisalkar, Crown Ethers Enable Room-Temperature Synthesis of $CsPbBr_3$ Quantum Dots for Light-Emitting Diodes. *ACS Energy Letters*, 3, 526–531 (2018). DOI: 10.1021/acsenergylett.7b01257.

3. Riyas Ahmad, Abhijith Surendran, P. C. Harikesh, Reinhard Haselsberger, Nur Fadilah Jamaludin, Rohit Abraham John, Teck Ming Koh, Annalisa Bruno, Wei Lin Leong, Nripan Mathews, Maria-Elisabeth Michel-Beyerle, Subodh G. Mhaisalkar, Perturbation-Induced Seeding and Crystallization of Hybrid Perovskites over Surface-Modified Substrates for Optoelectronic Devices. *ACS Applied Materials and Interfaces*, 31, 27727–27734 (2019). DOI: 10.1021/acsami.9b05965.

4. Riyas Ahmad, Pio John S. Buenconsejo, Ming Pin Alan Lim, P.C. Harikesh, Vipinraj Sugathan, Reinhard Haselsberger, Bening Titra Muhammad, Teck Ming Koh, Annalisa Bruno, Wei Lin Leong, Nripan Mathews, Maria-Elisabeth Michel-Beyerle, Subodh G. Mhaisalkar, Highly Crystalline and Oriented $MAPbI_3$ Spherulitic Films by Tailoring Crystal Growth Kinetics. (in publication).